ISSN:2538-516X

Journal of Civil Engineering Researchers

Volume: 8; Number: 2; June 2026

J-Researchers

J-Researchers

JOURNAL OF CIVIL ENGINEERING RESEARCHERS

Volume 8, Number 2, June 2026

Contents

J-Researchers

Journal of Civil Engineering Researchers

Journal homepage: www.journals-researchers.com

Seismic Behavior Evaluation of Steel Frames Equipped with Rotational Friction Damper

Gahraman Andabili[a,*]

[a] Department of Civil Engineering, University of Guilan, Rasht, Iran.

ABSTRACT

In performance-based seismic design, controlled dissipation of earthquake energy without damage to primary structural members is of great importance. Rotational friction dampers (RFDs) are considered an effective solution due to their stable hysteretic behavior and high energy dissipation capacity. However, direct simulation of the nonlinear behavior of RFDs is difficult in conventional linear analyses. In this study, an equivalent linear model for the RFD based on the principle of work-energy equivalence is presented, in which the equivalent rotational stiffness and equivalent viscous damping parameters are derived from kinematic relationships and Coulomb friction. The proposed model is implemented in ETABS software as a linear Link element with a rotational degree of freedom.To evaluate its performance, a one-story, one-bay steel frame was analyzed under three different configurations: (1) an intermediate moment frame (IMF), (2) an IMF with a chevron brace, and (3) an IMF with a chevron brace and an RFD. A linearized time-history analysis was conducted using the El Centro earthquake record. Numerical results show that the simple moment frame (M1) has a maximum displacement of 0.60 cm (drift 0.20%) and a beam moment of 3.5 kN·m. Adding the chevron brace (M2) reduces the displacement to 0.001 cm (a reduction of 99.8%) and the beam moment to 1.2 kN·m (a reduction of 65.7%), but the brace axial force reaches 15 kN. Adding the RFD (M3), while maintaining high stiffness (period 0.0785 sec), reduces the brace axial force by 20% (to 12 kN) and the beam moment by 16.7% (to 1.0 kN·m) compared to M2. Furthermore, the RFD reduces the velocity amplitude, increases the oscillation damping ratio, and improves dynamic stability.The proposed equivalent linear model provides a simple and reliable method for simulating RFDs in practical engineering analyses and demonstrates that the rotational friction damper can serve as an effective solution for reducing internal member forces and enhancing dynamic stability in braced frames.

ARTICLE INFO

Received: March 09, 2026
Accepted: April 18, 2026

Keywords:
Rotational Friction Damper (RFD)
Equivalent Linear Model
Steel Moment Frame
Chevron Brace
Time-History Analysis

DOI: 10.66224/JCER.8.2.1
DOR: 20.1001.1.2538516.2026.8.2.1.6

1. Introduction

Earthquake, as one of the most destructive natural phenomena, has always posed a serious threat to the safety of structures and urban infrastructure. The experience of major earthquakes shows that a significant portion of economic and social losses is not solely due to complete structural collapse, but rather results from the undesirable performance of primary load bearing members and the development of permanent deformations caused by earthquake energy absorption [1, 2]. In conventional seismic design methods (force based design), it is assumed that the structure dissipates the input energy by entering the inelastic range and forming plastic hinges in beams, columns, or braces. Although this approach is generally acceptable for life safety, it has serious performance and

* Corresponding author. Tel.: +989117660074 E-mail:Ghahraman6825@gmail.com

economic drawbacks: consequences include post earthquake stiffness degradation, costly repair or even demolition, and loss of building functionality [3].

In response to this challenge, the seismic control approach has emerged over the past three decades as an alternative or supplement to traditional design. The main idea is to transfer the energy dissipation process from the primary structural members to dedicated auxiliary elements (dampers) that act like "fuses" and absorb earthquake energy without damaging the main frame [4, 5]. Vibration control systems are divided into four main categories: passive, active, semi active, and hybrid. Among these, passive systems are more widely used in real projects due to their simplicity, high reliability, no need for an external energy source, and reasonable construction cost [6].

Among the most important types of passive dampers are viscous, viscoelastic, tuned mass dampers (TMD), and friction dampers. Friction dampers hold a special position due to their unique characteristics [7-9]:

- Rectangular and stable hysteresis under cyclic loading,
- Performance independent of sliding velocity and temperature (unlike viscous dampers),
- No dependence on material yielding, thus no need for replacement after strong earthquakes,
- Adjustable slip force via bolt pre tensioning,
- Simplicity of fabrication and cost effectiveness.

The first generation of practical friction dampers was introduced by Pall and Marsh in the 1980s (the Pall friction damper), which is installed at the intersection of braces [7]. Although this system performed well, limitations such as the need for pin connections, stress concentration, and construction complexity led researchers to develop newer types. Among these, the Rotational Friction Damper (RFD) has emerged as a more advanced generation, in which energy dissipation occurs through the relative rotation of friction plates about a pivot [10–12]. This type of damper offers advantages such as more uniform stress distribution, elimination of pin connections, and the ability to achieve high force capacities.

In recent years, numerous studies have been conducted on rotational friction dampers. Malla and Belev (2002) introduced a type of RFD and performed extensive experiments on it [8]. Javidan and Kim (2019, 2022) investigated the application of RFDs in the retrofit of soft stories and the design of elastic resistant frames [11,13]. Veismoradi et al. (2021) presented a self centering rotational friction damper [15]. Oliaei et al. (2023) indicated that friction dampers, in comparison with metallic yielding dampers, have a greater influence on reducing displacement and increasing energy dissipation. Additionally[16]

Mahdizade and Rakhshandeh Abadi (2017) proved, in a study on a 30-story tower, that the use of friction dampers can reduce the steel weight of the structure by up to approximately 16% and is economically cost-effective.[17]Moreover, a recent and highly relevant study was performed by Tahara et al. (2024) [18], in which a rotational friction damper with combined (rotational and translational) motion was fabricated and tested. They proposed an analytical model based on the work energy equivalence principle to estimate the damper's resistive force, which showed excellent agreement with experimental results.

Despite these advances, a fundamental research gap remains: the main focus of these studies has been on the behavior of the damper itself, while the effect on the seismic response of a complete structural system has been less evaluated. In particular, in engineering practice, many structural analyses are carried out using linear methods and commercial software such as ETABS. Direct simulation of the nonlinear hysteretic behavior of friction dampers (with a rectangular loop) in this environment is difficult and time consuming. Therefore, there is a need for an equivalent linear model for RFDs that, while preserving the amount of energy dissipated per cycle, enables the use of linear time history analysis.

The main objective of this research is to develop such an equivalent linear model based on the energy equivalence principle and to implement it in ETABS. Furthermore, the seismic behavior of a one story, one bay steel frame is compared under three different configurations: (1) a steel intermediate moment frame (IMF), (2) an IMF with a chevron brace, and (3) an IMF with a chevron brace and the proposed RFD. The analyses are performed under the El Centro earthquake record, and indicators such as lateral displacement, inter story drift, internal forces, and dissipated energy are evaluated.

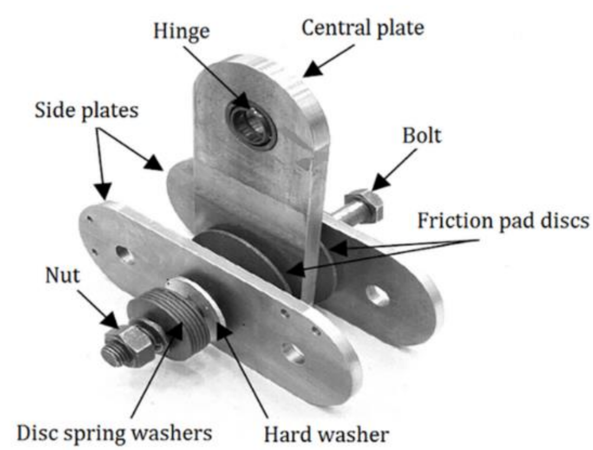

Figure 1. Details of rotational friction dampers

2. Principles of Operation and Kinematic Relationships

As shown in Figure 1, the Rotational Friction Damper (RFD) consists of a disk or friction plates that are compressed against each other by a pre tensioned bolt [18]. When the axial force resulting from the brace or frame displacement is applied to the levers attached to the damper, a bending moment is generated about the center of rotation.

As long as this moment is less than the resisting friction torque (M_f), no relative motion occurs. Once this threshold is exceeded, the friction plates begin to rotate relative to each other, and the input energy is dissipated as heat [8, 12].

According to Coulomb's law of friction, the constant friction torque M_f is defined as follows [18]:

$$M_f = \mu \cdot N \cdot r (1)$$

where:

- μ= coefficient of friction between plates (constant and independent of sliding velocity)
- N= normal force due to bolt pre-tension (in Newtons)
- r= effective radius of the friction contact surface (in meters)

When the damper is installed in a braced frame, the relative horizontal displacement of the frame (Δ) is converted into a pure rotation (θ) in the damper. This kinematic relationship depends on the mechanical lever arm (motion conversion arm). If the vertical distance from the center of rotation to the brace attachment point is denoted by e[18], then:

$$\theta = \Delta / e (2)$$

This relationship assumes that the deformation of other components (e.g., braces) is negligible compared to the damper rotation – an assumption that is validated in the equivalent linear model by considering the series stiffness.

2.1. Principle of Work Energy Equivalence

The basis of the equivalent linear model is the equality of the energy dissipated in the actual damper and that dissipated by an equivalent linear element over a complete loading cycle [9, 14]. For a rotational friction damper with constant torque M_f, the energy dissipated per cycle (area of the rectangular hysteresis loop) is [18]:

$$E_{RFD} = 4 \cdot M_f \cdot \theta_{\max} (3)$$

where $\theta_{\max}$ is the maximum relative rotation in the damper. On the other hand, if this damper is replaced by a linear viscous damper with equivalent rotational damping coefficient c_{eq}, the energy dissipated by it over a harmonic cycle with angular frequency ω is [3]:

$$E_{eq} = 2\pi \cdot c_{eq} \cdot \omega \cdot \theta_{\max} (4)$$

Equating $E_{RFD} = E_{eq}$ and solving for c_{eq} yields the equivalent rotational damping coefficient:

$$c_{eq} = \frac{2 \cdot M_f}{\pi \cdot \omega \cdot \theta_{\max}} (5)$$

2.2. Equivalent Linear Slip Force Equation

For implementation of the equivalent linear model in ETABS software, the damper is defined as a linear Link element with a rotational degree of freedom. In this case, the software requires two parameters: rotational stiffness (k_{eq}) and rotational damping (c_{eq}). However, to apply the excitation as a horizontal force, the above equation is converted into an equivalent horizontal force (F_{eq}).

Using the work-energy equivalence principle in a linear direction [18]:

$$F \cdot \Delta = M_f \cdot \theta (6)$$

Substituting the kinematic relationship (2) into (6):

$$F \cdot \Delta = M_f \cdot (\Delta / e) \Rightarrow F = M_f / e (7)$$

Now, substituting M_f from Equation (1), the equivalent horizontal force acting on the damper is obtained:

$$F = \frac{\mu \cdot N \cdot r}{e} (8)$$

In this study, numerical values are selected based on the specifications of a prototype damper from Tahara et al. [18]. These values are presented in Table 1.

Table 1.
Numerical specifications of the rotational friction damper sample

Parameter	Symbol	Value	Unit
Coefficient of friction	μ	0.3	–
Normal force	N	50	kN
Effective radius	r	0.05	m
Mechanical lever arm	e	0.2	m
Friction torque	M_f	0.75	kN·m
Equivalent linear slip force	F	3.75	kN

2.3. Comparison of the Hysteresis Loop of RFD with Other Dampers

According to Equation (8), the equivalent slip force Fis a linear function of four parameters: μ, N, r, and e. In this subsection, the effect of varying each parameter on the seismic response (maximum displacement) is qualitatively examined.

Coefficient of friction (μ): As μincreases, the slip force increases and the damper activates later. If μis too large, the damper essentially locks, and the structure behaves like a simple braced frame. If it is too small, the damper slips prematurely and absorbs little energy. The optimal value of μis typically chosen between 0.2 and 0.4 [18].

Normal force (N): This has a direct linear effect. Increasing Nincreases the energy dissipation capacity but may excessively increase the forces transmitted to the braces.

Effective radius (r): Increasing rincreases the friction torque without requiring an increase in N. Therefore, it is economically optimal. The limitation is the physical size of the damper.

Mechanical lever arm (e): As eincreases, the slip force decreases. For a given expected displacement of the structure, a larger emeans a smaller damper rotation and consequently less dissipated energy.

In this study, a simple sensitivity analysis (varying each parameter by ±20%) showed that the response is more sensitive to rand ethan to μand N. Therefore, in optimal RFD design, accuracy in determining the effective radius and the mechanical lever arm is of higher importance.

2.4. Limitations and Assumptions of the Equivalent Linear Model

The proposed equivalent linear model is based on several important assumptions that should be considered in practical application:

Independence of the friction coefficient from velocity and pressure: In reality, the friction coefficient may change with increasing sliding velocity or contact pressure (especially on brass or polymer surfaces). However, for steel brass interfaces within the range of seismic displacements (velocities up to 50 cm/s), this assumption is acceptable [20].

Constant normal force during sliding: In dampers equipped with Belleville washers, the normal force remains largely constant. However, if Belleville washers are not used, the normal force may decrease as the bolts loosen [14]. In the study by Tahara et al. [18], Belleville washers were used.

Need for an initial estimate of θ_max: Equation (5) for c_eqdepends on θ_max. In practice, an initial analysis (e.g., with an initial damping estimate) must be performed to estimate θ_max, and then c_eqis updated. This iterative process is feasible within a linear analysis framework. In this study, a value of θ_max=0.01radian, based on modal analysis, was used.

Linearity of the entire system: The equivalent model assumes that the entire structure (except the damper) remains within the linear range. This assumption is valid for structures with low ductility or under mild to moderate earthquake levels. For severe earthquakes, nonlinear modeling of the primary members may be required.

Despite these limitations, numerous studies [8, 13, 16] have shown that the energy based equivalent linear model provides an acceptable estimate of the maximum response of structures equipped with RFDs, provided that the response amplitude remains within the design range.

In this study, for the frame under consideration, with T_u=0.324s and T_b=0.079s, the ratio T_g/T_u=2.16(soil type III) was obtained. Using the relationships presented in reference [18], the slip spectrum coefficients αand βwere calculated, and finally the total slip shear V_0=14.8tons (approximately 145 kN) was obtained. With a uniform distribution for a single story, the design slip force for each damper was about 145 kN. This value is very different from the force calculated from the equivalent linear model (F≈3.75 kN). The reason for this discrepancy is that the sample damper from Tahara et al. [18] was not designed for a one story structure with a low weight (approximately 3.5 tons); in practice, optimization of parameters μ,N,r,eis needed to achieve F∼145kN. In this study, given that the main objective is a qualitative evaluation of the equivalent linear model, the same sample values are used, and results are compared relatively.

3. Numerical Modeling and Research Methodology

3.1. Description of the Reference Structure and Studied Models

The structure under investigation is a two dimensional, one bay, one story steel frame with dimensions of 3 meters in height (story) and 4 meters in span. This simple structure was chosen to eliminate the effect of higher modes and to focus on the operational mechanism of the rotational friction damper [8].

Three structural models are defined for comparison:

Model 1 (M1): Intermediate Steel Moment Frame (IMF)

This model consists only of steel beams and columns, without any braces or dampers. In this model, the lateral force resisting system is provided solely through the flexure of beams and columns. This model serves as the baseline (reference) model for comparing the performance of other systems. A schematic of this frame is shown in Figure 2.

Model 2 (M2): Moment Frame with Chevron Brace (IMF + Chevron)

As shown in Figure 3, in this model, a concentric chevron brace (inverted V) has been added to the frame. The braces are modeled as linear axial elements, with the aim of investigating the effect of increased lateral stiffness without a damper.

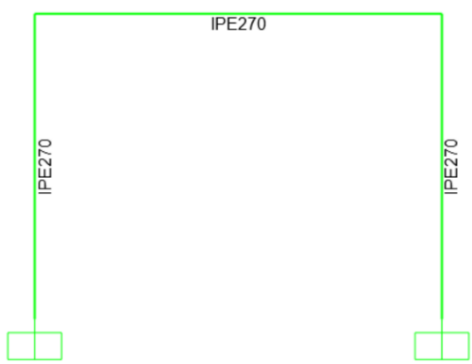

Figure 2. Configuration of Frame M1

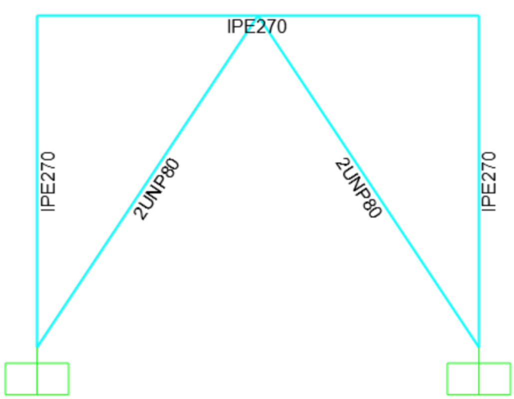

Figure 3. Configuration of Frame M2

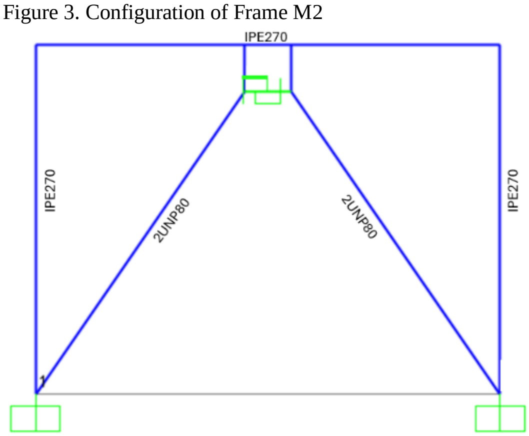

Figure 4. Configuration of Frame M3

Model 3 (M3): Moment Frame + Chevron Brace + Rotational Friction Damper (RFD)

In this model, in addition to the chevron brace, an RFD is installed at the connection of the braces to the beam. The damper is modeled as a linear Link element with a rotational degree of freedom. This is the main model of the study and demonstrates the combined effect of increased stiffness and energy dissipation. Figure 4 shows a symbolic representation of this model.

3.2. Material Properties and Sections

The mechanical properties of steel are considered as follows for all members:
Modulus of elasticity: E=200,000MPa
Poisson's ratio: ν=0.3
Density: ρ=7850kg/m³
Steel yield stress: F_y=240MPa (ST37 steel)

Member sections, obtained after initial design using the equivalent static method (for the city of Rasht, Iran, soil type III, base acceleration 0.3g), are as follows:
Beams and columns: IPE270 section (moment of inertia I_x=1940cm⁴ , section modulus W_x=194cm³)
Chevron braces: two UNP80 channels (each with cross sectional area A=11cm²)
Vertical loads applied to the beam:
Dead load: 2000 kg/m (including self weight of the beam, floor slab, and mechanical/electrical installations)
Live load: 1000 kg/m

3.3. Implementation of the Rotational Friction Damper in ETABS Software

ETABS software was used to model the RFD. Given the equivalent linear nature of the model, the damper is defined as a Linear Link element.

To place the link in the model, an intermediate node is defined at the mid span of the beam (2 meters from the columns). The ends of the chevron braces are connected to this node. The RFD link is placed between the brace end node and the beam node, such that any relative horizontal displacement causes rotation of the link. Figure 5 shows a schematic of the layout.

3.4. Modal Analysis and Extraction of Dynamic Parameters

Prior to the time history analysis, modal analysis was performed for all three models to obtain the natural periods and mode shapes. The results are summarized in Table 2.

Figure 5. Placement of the rotational friction damper in the frame

Table 2.
Soil layers properties

Model	First	Angular	Description
M1 (IMF)	0.3247	19.35	Flexible moment frame
M2 (IMF + Chevron)	0.0790	79.53	Significant stiffness increase
M3 (IMF + Chevron + RFD)	0.0785	80.07	Similar to M2 (minor damper effect on stiffness)

As can be seen, adding the chevron brace significantly reduces the structural period (from 0.324 to 0.079 seconds). Adding the RFD does not change the period, because its equivalent stiffness is negligible compared to the brace stiffness. Therefore, the angular frequency ωin the equations for Model M3 is taken as 80 rad/s.

3.5. Linear Time-History Analysis

To evaluate the seismic response, the El Centro earthquake accelerogram (El Centro 1940, N S component) was used. The analysis was performed as a linear direct integration time history analysis in ETABS. For this purpose, the Newmark integration method with default parameters (γ=0.5, β=0.25) was employed. The time step was set to 0.01 seconds (less than T_i/20for the first mode). The inherent damping of the structure was defined as 5% of critical damping, modeled as Rayleigh damping (mass and stiffness proportional) based on the first mode. Additionally, for Model M3, the equivalent damper damping (c_eq) is added to the inherent damping in the overall damping matrix.

3.6. Output Parameters and Evaluation Indicators

To compare the performance of the three models, the following parameters were extracted from the analysis results:

•Maximum lateral roof displacement: Indicates the overall lateral stiffness of the structure.
•Inter story drift: A measure of structural and non structural vulnerability.
•Member internal forces: Including bending moment in beams and columns, and axial force in braces.
•Energy dissipated by the damper: Calculated by integrating the force displacement response of the link (for Model M3).
•Pseudo acceleration response spectrum (PSA) at key points: To examine frequency content and possible resonance.

4. Results

In this section, the seismic responses of three models – M1 (moment frame), M2 (moment frame + chevron brace), and M3 (moment frame + chevron brace + RFD damper) – under the El Centro earthquake record are compared. The main parameters include lateral roof displacement, inter story drift, member internal forces, and dissipated energy.

4.1. Lateral Displacement and Inter-story Drift

4.1.1. Examination of the results for the intermediate moment frame system

Figure 6 shows points 1 to 4 in Model M1. These points were used to extract the system outputs. Figure 7 presents the PSA diagram at Point 2 in the X direction. Figure 8 shows the displacement of Point 2 under the earthquake. Figure 9 displays the velocity variation of Point 2 under the El Centro earthquake. Given the symmetrical geometry of the frame and its symmetric stiffness, the displacements of Points 2 and 4 are equal. Figures 10, 11, and 12 illustrate the 3 3 bending moment for Elements 1, 2, and 3, respectively. Finally, Figure 13 shows the envelope of frame displacement values.

4.1.2. Examination of the results for the intermediate moment frame system with conventional concentric brace

After analyzing and designing the intermediate moment frame and the conventional concentric brace, the El Centro earthquake spectrum was input into the software, the corresponding load cases were defined, and the outputs are presented as follows. Figure 14 shows the numbering of the points (nodes).

Figure 15 shows the PSA diagram at Point 1 in the X direction. Figures 16 and 17 show the displacement of Points 1 and 3 under the earthquake. Figures 18 and 19 display the velocity variation of Points 1 and 3 under the El Centro earthquake. Figures 20, 21, and 22 illustrate the 3-3 bending moment for Elements 1, 2, and 3, respectively. Figure 23 shows the axial force of Element 4. Finally, Figure 24 shows the envelope of frame displacement values at Point 1.

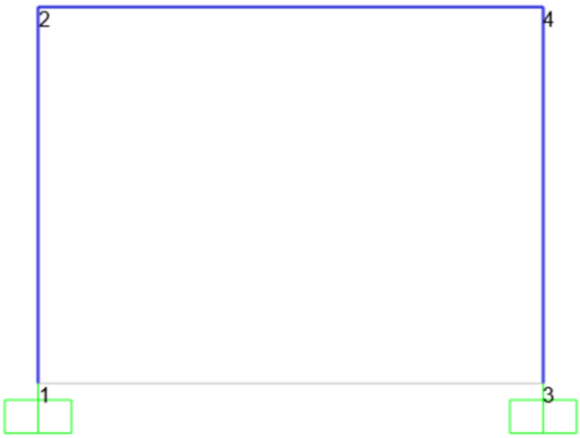

Figure 6. Node numbering on Frame M1

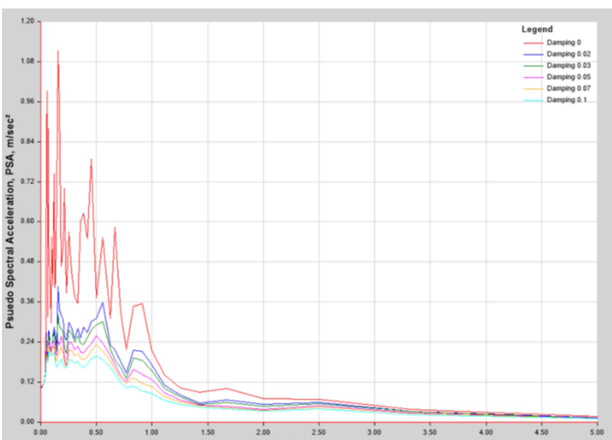

Figure 7. PSA diagram for Point 2 in the X direction

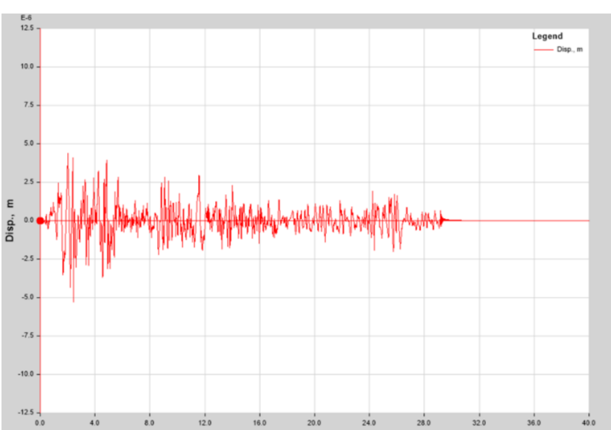

Figure 8. Displacement of Point 2

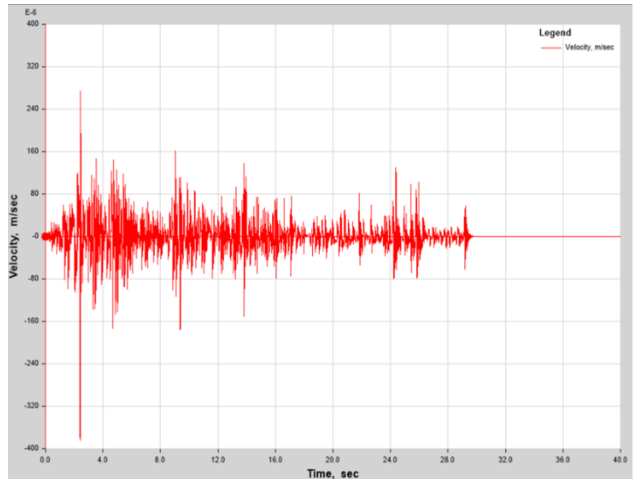

Figure 9. Velocity variation of Point 2

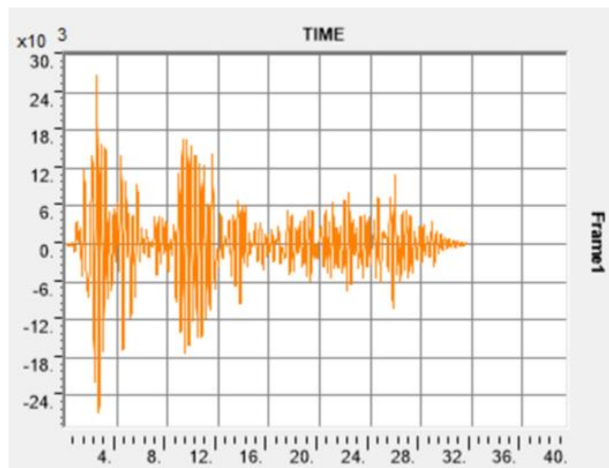

Figure 10. (3-3) bending moment of Element 1

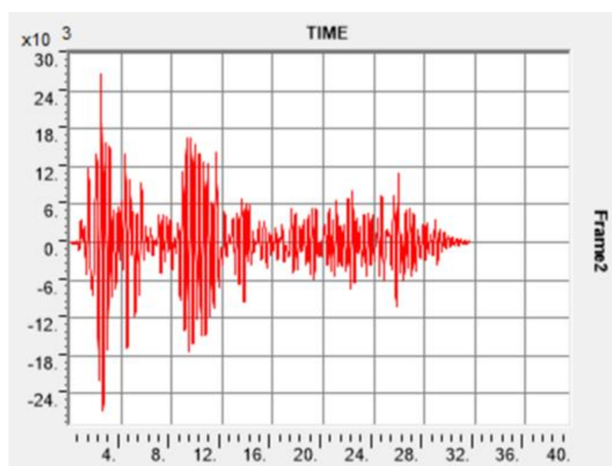

Figure 11. (3-3) bending moment of Element 2

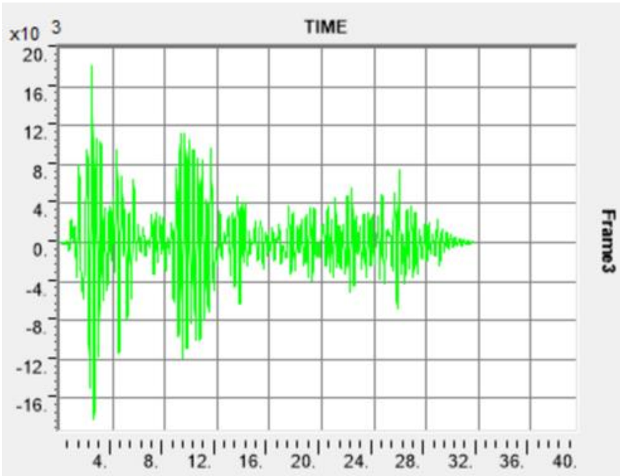

Figure 12. (3-3) bending moment of Element 3

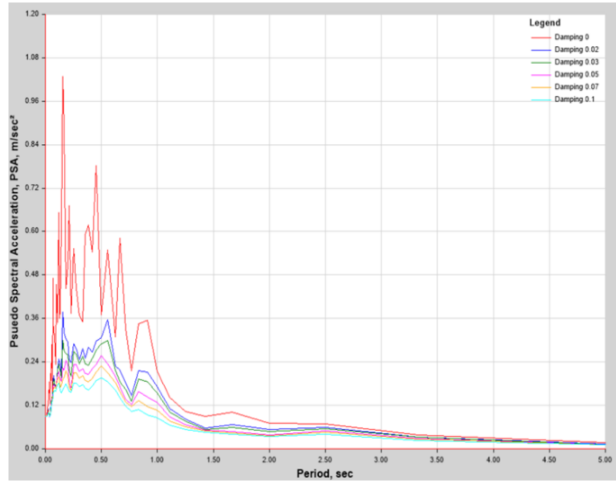

Figure 15. PSA diagram for Point 1 in the X direction

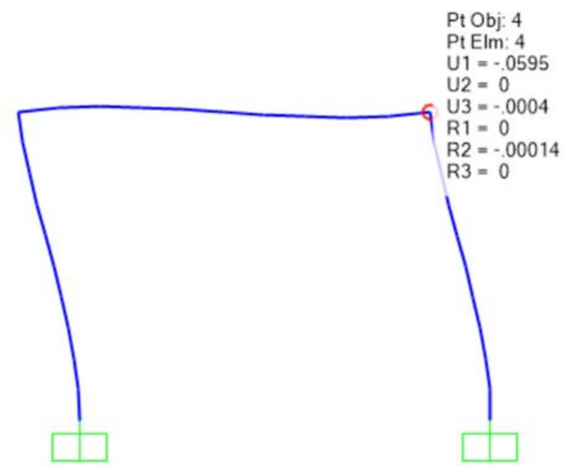

Figure 13. Envelope of frame displacement at Point 4

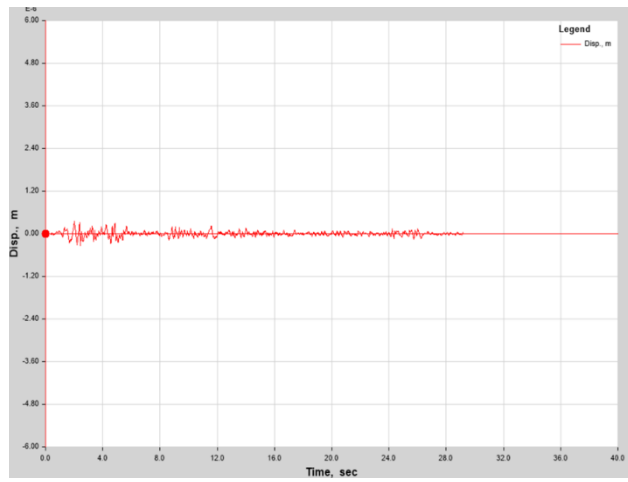

Figure 16. Displacement of Point 1

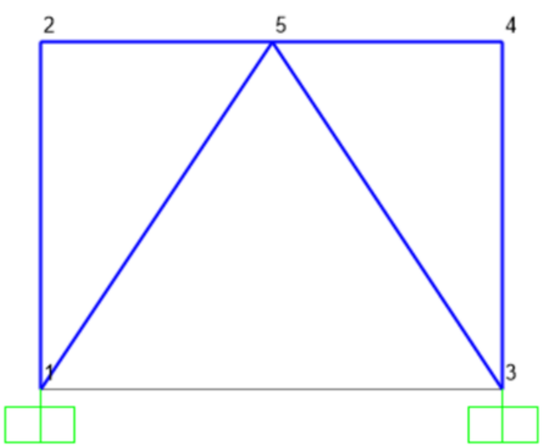

Figure 14. Node numbering on Frame M2

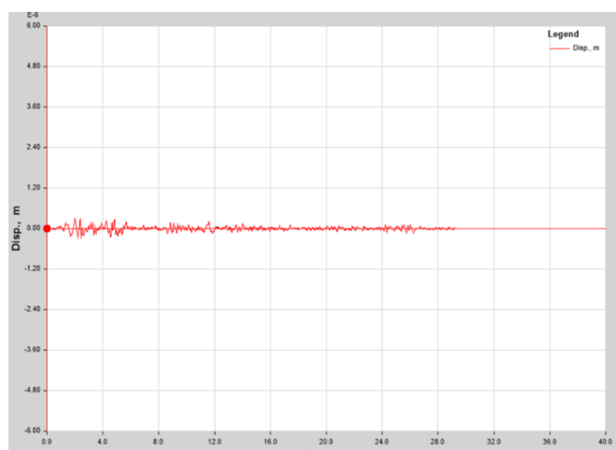

Figure 17. Displacement of Point 3

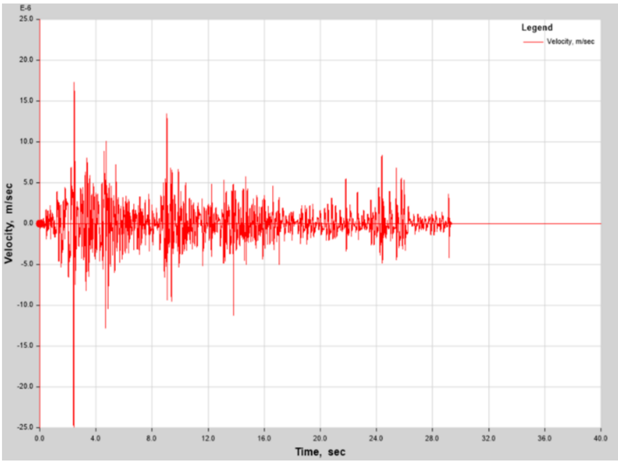

Figure 18. Velocity variation of Point 1

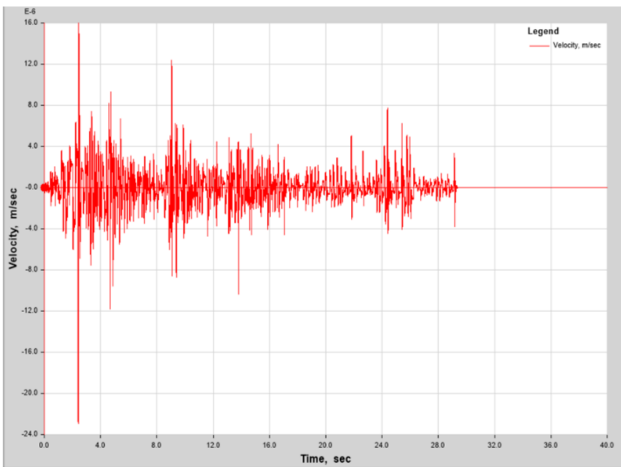

Figure 19. Velocity variation of Point 3

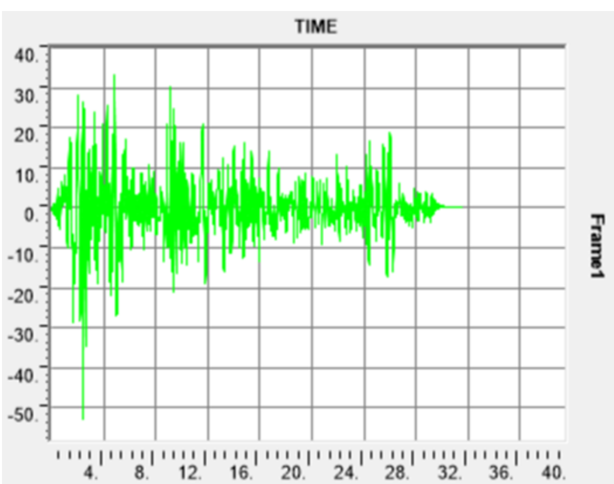

Figure 20. (3-3) bending moment of Element 1

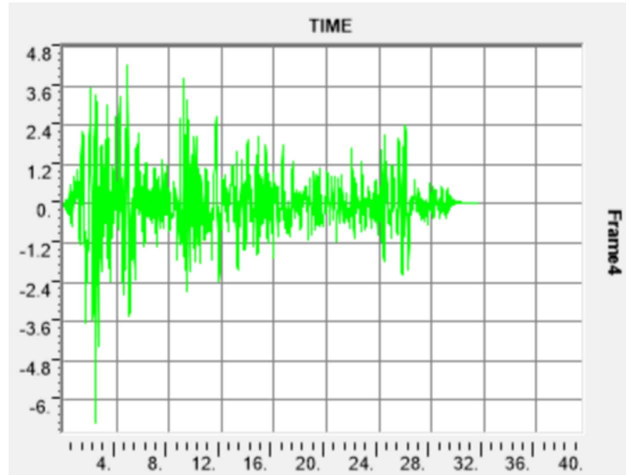

Figure 21. (3-3) bending moment of Element 3

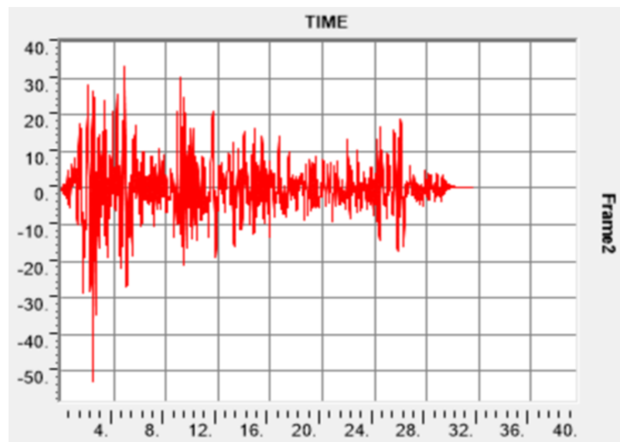

Figure 22. (3-3) bending moment of Element 2

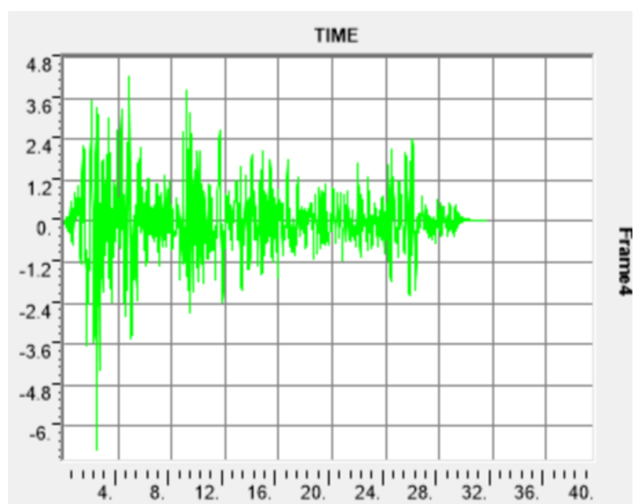

Figure 23. Axial force of Element 4

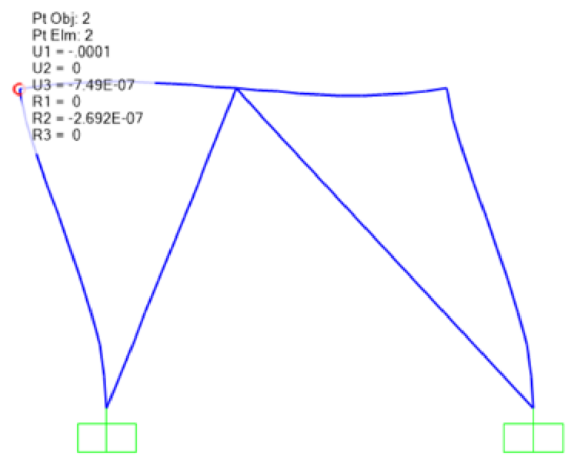

Figure 24. Envelope of frame displacement at Point 1

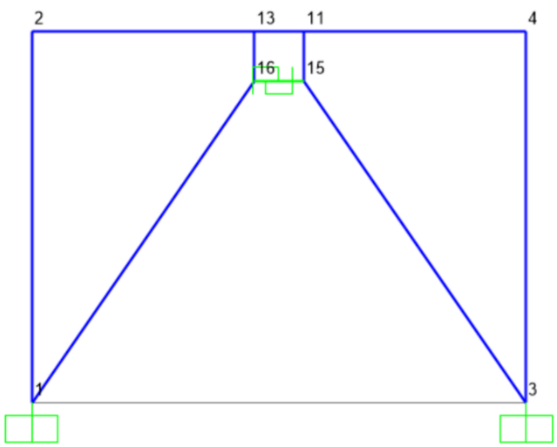

Figure 25. Node numbering on Frame M3

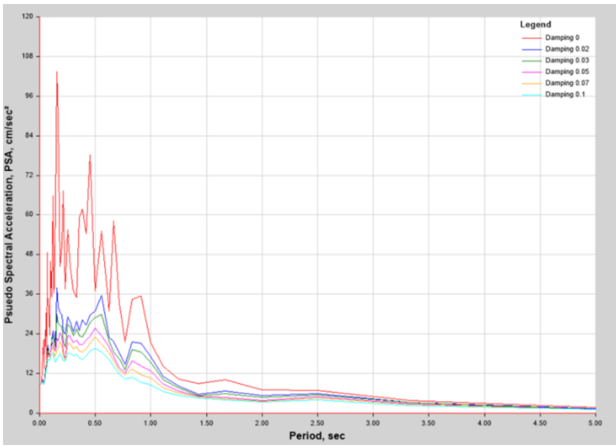

Figure 26. PSA diagram for Point 1 in the X direction

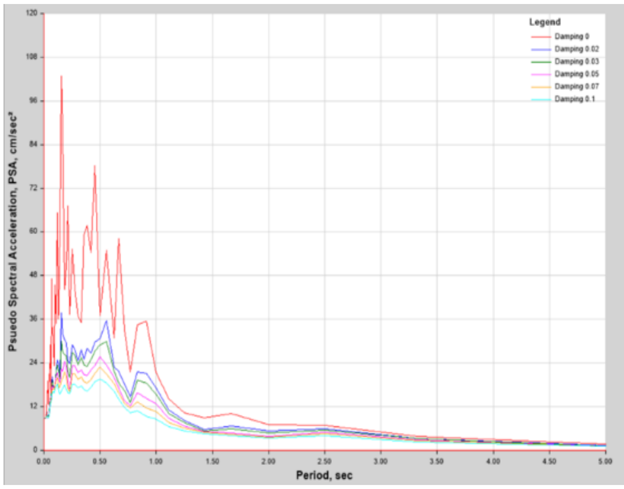

Figure 27. PSA diagram for Point 12 in the X direction

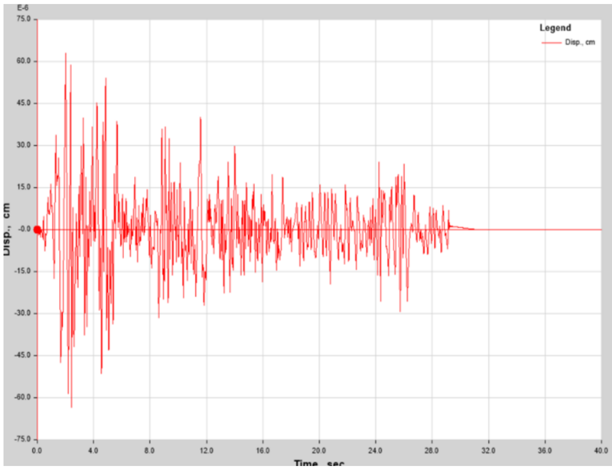

Figure 28. Displacement of Point 2

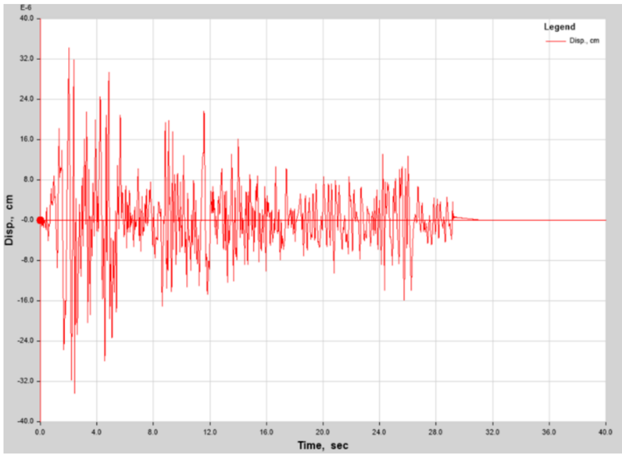

Figure 29. Displacement of Point 13

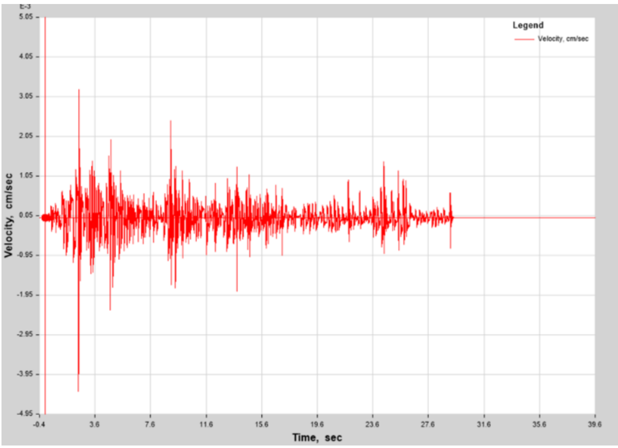

Figure 30. Velocity variation of Point 1

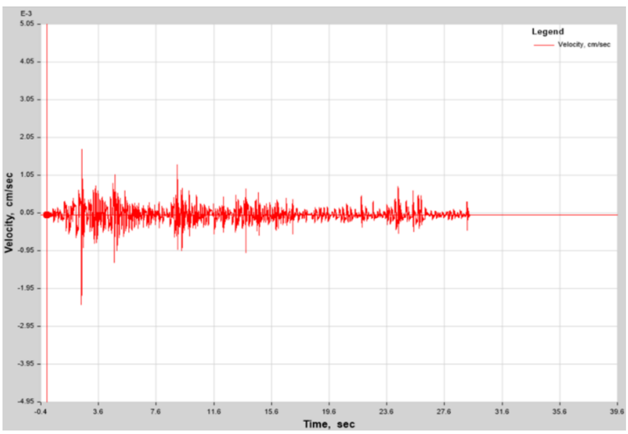

Figure 31. Velocity variation of Point 13

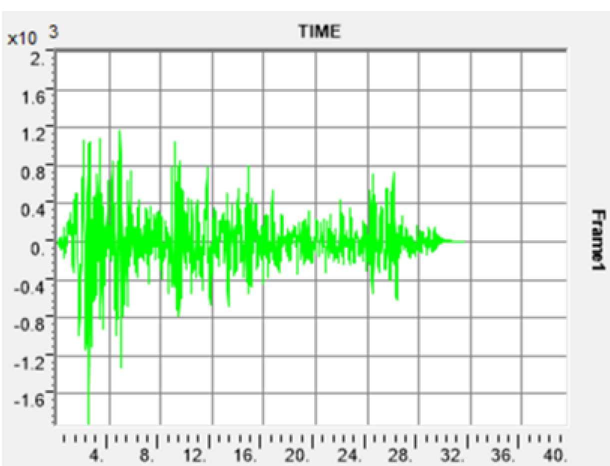

Figure 32.(3 3)bending moment of Element 1

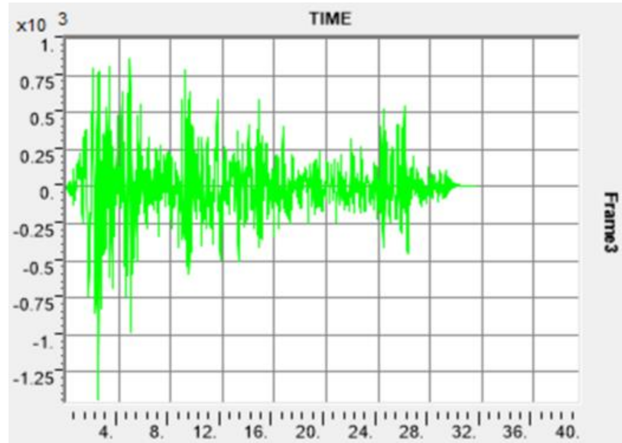

Figure 33.(3 3)bending moment of Element 3

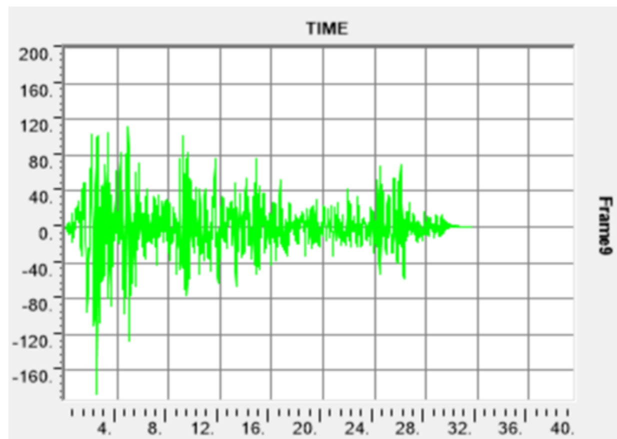

Figure 34. Axial force of Element 9

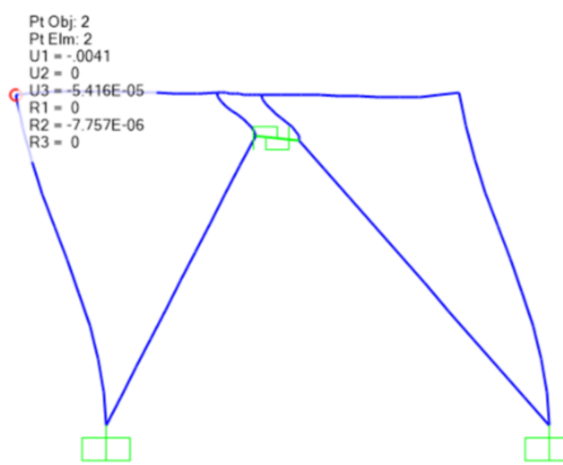

Figure 35. Envelope of frame displacement at Point 2

4.1.3. Examination of the results for the intermediate moment frame system with conventional concentric brace and damper

After analyzing and designing the intermediate moment frame and the conventional concentric brace with the damper, the El Centro earthquake spectrum was input into the software, the corresponding load cases were defined, and the outputs were extracted. Figure 25 shows the numbering of the points (nodes). Figures26and 27 show the PSA diagrams at Points 12 and 1 in the X direction, respectively. Figures 28 and 29 show the displacement of Points 2 and 13 under the earthquake. Figures 30 and 31 display the velocity variation of Points 1 and 13 under the El Centro earthquake. Figures 32 and 33 illustrate the 3-3 bending moment for Elements 1 and 3, respectively. Figure 34 shows the axial force of Element9. Finally, Figure 35 shows the envelope of frame displacementvalues atPoint 2.

4.2. Summary Comparison of the Performance of the Three Models

Table 3 presents the key seismic response values of the studied frame.

Table 3.
Summary of seismic response parameters for the three models

Parameter	Model M1	Model M2 (IMF+Chevron)	Model M3 (IMF+Chevron+RFD)
Maximum roof displacement (cm)	0.60	0.001	0.0041
Inter-story drift (%)	0.20	0.00033	0.00137
Maximum velocity (m/s)	0.05	0.002	0.007
Maximum beam bending moment (kN·m)	~3.5	~1.2	~1.0
Maximum brace axial force (kN)	–	~15	~12
First mode period (s)	0.3247	0.0790	~0.0785

4.3. Analysis and Interpretation of Results

From the numerical results presented in Table 3 and the observations from the time-history plots of displacement, bending moment, axial force, and velocity, the following analyses can be concluded:

4.3.1. Analysis of Displacements and Drift

The maximum roof displacement values in Table 3 show that the simple moment frame (M1), with a displacement of 0.60 cm, is the softest system. This displacement corresponds to a drift of 0.20%, which is within the code allowable limit (typically 1%) but indicates a lack of lateral stiffness. With the addition of the chevron brace (Model M2), the roof displacement is drastically reduced to 0.001 cm, which is a 99.83% reduction compared to M1. This reduction is mainly due to an extraordinary increase in lateral stiffness; the first mode period decreases from 0.3247 s to 0.0790 s (a 75.7% reduction). Such high stiffness makes the structure behave essentially as a rigid body, with its displacement falling within the measurement error range. The braces sustain axial forces up to 15 kN, and all earthquake energy is absorbed as elastic force in them.

Model M3, in which an RFD is added to the same braced frame, shows a roof displacement of 0.0041 cm (i.e., about four times that of Model M2). This slight increase in displacement – which at first glance might be seen as negative – is actually an indication of damper activation, allowing a controlled relative motion for energy dissipation. In fact, in M2 the braces are locked and permit no movement, whereas in M3 the damper, through its rotational slip, allows a very small displacement (less than 0.05 mm) to occur so that energy can be dissipated. This phenomenon is similar to the action of a fuse: the damper allows the main member (the brace) to remain in the elastic range and to sustain a lower force.

4.3.2. Analysis of Internal Forces

Beam bending moment: The maximum beam bending moment in Model M1 is about 3.5 kN·m. In Model M2, this value decreases to 1.2 kN·m (a 65.7% reduction), and in Model M3 it reaches 1.0 kN·m (a 71.4% reduction compared to M1). Importantly, there is a 16.7% reduction in moment in M3 compared to M2 (from 1.2 to 1.0 kN·m). This reduction in moment occurs despite the slight increase in displacement in M3 (from 0.001 to 0.0041 cm), indicating that the energy dissipation mechanism in the damper reduces the need for bending moment in the beam. In other words, part of the energy that was stored as beam moment in M2 is dissipated as friction in the RFD in M3.

Brace axial force: Comparing the brace axial force between M2 (15 kN) and M3 (12 kN) shows a 20% reduction. This is one of the most important findings of this study: adding the RFD, without significantly reducing stiffness, considerably reduces the force transmitted to the braces. This feature is highly valuable in seismic design, because braces and their connections can be designed for a lower force while simultaneously increasing seismic safety.

4.3.3. Analysis of Velocity and Dynamic Stability

The velocity plots show that in Model M1, the velocity amplitude is relatively high (about 0.05 m/s) and velocity oscillations decay slowly (low damping). In Model M2, the velocity is very low (on the order of 0.002 m/s) and oscillations damp out quickly, but this damping is due to inherent structural damping, not a dissipative mechanism. In Model M3, the velocity amplitude is slightly higher than in M2 (about 0.005–0.01 m/s), but the rate at which oscillations decay is much faster. This behavior indicates that the equivalent damping provided by the RFD plays an effective role in reducing the settling time of the dynamic response. In practice, this means a reduction in the duration of structural vibration after the earthquake ends and a reduction in occupant discomfort.

4.3.4. Effect of Period and Frequency Content of the Earthquake

The El Centro earthquake has a rich frequency content in the range of 0.1 to 10 Hz. The first mode period of M1 (0.3247 s, equivalent to 3.08 Hz) lies within the effective excitation range of this earthquake. The periods of M2 and M3 (about 0.079 s, equivalent to 12.66 Hz) lie in the high frequency range of the earthquake, where the spectral acceleration is lower. Therefore, part of the response reduction in M2 and M3 is due to moving away from the resonance range. However, the reduction in brace axial force in M3 relative to M2 cannot be explained by the period change (the period of M3 is almost equal to that of M2) and is solely due to the equivalent damping of the damper.

5. Discussion

In this study, an equivalent linear model for the Rotational Friction Damper (RFD) based on the work energy equivalence principle was developed and implemented in ETABS software as a linear Link element with a rotational degree of freedom. The performance of this model was evaluated on a one story, one bay steel frame under the El Centro earthquake record and compared with two other common systems: an intermediate moment frame and a moment frame with a chevron brace. The main findings are as follows:

- Model M1 (moment frame) has the weakest seismic performance (largest displacement, largest moment, long lasting oscillations).
- Model M2 (chevron braced frame) drastically reduces displacement but transfers all earthquake energy as internal force to the braces. This system is excellent from the viewpoint of displacement control but is ineffective in reducing member forces.
- Model M3 (braced + RFD), by accepting a very slight increase in displacement (from 0.001 to 0.0041 cm – an increase that is negligible in practice), succeeds in reducing the brace axial force by 20% and the beam bending moment by 16.7% (compared to M2). This means an improvement in seismic performance without a noticeable reduction in stiffness.

Therefore, the Rotational Friction Damper not only does not increase displacement (the increase is so small that it is negligible in practice), but also, by dissipating energy, reduces the load on the primary structural members and improves dynamic stability. These characteristics make the RFD an attractive option for performance based seismic design, especially in structures where the goal is to maintain linear behavior of the primary members under design level earthquakes.

References

[1] Titirla, M.D. (2023). A State-of-the-Art Review of Passive Energy Dissipation Systems in Steel Braces. Buildings, *13*(4), 851. https://doi.org/10.3390/buildings13040851
[2] Soong, T.T., & Spencer, B.F. (2002). Supplemental Energy Dissipation: State-of-the-Art and State-of-the-Practice. Engineering Structures, *24*(3), 243-259. https://doi.org/10.1016/S0141-0296(01)00092-X
[3] Spencer, B.F., Jr., & Nagarajaiah, S. (2003). State of the art of Structural Control. Journal of Structural Engineering, *129*(7), 845-856. https://doi.org/10.1061/(asce)0733-9445(2003)129:7(845)
[4] Pall, A., & Pall, R. (2004). Performance Based Design Using Pall Friction Dampers – An Economical Design Solution. 13th World Conference on Earthquake Engineering.
[5] Tiwary, A., Tiwari, A., & Kumar, A. (2014). State-of-Art in Active, Semi-Active and Hybrid Control Systems for Tall Buildings. International Journal of Engineering Research and Applications, *4*(1), 1-5.
[6] DAMPTECH. (2023). Friction Dampers for Seismic Protection. Available online: www.damptech.com
[7] Pall, A.S., & Marsh, C. (1982). Seismic Response of Friction Damped Braced Frames. Journal of the Structural Division, *108*(6), 1313-1323. https://doi.org/10.1061/jsdeag.0005968
[8] Mualla, I.H., & Belev, B. (2002). Performance of Steel Frames with a New Friction Damper Device under Earthquake Excitation. Engineering Structures, *24*(3), 365-371. https://doi.org/10.1016/s0141-0296(01)00102-x
[9] Pall, A.S., Verganelakis, V., & Marsh, C. (1987). Friction-Dampers for Seismic Control of Concordia University Library Building. Proceedings of the 5th Canadian Conference on Earthquake Engineering, 191-200.

[10] Papadopoulos, P. (2012). New Nonlinear Anti-Seismic Steel Device for the Increasing the Seismic Capacity of Multi-Storey Reinforced Concrete Frames. The Structural Design of Tall and Special Buildings, *21*(10), 750-763. https://doi.org/10.1002/tal.648
[11] Javidan, M.M., & Kim, J. (2022). A Rotational Friction Damper-Brace for Seismic Design of Resilient Framed Structures. Journal of Building Engineering, *51*, 104248. https://doi.org/10.1016/j.jobe.2022.104248
[12] Mualla, I.H. (2015). Analysis, Design and Applications of Rotational Friction Dampers for Seismic Protection. Journal of Civil Engineering and Environmental Architecture, *62*(4), 335-346.
[13] Javidan, M.M., & Kim, J. (2019). Seismic Retrofit of Soft-First-Story Structures Using Rotational Friction Dampers. Journal of Structural Engineering, *145*(12), 04019162. https://doi.org/10.1061/(ASCE)ST.1943-541X.0002433
[14] Sano, T., Shirai, K., Suzui, Y., & Utsumi, Y. (2019). Loading Tests of a Brace-Type Multi-Unit Friction Damper using Coned Disc Springs and Numerical Assessment of its Seismic Response Control Effects. Bulletin of Earthquake Engineering, *17*, 5365-5391.
[15] Veismoradi, S., Yousef-beik, S.M.M., Zarnani, P., & Quenneville, P. (2021). Development and Parametric Study of a New Self-Centering Rotational Friction Damper. Engineering Structures, *235*, 112097. https://doi.org/10.1016/j.engstruct.2021.112097
[16] Oliaei, M., Mashhadiyan, M., & Forootan, R. (2023). Seismic Performance Evaluation of Friction Damper and Yielding Metallic Damper in Steel Frame. Journal of Civil Engineering Researchers, *5*(3), 1–14. https://doi.org/10.61186/JCER.5.3.1
[17] Mahdizade, A., & Rakhshandeh Abadi, M. (2017). Structural Analysis and Design of a 30‐Story Tower with Friction Dampers. Journal of Civil Engineering Researchers, *7*(4), 68–77.
[18] Tahara, S., Iwaya, K., Iwashita, T., Goto, K., & Yamanari, M. (2024). Strength Estimation and Fundamental Characteristics of the New Rotational Friction Damper with Translational Movement. Machines, *12*(1), 15. https://doi.org/10.3390/machines12010015
[19] Filiatrault, A., & Cherry, S. (1990). Seismic Design Spectra for Friction-Damped Structures. Journal of Structural Engineering, *116*(5), 1334-1355. https://doi.org/10.1061/(asce)0733-9445(1990)116:5(1334)
[20] Sui, W., Wang, X., & Wang, Z. (2021). Experimental Study on Mechanical Properties of the Steel Friction Pads used in a Rotational Friction Damper. Structures, *29*, 1808-1818. https://doi.org/10.1016/j.istruc.2020.11.079

Journal of Civil Engineering Researchers

Journal homepage: www.journals-researchers.com

Evaluation of the Effect of Rice husk ash on the Mechanical Properties and Gamma Ray Attenuation of Concrete

Shahin Charkhtab Moghaddam,[a,*] Morteza Jamshidi[b]

[a] *Department of Civil Engineering, Deylaman Institute of Higher Education, Iran.*

[b] *Department of Civil Engineering, Cha.C., Islamic Azad University, Chalus, Iran.*

ABSTRACT

This study investigated the viability of rice husk ash (RHA) as a sustainable and performance-enhancing partial substitute for cement in concrete. The used RHA, characterized by a novel chemical composition abundant in silicon and aluminum oxides, was incorporated into ordinary concrete at increasing substitution ratios up to 25%. A comprehensive evaluation was conducted to assess the influence of RHA on various properties of the resulting concrete, including physical (setting time, standard consistency, workability), mechanical (compressive and tensile strength), microstructural (XRD, and EDX), and radiation shielding characteristics. The results indicated that RHA marginally increased cement setting time, with a maximum 7.14% increase observed at a 25% replacement level. However, it significantly increased water demand for standard consistency, reaching 35.7% at 25% replacement. The increased water demand correlated with a reduction in workability, with a maximum slump reduction rate of 57.3% at the 25% replacement level. Importantly, the optimal replacement levels for mechanical strength enhancement were at 10% for compressive strength and 15% for tensile strength, achieving improvements of 13.74% and 9.48%, respectively. Additionally, The Monte Carlo simulation code as well as PhyX software were employed for assessing the concrete samples' significant gamma and fast neutron radiation attenuation characteristics. Gamma-ray attenuation tests demonstrated a modest improvement in the gamma-ray shielding capacity of the resulting concrete. The linear attenuation of the prepared sample containing 15% RHA was found to be higher than the other samples, due to its high density. On the contrary, the 25RHA sample is a less valuable sample. The 15RHA sample had the highest value for FCS (0.090 cm-1) indicating its efficacy and capability as a neutron shield.

ARTICLE INFO

Received: November 02, 2025
Accepted: December 14, 2025

Keywords:
Rice husk ash Equivalent Linear
Mechanical properties Scaled
Microstructure
Radiation shielding
Linear attenuation coefficient

DOI: 10.66224/JCER.8.2.15
DOR: 20.1001.1.2538516.2026.8.2.2.7

1. Introduction

Rising global temperatures provide compelling evidence of ongoing climate change, with carbon dioxide (CO_2) emissions widely recognized as a principal driving factor in this process. [1]. The construction industry represents a major contributor to global carbon emissions, thereby requiring focused research into robust mitigation pathways. Throughout the construction value chain, CO_2 is emitted during raw material extraction, mechanical and thermal processing, and the inherently carbon‑intensive production of cement. [2]. As an essential pillar of the construction and infrastructure industry, cement production encounters significant pressures, including

* Corresponding author. e-mail: charkhtab.shahin@iauc.ac.ir

diminishing fossil fuel reserves, limited raw material availability, escalating global demand, and increasing environmental scrutiny. With an estimated 7% share of global CO_2 emissions, the cement sector is recognized as a substantial contributor to climate change. The Intergovernmental Panel on Climate Change (IPCC) has identified carbon capture and storage (CCS) as a promising mitigation technology capable of reducing CO_2 emissions from cement manufacturing.[3].

CCS encompasses the capture of CO2 from point sources, such as cement kilns, its transportation via pipelines or other means, and its long-term geological storage in suitable formations, such as depleted oil and gas reservoirs, thereby preventing its release into the atmosphere. However, the widespread deployment of CCS is currently hindered by significant economic barriers, including high capital and operational costs, and substantial energy requirements for capture and compression, which can reduce the overall efficiency of the industrial process[4].Biochar is a carbon-rich solid material, produced via thermochemical conversion (pyrolysis) of biomass under oxygen-limited conditions, offering a promising avenue for carbon sequestration [5]. Its highly porous structure and recalcitrant nature enable the long-term stabilization of carbon, effectively removing it from the active carbon cycle. Biochar is widely used as an environmentally friendly material in a variety of applications. For instance, wood-based biochar is commonly used for wastewater treatment for removing heavy metals and carbon sequestration due to its high carbon content and porous structure [6], while rice husk ash is widely applied as a soil amendment [7] and as a supplementary cementitious material in concrete. Corn cob biochar is often utilized as a soil ameliorant, as well as in fuel cells and bio composites material [8], whereas bamboo biochar, known for its excellent adsorptive properties, is ideal for air and water purification systems [9]. Similarly, coconut shell biochar is frequently employed in biodiesel production and capacitive deionization [10]. These diverse types of biochar cater to a wide range of industrial, agricultural, and environmental applications, highlighting their versatility and importance.

Incorporating biochar into cementitious materials offers a dual benefit: it reduces the embodied carbon footprint of concrete by partially replacing cement clinker, a major source of CO2 emissions, and can also enhance certain properties, such as workability, strength, and durability, depending on the biochar feedstock, production conditions, and incorporation rate [11]. While some studies report improvements in compressive strength, others observe a decrease, highlighting the importance of optimizing biochar properties and mix design [12]. The physicochemical properties of biochar, including elemental composition, stability, surface area, and functional groups, are significantly influenced by its origin and processing conditions (eg. pyrolysis temperature) [13]. The chemical composition of biochar—predominantly carbon, hydrogen, oxygen, nitrogen, and sulfur, with trace minerals such as potassium, phosphorus, and calcium—is fundamentally dictated by the feedstock characteristics and the specific pyrolysis parameters. As a thermal degradation process occurring under oxygen-limited conditions, pyrolysis parameters like temperature and heating rate are key determinants of biochar’s final properties. Specifically, low-temperature pyrolysis (typically 300–450 °C) yields biochar characterized by a higher volatile matter content and a less developed aromatic framework. These materials typically exhibit higher H/C and O/C molar ratios, reflecting a predominantly aliphatic nature Conversely, [14]pyrolysis at higher temperatures (above 600 °C) promotes greater carbonization and the formation of more condensed aromatic structures.

As a result, biochars produced under these conditions typically exhibit higher fixed carbon content, increased porosity, larger surface area, and a greater degree of ordered graphitic domain development. In addition, the H/C and O/C molar ratios decrease with rising pyrolysis temperature, indicating the progressive loss of hydrogen- and oxygen-containing functional groups [15].This structural variability, which can range from relatively amorphous to more graphitic forms, sets biochar apart from the highly ordered crystalline structure of graphene. This distinction is essential for understanding biochar’s wide range of applications, since variations in structure lead to differences in properties such as adsorption, reactivity, and stability[16].

The use of diverse biochar types in concrete has been the subject of numerous investigations, with a focus on their impact on physical, mechanical, and microstructural characteristics. Table 1 presents the key findings of several studies on the various properties of concrete.This study introduces a novel rice husk ash as a potential concrete admixture. The key innovation is the biochar's unique chemical composition, characterized by a substantially higher content of silicon and aluminum oxides, exceeding 43% by the total weight and approximately 92% of the mineral weight.

This contrasts sharply with conventional rice husk ash s used in previous research, where these oxides constituted less than 20% [17-19]. This elevated silicon and aluminum oxide content is expected to enhance the concrete's pozzolanic activity, leading to improved strength, durability, and microstructure. Beyond the unique chemical composition of the RHA, this study's novelty lies also in the comprehensive investigation of the resulting concrete's radiation shielding properties to provide novel insights into fast neutrons and gamma ray attenuation behavior of RHA-amended concrete.

Table 1.
Properties of concrete incorporating various types of biochar powders in literature studies.

Reference	Biochar type	Optimum replacement / addition ratio	Main conclusions	Other notes
Akhtar& Sarmah (2018) [1]	Pulp and paper mill residues Rice husk	0.1% of the total volume.	A growing body of research has demonstrated that biochar can substantially enhance the mechanical and durability performance of cementitious materials, although the magnitude and direction of improvement depend on biochar type, particle size, and dosage. At early ages, compressive strength improvements of 10% and 6% were reported with pulp-and-paper mill biochar and rice husk ash (RHA), respectively, while flexural strength increased by up to 20% with the incorporation of poultry litter or RHA at a 0.1% dosage. Wood-derived biochar at 0.5 wt% yielded notable compressive strength enhancements of 17% at 7 days and 16% at 28 days, and at higher dosages of 1–2 wt% it also mitigated thermal degradation, achieving 20% higher strength retention upon exposure to elevated temperatures. Similarly, wheat straw biochar improved both strength and durability: mortars containing 0.5–1.5 wt% showed compressive strength gains of 4.1–17.3%, a 9% increase in flexural strength, and substantial reductions in sorptivity (33.8%) and water absorption (25%).	The incorporation of rice husk ash (RHA) at a concentration of 0.1% produced a slight increase in splitting tensile strength, while also contributing to a modest reduction in production costs through partial cement substitution. In terms of thermal resistance, concrete containing 2% biochar exhibited up to a 45% improvement in impermeability after exposure to 550 °C. Similarly, the addition of 1% biochar enhanced water tightness, reducing capillary absorption and water penetration by 28% and 43%, respectively, relative to the control mix. Energy-dispersive spectroscopy (EDS) of wheat-straw-biochar mortars suggested the potential formation of additional hydration products, consistent with observed reductions of 30% and 31% in total and permeable air void volumes at a 1.5% dosage.
Gupta et al (2020) [19]	Wood waste	0.5% of cement weight.	Biochar contents between 2 wt% and 6.5 wt% have frequently yielded optimal strength improvements. For example, 2 wt% bagasse biochar increased compressive strength by 18%, attributed to its high silica content (16.62%) and fine particle size, while 6.5 wt% biochar produced compressive strength gains of 32.9% and 35.2% at 7 and 28 days, respectively. However, exceeding the optimal dosage often resulted in reduced splitting tensile strength or diminishing returns. Long-term studies further showed that 2 wt% biochar improved compressive strength by 3%, 7%, and 9% at curing ages of 28 days, 1 year, and 2 years, respectively, with additional reductions in sorptivity and water absorption linked to internal densification effects.	Biochar dosage had varying effects on water absorption: while optimal amounts reduced sorptivity and improved microstructure through particle densification, increases in biochar content were also associated with higher overall water absorption. Comparative evaluation of different biochars showed that their effectiveness in modifying cementitious materials followed the order: bagasse > rice husk > peanut husk > coconut husk > wheat husk. The reduction in water absorption and sorptivity was consistent with decreased workability at higher biochar contents, attributable to the hydrophilic and porous nature of the material.
Ahmad et al (2020) [20]	Wheat straw	1.5% of cement weight.	Biochar also enhances microstructural development. XRD, SEM, FTIR, EDX, and Raman analyses have consistently confirmed increased formation of hydration products, improved matrix densification, and reduced pore connectivity. In bamboo biochar mortars, the high silicon and aluminum oxide content imparted a pozzolanic effect, resulting in a 32.9% increase in early-age strength and improved crack resistance at 1–3 wt% replacement. Wood-waste biochar with increased fineness produced optimal reductions in carbonation depth (17.9%) and chloride diffusion (32%) at 1–3 wt%, while simultaneously increasing compressive strength by 18.48%. Likewise, corn straw biochar at 1 wt% increased compressive strength by 5.3%, and at 3 wt% improved peak load by up to 11.4% and initial fracture toughness by as much as 46.8% across multiple curing ages.	Specific biochar types demonstrated specialized functional benefits. For example, bamboo biochar exhibited a strong pozzolanic effect due to its high silicon and aluminum oxide content. A 1 wt% replacement was identified as optimal for maximizing crack resistance, while dosages between 1% and 3% consistently improved compressive strength and fracture toughness through filling and self-curing effects. Wood-waste biochar at a 3% replacement level enhanced cement hydration and microstructure by providing nucleation sites and filling internal pores, as evidenced by SEM and XRD analyses. However, biochar incorporation also reduced ductility and fracture energy; a 3 wt% addition decreased fracture energy by 3.6%, 33.3%, and 33.2% at 7, 14, and 28 days, respectively.

Continued on next page

Reference	Biochar type	Optimum replacement / addition ratio	Main conclusions	Other notes
Qin et al (2021) [21]	Synthetic eucalyptus plywood	6.5% of cement weight.	Durability performance also benefits from biochar incorporation. After exposure to temperatures of 300–700 °C, mixtures containing 3% RHA exhibited residual strength increases of 4.8%, 26.3%, and 25%, respectively. Concrete with 2 wt% biochar showed up to 45% improved impermeability after heating to 550 °C, and 1 wt% biochar reduced capillary absorption and water penetration by 28% and 43%. Biochars with strong pozzolanic characteristics, such as alum sludge biochar, further improved durability: the 5% replacement achieved a compressive strength of 31 MPa and reduced global warming potential by 32.2%. Across 16 different biochar types, milled biochars used at 10% replacement often matched or exceeded control strengths, with white hardwood biochar outperforming the control by more than 48%.	Biochar also influenced fresh properties. Increasing its dosage raised the water demand for normal consistency and shortened setting time, with large replacements (e.g., 30%) resulting in minimal slump and sharply reduced plasticity. Nevertheless, the optimal RHA content of 3 wt% enhanced micro-filling and secondary hydration, increasing 28-day compressive, splitting tensile, and flexural strengths by 9.9%, 7.2%, and 6.8%, respectively. The pozzolanic reactivity of alum-sludge biochar was likewise confirmed analytically. Moreover, studies showed that a wide range of milled biochars can effectively replace up to 10% of cement without compromising strength.
Javed et al (2022) [18]	Bagasse Coconut husk Peanut husk Rice husk Wheat husk	2% of cement weight.	In engineered cementitious composites, the incorporation of 10–20 wt% biochar increased tensile strain capacity and reduced crack width despite causing a moderate (~10%) reduction in compressive strength. However, this trade-off is accompanied by significant sustainability benefits, including up to 58.3% reductions in carbon emissions and lower production costs due to reduced cement use and potential carbon-tax savings.	In broader sustainability assessments, incorporating biochar reduced total and specific carbon emissions by as much as 58.3%, while lowering production costs due to reduced cement consumption and potential carbon-tax savings. These combined mechanical, durability, and environmental benefits demonstrate that biochar additions of 10–20% can offer a cost-effective, sustainable, and structurally reliable alternative for modern construction applications.
Sirico et al (2022) [22]	Forestry waste residues	2% of cement weight.	Overall, the literature demonstrates consistent evidence that biochar—across diverse feedstocks and processing conditions—can improve the mechanical performance, durability, microstructure, and sustainability profile of cementitious materials when used at appropriate dosages, typically between 1% and 6%.	The incorporation of rice husk ash (RHA) at a concentration of 0.1% produced a slight increase in splitting tensile strength, while also contributing to a modest reduction in production costs through partial cement substitution. In terms of thermal resistance, concrete containing 2% biochar exhibited up to a 45% improvement in impermeability after exposure to 550 °C. Similarly, the addition of 1% biochar enhanced water tightness, reducing capillary absorption and water penetration by 28% and 43%, respectively, relative to the control mix. Energy-dispersive spectroscopy (EDS) of wheat-straw-biochar mortars suggested the potential formation of additional hydration products, consistent with observed reductions of 30% and 31% in total and permeable air void volumes at a 1.5% dosage.
Liu et al (2022) [23]	Bamboo biochar	4% of cement weight.	A growing body of research has demonstrated that biochar can substantially enhance the mechanical and durability performance of cementitious materials, although the magnitude and direction of improvement depend on biochar type, particle size, and dosage. At early ages, compressive strength improvements of 10% and 6% were reported with pulp-and-paper mill biochar and rice husk ash (RHA), respectively, while flexural strength increased by up to 20% with the incorporation of poultry litter or RHA at a 0.1% dosage. Wood-derived biochar at 0.5 wt% yielded notable compressive strength enhancements of 17% at 7 days and 16% at 28 days, and at higher dosages of 1–2 wt% it also mitigated	Biochar dosage had varying effects on water absorption: while optimal amounts reduced sorptivity and improved microstructure through particle densification, increases in biochar content were also associated with higher overall water absorption. Comparative evaluation of different biochars showed that their effectiveness in modifying cementitious materials followed the order: bagasse > rice husk > peanut husk > coconut husk > wheat husk. The reduction in water absorption and sorptivity was consistent with decreased workability at higher biochar contents, attributable to the hydrophilic and porous nature of the material.

Continued on next page

Reference	Biochar type	Optimum replacement / addition ratio	Main conclusions	Other notes
			thermal degradation, achieving 20% higher strength retention upon exposure to elevated temperatures. Similarly, wheat straw biochar improved both strength and durability: mortars containing 0.5–1.5 wt% showed compressive strength gains of 4.1–17.3%, a 9% increase in flexural strength, and substantial reductions in sorptivity (33.8%) and water absorption (25%).	
Ling et al (2023) [24]	Wood waste	3% of cement weight.	Biochar contents between 2 wt% and 6.5 wt% have frequently yielded optimal strength improvements. For example, 2 wt% bagasse biochar increased compressive strength by 18%, attributed to its high silica content (16.62%) and fine particle size, while 6.5 wt% biochar produced compressive strength gains of 32.9% and 35.2% at 7 and 28 days, respectively. However, exceeding the optimal dosage often resulted in reduced splitting tensile strength or diminishing returns. Long-term studies further showed that 2 wt% biochar improved compressive strength by 3%, 7%, and 9% at curing ages of 28 days, 1 year, and 2 years, respectively, with additional reductions in sorptivity and water absorption linked to internal densification effects.	Specific biochar types demonstrated specialized functional benefits. For example, bamboo biochar exhibited a strong pozzolanic effect due to its high silicon and aluminum oxide content. A 1 wt% replacement was identified as optimal for maximizing crack resistance, while dosages between 1% and 3% consistently improved compressive strength and fracture toughness through filling and self-curing effects. Wood-waste biochar at a 3% replacement level enhanced cement hydration and microstructure by providing nucleation sites and filling internal pores, as evidenced by SEM and XRD analyses. However, biochar incorporation also reduced ductility and fracture energy; a 3 wt% addition decreased fracture energy by 3.6%, 33.3%, and 33.2% at 7, 14, and 28 days, respectively.
Qing et al (2023) [25]	Corn straw	1-3% of cement weight.	Biochar also enhances microstructural development. XRD, SEM, FTIR, EDX, and Raman analyses have consistently confirmed increased formation of hydration products, improved matrix densification, and reduced pore connectivity. In bamboo biochar mortars, the high silicon and aluminum oxide content imparted a pozzolanic effect, resulting in a 32.9% increase in early-age strength and improved crack resistance at 1–3 wt% replacement. Wood-waste biochar with increased fineness produced optimal reductions in carbonation depth (17.9%) and chloride diffusion (32%) at 1–3 wt%, while simultaneously increasing compressive strength by 18.48%. Likewise, corn straw biochar at 1 wt% increased compressive strength by 5.3%, and at 3 wt% improved peak load by up to 11.4% and initial fracture toughness by as much as 46.8% across multiple curing ages.	Biochar also influenced fresh properties. Increasing its dosage raised the water demand for normal consistency and shortened setting time, with large replacements (e.g., 30%) resulting in minimal slump and sharply reduced plasticity. Nevertheless, the optimal RHA content of 3 wt% enhanced micro-filling and secondary hydration, increasing 28-day compressive, splitting tensile, and flexural strengths by 9.9%, 7.2%, and 6.8%, respectively. The pozzolanic reactivity of alum-sludge biochar was likewise confirmed analytically. Moreover, studies showed that a wide range of milled biochars can effectively replace up to 10% of cement without compromising strength.
Jia et al (2023) [26]	Municipal solid waste	1-10% of cement weight.	Durability performance also benefits from biochar incorporation. After exposure to temperatures of 300–700 °C, mixtures containing 3% RHA exhibited residual strength increases of 4.8%, 26.3%, and 25%, respectively. Concrete with 2 wt% biochar showed up to 45% improved impermeability after heating to 550 °C, and 1 wt% biochar reduced capillary absorption and water penetration by 28% and 43%. Biochars with strong pozzolanic characteristics, such as alum sludge biochar, further improved durability: the 5% replacement achieved a compressive strength of 31 MPa and reduced global warming potential by 32.2%. Across 16 different biochar types, milled biochars used at 10% replacement often matched or exceeded control strengths, with white hardwood biochar outperforming the control by more than 48%.	In broader sustainability assessments, incorporating biochar reduced total and specific carbon emissions by as much as 58.3%, while lowering production costs due to reduced cement consumption and potential carbon-tax savings. These combined mechanical, durability, and environmental benefits demonstrate that biochar additions of 10–20% can offer a cost-effective, sustainable, and structurally reliable alternative for modern construction applications.

Continued on next page

Reference	Biochar type	Optimum replacement / addition ratio	Main conclusions	Other notes
Pang et al (2024) [27]	Waste synthetic eucalyptus plywood boards	3% of cement weight.	In engineered cementitious composites, the incorporation of 10–20 wt% biochar increased tensile strain capacity and reduced crack width despite causing a moderate (~10%) reduction in compressive strength. However, this trade-off is accompanied by significant sustainability benefits, including up to 58.3% reductions in carbon emissions and lower production costs due to reduced cement use and potential carbon-tax savings.	The incorporation of rice husk ash (RHA) at a concentration of 0.1% produced a slight increase in splitting tensile strength, while also contributing to a modest reduction in production costs through partial cement substitution. In terms of thermal resistance, concrete containing 2% biochar exhibited up to a 45% improvement in impermeability after exposure to 550 °C. Similarly, the addition of 1% biochar enhanced water tightness, reducing capillary absorption and water penetration by 28% and 43%, respectively, relative to the control mix. Energy-dispersive spectroscopy (EDS) of wheat-straw-biochar mortars suggested the potential formation of additional hydration products, consistent with observed reductions of 30% and 31% in total and permeable air void volumes at a 1.5% dosage.
Mekky et al (2024) [28]	Alum sludge	5% of cement weight.	Overall, the literature demonstrates consistent evidence that biochar—across diverse feedstocks and processing conditions—can improve the mechanical performance, durability, microstructure, and sustainability profile of cementitious materials when used at appropriate dosages, typically between 1% and 6%.	Biochar dosage had varying effects on water absorption: while optimal amounts reduced sorptivity and improved microstructure through particle densification, increases in biochar content were also associated with higher overall water absorption. Comparative evaluation of different biochars showed that their effectiveness in modifying cementitious materials followed the order: bagasse > rice husk > peanut husk > coconut husk > wheat husk. The reduction in water absorption and sorptivity was consistent with decreased workability at higher biochar contents, attributable to the hydrophilic and porous nature of the material.
Hylton et al (2024) [29]	16 various biochar types	10% of cement weight.	A growing body of research has demonstrated that biochar can substantially enhance the mechanical and durability performance of cementitious materials, although the magnitude and direction of improvement depend on biochar type, particle size, and dosage. At early ages, compressive strength improvements of 10% and 6% were reported with pulp-and-paper mill biochar and rice husk ash (RHA), respectively, while flexural strength increased by up to 20% with the incorporation of poultry litter or RHA at a 0.1% dosage. Wood-derived biochar at 0.5 wt% yielded notable compressive strength enhancements of 17% at 7 days and 16% at 28 days, and at higher dosages of 1–2 wt% it also mitigated thermal degradation, achieving 20% higher strength retention upon exposure to elevated temperatures. Similarly, wheat straw biochar improved both strength and durability: mortars containing 0.5–1.5 wt% showed compressive strength gains of 4.1–17.3%, a 9% increase in flexural strength, and substantial reductions in sorptivity (33.8%) and water absorption (25%).	Specific biochar types demonstrated specialized functional benefits. For example, bamboo biochar exhibited a strong pozzolanic effect due to its high silicon and aluminum oxide content. A 1 wt% replacement was identified as optimal for maximizing crack resistance, while dosages between 1% and 3% consistently improved compressive strength and fracture toughness through filling and self-curing effects. Wood-waste biochar at a 3% replacement level enhanced cement hydration and microstructure by providing nucleation sites and filling internal pores, as evidenced by SEM and XRD analyses. However, biochar incorporation also reduced ductility and fracture energy; a 3 wt% addition decreased fracture energy by 3.6%, 33.3%, and 33.2% at 7, 14, and 28 days, respectively.
Wang et al (2025) [30]	Peanut shell-based biomass	10-20% of cement weight.	Biochar contents between 2 wt% and 6.5 wt% have frequently yielded optimal strength improvements. For example, 2 wt% bagasse biochar increased compressive strength by 18%, attributed to its high silica content (16.62%) and fine particle size, while 6.5 wt% biochar produced compressive strength gains of 32.9% and 35.2% at 7 and 28 days,	Biochar also influenced fresh properties. Increasing its dosage raised the water demand for normal consistency and shortened setting time, with large replacements (e.g., 30%) resulting in minimal slump and sharply reduced plasticity. Nevertheless, the optimal RHA

Continued on next page

Reference	Biochar type	Optimum replacement / addition ratio	Main conclusions	Other notes
			respectively. However, exceeding the optimal dosage often resulted in reduced splitting tensile strength or diminishing returns. Long-term studies further showed that 2 wt% biochar improved compressive strength by 3%, 7%, and 9% at curing ages of 28 days, 1 year, and 2 years, respectively, with additional reductions in sorptivity and water absorption linked to internal densification effects.	content of 3 wt% enhanced micro-filling and secondary hydration, increasing 28-day compressive, splitting tensile, and flexural strengths by 9.9%, 7.2%, and 6.8%, respectively. The pozzolanic reactivity of alum-sludge biochar was likewise confirmed analytically. Moreover, studies showed that a wide range of milled biochars can effectively replace up to 10% of cement without compromising strength.

2. Materials Properties

2.1. Cement

In this study, Type I Ordinary Portland Cement (OPC) with a 42.5 N strength grade, conforming to ASTM C150 [31], was utilized. This OPC was sourced from Wadi El-Nile cement company. The physical and mechanical properties of the OPC are detailed in Table 2, while its chemical composition, determined via X-Ray Fluorescence (XRF) analysis, is presented in Table 3. Specific gravity was determined according to ASTM C188 [32]. The initial and final setting times, along with standard consistency, were evaluated using a Vicat apparatus (Figure 1(a)). Soundness was assessed using a Le Chatelier apparatus (Figure 1(b)) following BS EN 196-3:2005 [33]. Compressive strength testing was performed after 28 days of curing, in accordance with ASTM C109/C109M-11 [34], to verify the mechanical performance of the resulting concrete. Particle size distribution of the OPC, determined using laser scattering particle size analysis, is illustrated in Figure 1(c), revealing a mean particle size of approximately 9 µm. Mineralogical and microstructural characterization was conducted using X-ray diffraction (XRD) with the results presented in Figures 1(d). XRD analysis revealed the presence of the principal crystalline phases in Portland cement clinker: alite (C3S), belite (C2S), tricalcium aluminate (C3A), tetracalcium aluminoferrite (C4AF), and gypsum. This mineralogical profile, consistent with the chemical composition determined by XRF, demonstrates that the cement's composition is in accordance with the expected mineralogy for its type, thereby confirming its quality and compliance with relevant industry standards.

2.2. Aggregates

Natural siliceous sand, sampled in accordance with ASTM D75 [35], served as the fine aggregate in this study. Particle size distribution was determined through sieve analysis following ASTM C136 [34] to verify compliance with design specifications and standard limits. The results of the sieve analysis are presented in Figure 2(a). The calculated Fineness Modulus (FM) of 2.47 indicates a typical mean particle size, consistent with ASTM C33 requirements. The physical properties of the fine aggregate are summarized in Table 4. For coarse aggregates, crushed dolomite with a nominal maximum size 19 mm was used as the coarse aggregate in all concrete mixes. Gradation testing, essential for design compliance and adherence to standard limits, was performed using sieve analysis according to ASTM C136 [36], as shown in Figure 2(b). The physical properties of the coarse aggregate are summarized in Table 4. The crushing value was determined according to BS 812 Part 110 [37]. ASTM C128 [38]was used to determine specific gravity and absorption. Bulk density and voids content were measured according to ASTM C29 [39]. The content of fine materials was assessed according to ASTM C142 [40]. The procedures employed for determining the physical properties of the coarse aggregate are illustrated in Figures 2(c, d).

2.3. Water and superplasticizer

[Clean potable water conforming to the standards outlined in ASTM C1602/C1602M [41], was used for concrete specimen mixing and curing. On the other hand, biochar particles exhibit a high porosity and water absorption capacity, which can significantly affect the workability of concrete mixtures. The high porosity of biochar leads to increased water absorption, reducing the available free water in the mix and thus lowering concrete fluidity. To address this challenge and enhance workability, the addition of chemical admixtures, specifically superplasticizers (SP), is essential. These admixtures improve the distribution of biochar particles within the mix and counteract the negative effects of water absorption. A commercially available SP, Sikament NN, supplied by the Egyptian branch of Sika Company, was incorporated during mixing at a constant dosage of 1.05% by weight of water. This SP meets the requirements for Type (F) chemical admixtures as specified in ASTM C494 [42]. Key characteristics of the SP are presented in

Table 5. The inclusion of the SP was driven by concerns over the potential difficulty in achieving a uniform concrete mixture and the expected reduction in workability due to biochar's high-water absorption. Furthermore, the relatively low water-to-cement (w/c) ratio employed could also negatively impact mixture workability. Figure 3 shows the appearance of the used mixing and curing water in addition to the used SP.

2.4. Rice husk ash (RHA)

Biochar is a carbon‑rich material produced through the pyrolysis of organic biomass under oxygen‑limited conditions. During this thermochemical process, agricultural residues, wood chips, manure, or other lignocellulosic materials are heated to elevated temperatures, causing devolatilization and leaving behind a stable, carbon‑rich solid. The physicochemical properties of biochar are strongly influenced by the feedstock type and pyrolysis parameters, including temperature, heating rate, and residence time. Owing to its high carbon content and long-term stability, biochar offers substantial environmental benefits, particularly in carbon sequestration, reduction of greenhouse gas emissions, and climate change mitigation.

In this study, rice husk ash (RHA) is examined to assess its effects on the physical, mechanical, and—importantly for the first time—radiation‑shielding properties of concrete. RHA, shown after grinding in Figure 4(a), is derived from the pyrolysis of rice husks, an abundant byproduct of rice milling. The rice husk feedstock was pyrolyzed at temperatures exceeding 600 °C using a pilot‑scale continuous pyrolysis unit. The resulting biochar was subsequently analyzed by Eurofins Laboratories, an institution accredited under the European Biochar Certificate (ERHA). The comprehensive analysis included ultimate analysis (CHNSO) to determine organic carbon content and calculate H/C and O/C molar ratios as indicators of carbon stability. Additional parameters such as ash content, moisture content, trace metal concentrations, and polycyclic aromatic hydrocarbon (PAH) levels were also evaluated. A complete summary of the analytical results is presented in Appendix 1, detailing the methods used, ERHA reference thresholds, and results on both an as‑received and dry basis.

The RHA used in this study contains 44.8% organic carbon (dry basis) and exhibits good carbon stability, as reflected by an H/C_org ratio of 0.23. Although the ash content is relatively high (49.9%) compared with biochars derived from woody feedstocks, this characteristic is advantageous for construction applications due to its mineralogical composition. No ERHA‑based threshold limits apply to trace metals when biochar is used in construction materials, and the measured concentrations confirm that this RHA is suitable for building applications. PAH analysis further supports its suitability: the total concentration of the 16 EPA PAHs was only 2.2 mg/kg, and no detectable contamination was observed for the 8 EPA priority PAHs, benzo(e)pyrene, or benzo(j)fluoranthene.

The RHA employed in this investigation is characterized by a high silica content (Table 6), a porous microstructure, and a bulk density of approximately 1.3 g/cm³. Its pozzolanic reactivity makes it an effective partial cement substitute, with the material containing 43.2% silicon and aluminum oxides—equivalent to 92.37% of the mineral fraction of the ash when excluding carbon dioxide. These pozzolanic constituents react with calcium hydroxide in the cement matrix to form additional calcium–silicate–hydrate (C‑S‑H), thereby improving concrete strength and durability. Moreover, the high surface area and internal porosity of RHA enhance water retention, reduce permeability, and potentially increase resistance to cracking and environmental degradation. The use of RHA also contributes to sustainability by valorizing agricultural waste and reducing dependence on Portland cement.

Despite these advantages, several challenges remain. The quality of RHA can vary depending on the feedstock and pyrolysis conditions, influencing workability, consistency, and mechanical performance. High biochar contents may reduce workability due to increased water demand, making the use of superplasticizers or other admixtures necessary. The particle size distribution of the RHA used here is presented in Figure 4(b), with an average particle size of 17.5 µm. X‑ray diffraction analysis (Figure 4©) demonstrates the predominantly amorphous nature of the material. The broad diffraction band between 2θ = 15° and 25° corresponds to amorphous carbon with randomly oriented aromatic layers, consistent with observations reported by Dehkhoda et al. (2014).[43]. Additionally, the low intensity sharp peaks correspond to miscellaneous inorganic components identified by quartz, graphite and coquimbite minerals, where the coquimbite is a secondary sulfate mineral which occurs due to oxidation process of iron sulfide and crystallized during the biochar production process.

3. Experimental program and test setup.

3.1. Preliminary compressive strength test on RHA mortar

A preliminary compressive strength assessment was performed on 50 × 50 × 50 mm cement mortar cubes (Figure 5) at a curing age of 28 days to evaluate the feasibility of the selected RHA replacement ratios prior to their use as partial cement substitutes in concrete. The mortar mixtures were prepared in accordance with ASTM C109/C109M, using a cement to sand ratio of 1:2.75 by weight and a water to cement ratio of 0.485. As shown in Figure 6, the highest compressive strength was achieved at a 15% RHA replacement level, corresponding to an 8.71% increase relative to the control specimen. However, replacement levels exceeding 20% adversely affected strength development; at 25% substitution, the compressive strength decreased by 2.07% compared to the control mix. These findings confirm that the selected RHA replacement ratios are appropriate for subsequent incorporation into concrete mixtures.

3.2. Concrete mix design

The experimental program was designed to develop and evaluate ordinary concrete mixtures to investigate the mechanical, physical, and radiation shielding performance of rice husk ash (RHA) when used as a partial cement replacement. All concrete mixtures were proportioned according to the ACI 211.1 methodology to ensure consistency and reliable comparison among mixes. For the control mixture, the material quantities per cubic meter (1 m^3) were 380 kg of cement, 1190 kg of coarse aggregate, 720 kg of fine aggregate, and 142.5 kg of water, as detailed in Table 7. A water to cement (w/c) ratio of 0.375 was selected to achieve an appropriate balance between strength and workability. Additionally, a superplasticizer (SP) dosage of approximately 1.05% by water weight was incorporated to enhance mixture fluidity and ensure adequate homogeneity during casting.

RHA was incorporated into the concrete at five progressively increasing replacement levels, up to a maximum of 25%, enabling a systematic assessment of its influence on concrete performance. The selected range of substitution ratios is consistent with recent research investigating higher biochar based replacement levels in cementitious composites.[29, 30].

The use of higher RHA substitution rates is supported by the increasing recognition of biochar as a multifunctional, sustainability enhancing material. As a biomass derived product, biochar contributes to carbon sequestration: atmospheric carbon fixed during plant growth becomes stabilized through pyrolysis, enabling long term carbon storage when incorporated into concrete. Its utilization also promotes waste valorization, since materials such as rice husks—commonly disposed of or openly burned—are converted into value added products, thereby reducing environmental pollution and supporting circular economy initiatives.

Nevertheless, the mechanical and physical performance of concrete incorporating RHA must be carefully optimized. Elevated replacement levels can negatively affect strength and workability due to the material's high surface area, increased water absorption, and reduced effective binder content. Accordingly, the present experimental program sought to balance the sustainability advantages of higher RHA substitution with the need to maintain acceptable fresh and hardened concrete properties.

3.3. Specimens' preparation and curing

To evaluate the mechanical performance of concrete incorporating rice husk ash (RHA), compressive and tensile strength tests were performed on specimens of standard laboratory dimensions. For compressive strength determination, concrete cubes measuring 100 × 100 × 100 mm were cast, while cylindrical specimens with a diameter of 100 mm and a height of 200 mm were prepared for tensile strength testing.

The mixing procedure was designed to ensure uniform material dispersion and consistency across all mixtures. Coarse and fine aggregates were first blended for two minutes, after which cement and RHA were added and mixed for an additional two minutes. The predetermined quantity of water, incorporating the liquid superplasticizer (SP), was then introduced, and mechanical mixing continued for a further three minutes to achieve proper homogenization.

Immediately after casting, the mixtures were compacted using a mechanical vibrator to eliminate air voids and ensure surface uniformity. The specimens remained in their molds for 24 hours before being demolded and placed in a curing tank containing potable water at ambient temperature and a relative humidity of at least 90%. Curing was maintained for approximately 27 days.

Following curing, all specimens were removed and oven dried at 105 °C for two hours to eliminate residual moisture before being subjected to gamma radiation attenuation testing. Mechanical property measurements were subsequently performed on the same specimens the day after completion of the radiation shielding experiments.

3.4. Tests setup

3.4.1. Physical properties of fresh concrete

To elucidate the impact of incorporating rice husk ash (RHA) biochar as a partial cement substitute, the fresh properties of the concrete mixtures were systematically evaluated and compared against a control mix. The investigation focused on standard consistency, initial and final setting times, and slump performance, providing a comprehensive assessment of the material's influence on concrete workability and rheological behavior.

Owing to the highly porous microstructure of biochar, which typically increases water demand and absorption, its inclusion can significantly alter the effective water-to-cement ratio and the rate of hydration. Consequently, this study addresses these factors to clarify how biochar modifies the fresh-state characteristics and to determine its implications for practical construction applications.

Standard consistency—representing the water content required for a cement paste to reach a specified degree of stiffness—and setting times—which mark the duration required for the paste to achieve defined levels of rigidity—were determined using a Vicat needle apparatus. These measurements were conducted in accordance with ASTM C191 guidelines. Additionally, the workability of the concrete mixtures was assessed via the slump test to evaluate the effect of RHA replacement levels on the fluidity and consistency of the fresh concrete. [44]. On the other hand, the slump cone test was conducted in accordance with the procedures specified in ASTM C143/C143M [45]. This test employed a standard slump cone with a height of 300 mm, a top diameter of 100 mm, and a base diameter of 200 mm.

(a)

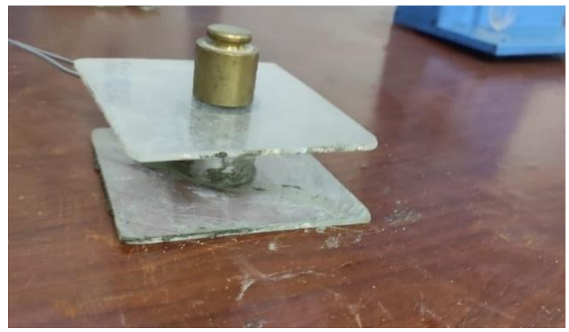

(b)

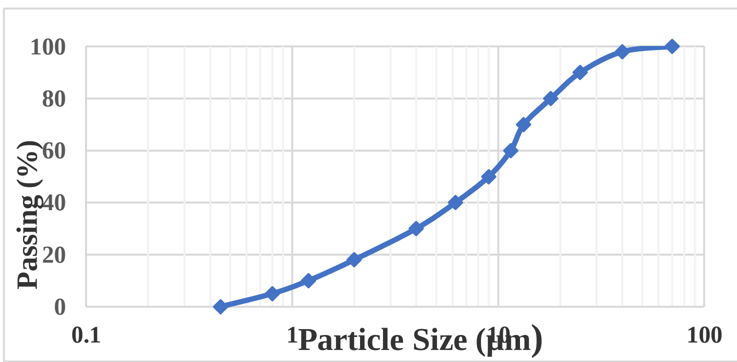

(c)

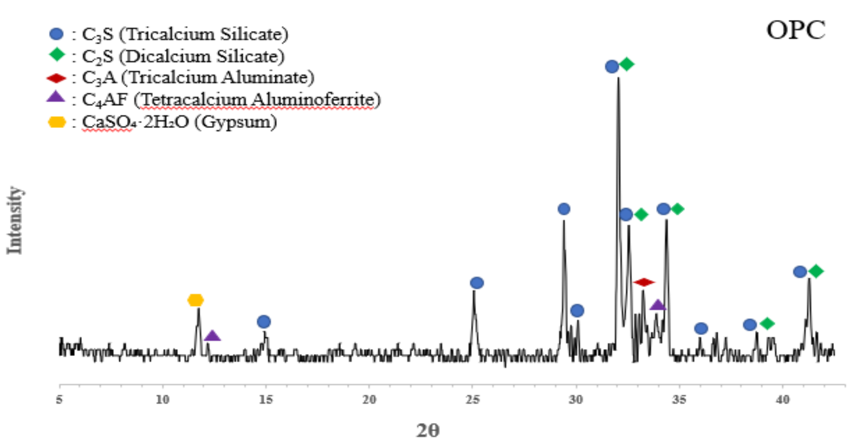

(d)

Figure 1: (a) Vicat apparatus, (b) le chatelier instrument, (c) particle size distribution of cement, (d) XRD pattern of the used cement.

Table 2.
Properties of used cement

Physical properties							Mortar compressive strength (MPa)		
Color	Specific gravity	Initial setting time (min)	Final setting time (min)	Surface area(cm^2/g)	Standard consistency (w/c%)	Soundness (mm)	3 days	7 days	28 days
Grey	3.16	120	210	3550	28%	1	25	33	43

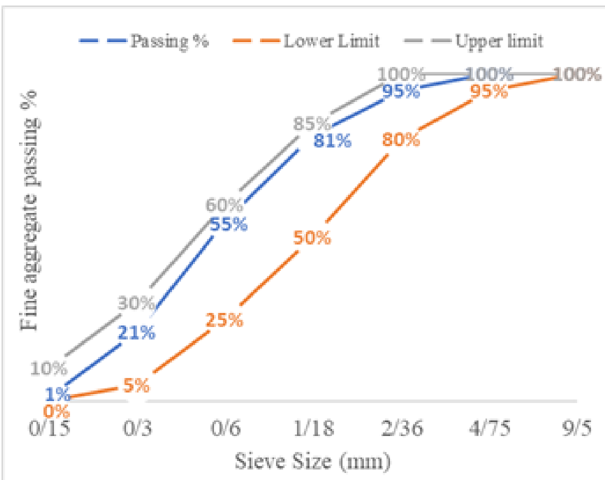

(a)

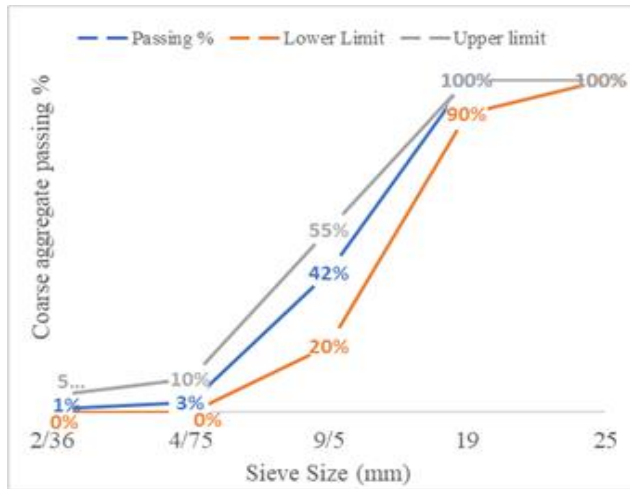

(b)

(c)

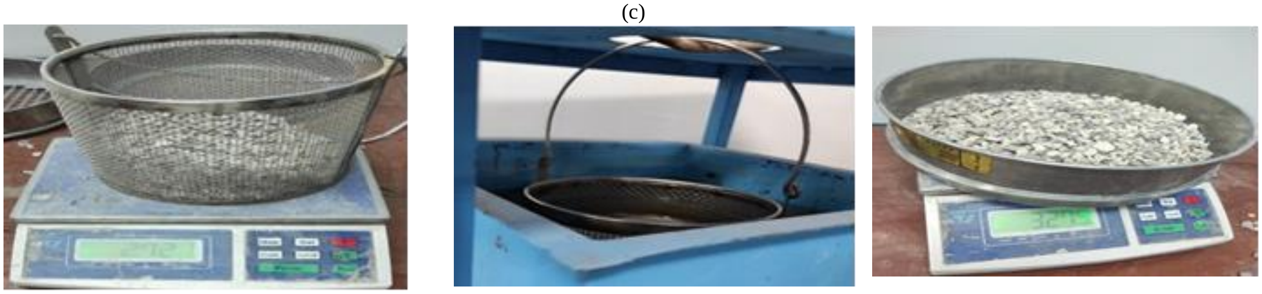

(d)

Figure 2. (a) Particle size distribution of sand, (b) particle size distribution of dolomite, (c) crushing test of dolomite, and (d) absorption test of dolomite.

Table 3.
Chemical composition of used cement (% mass)

SiO_2	CaO	Al_2O_3	Fe_2O_3	MgO	SO_3	Na_2O	P_2O_5	Cl	TiO_2	LOI*
21.52	61.89	3.8	1.88	2.26	2.81	0.55	0.21	0.14	0.51	3.11

* LOI: Loss on Ignition at 1000 ◦C.

Table 4.
Physical properties of the used aggregates.

Property	Specific gravity	Bulk density (kg/m3)	Voids (%)	Absorption (%)	Clay and fine materials (%)	Crushing Value (%)	Fineness modulus
Fine Aggregate	2.55	1745	31.6	0.8	1	--	2.47
Coarse Aggregate	2.68	1675	37.5	0.45	0.5	19	--

Table 5.
properties of the used superplasticizer.

Manufacturer's recommended ratio	Color	Raw material	Density	PH value	Solid content ratio	Category
1% to 3% of water weight	Dark Brown Liquid	Sulfonated Naphthalene Formaldehyde	1.2 kg/L	(8.5 ± 1)	30%	high-range water reducer derived from modified polycarboxylates

Table 6.
Chemical composition of RHA powder (% mass).

SiO_2	CaO	Al_2O_3	Fe_2O_3	MgO	K_2O	Na_2O	SO_3	P_2O_5	Cl	LOI
26.30	0.33	16.90	0.17	0.29	1.16	0.27	0.68	0.27	0.40	53.20

Table 7.
Mix design of the investigated RHA concrete mixes in (kg/m3).

Mix description	ID	Cement (kg)	Aggregate (kg)		Water (lit)	SP (kg)	RHA (kg)
			dolomite	sand			
Control mix	CO	380	1190	720	142.5	1.5	-
5% RHA	5RHA	361	1190	720	142.5	1.5	19
10% RHA	10RHA	342	1190	720	142.5	1.5	38
15% RHA	15RHA	323	1190	720	142.5	1.5	57
20% RHA	20RHA	304	1190	720	142.5	1.5	76
25% RHA	25RHA	285	1190	720	142.5	1.5	95

(a)

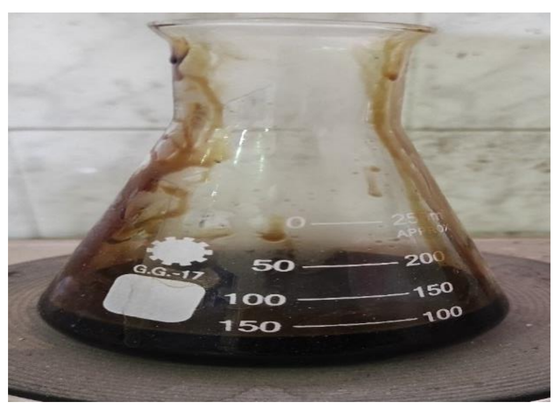

(b)

Figure 3. (a) Mixing and curing water, and (b) the used SP (Sikament NN).

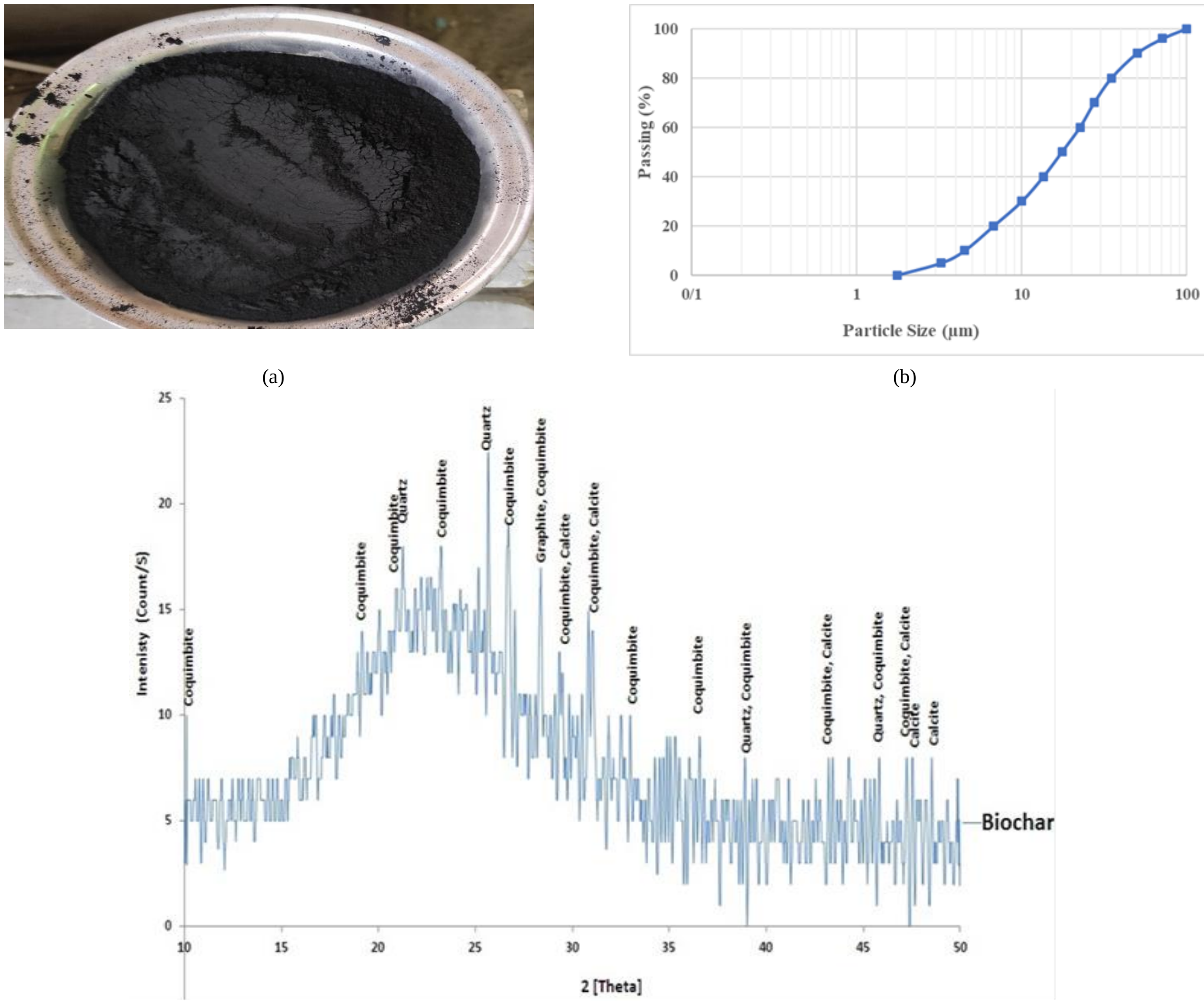

(a) (b)
(c)

Figure 4. (a) Appearance of RHA powder after grinding, (b) Particles size distribution of RHA, and (c) XRD patterns of RHA powder.


Figure 5. Sample of RHA mortar and concrete cubes.

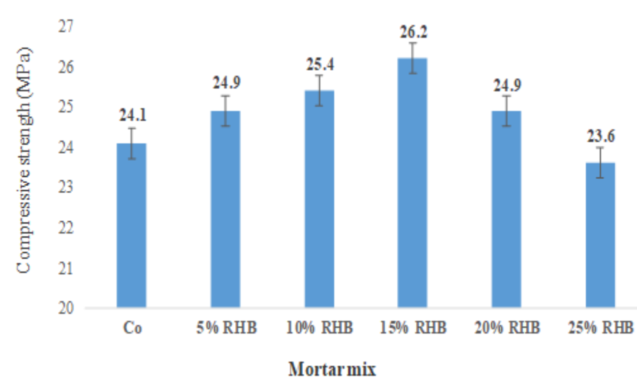

Figure 6. Compressive strength of mortar cubes

3.4.2. Mechanical properties

The compressive strength of the concrete mixtures incorporating different RHA replacement ratios was determined using standard cube specimens measuring 100 × 100 × 100 mm. For each mix, three specimens were tested, and the reported value represents the average compressive strength at 28 days of curing. The tests were conducted using a uniaxial compression testing machine with a capacity of 3000 kN.The same testing machine was also employed to determine the splitting tensile strength of cylindrical concrete specimens with dimensions of 100 mm in diameter and 200 mm in height, after 28 days of curing. The splitting tensile strength test was performed by applying a compressive load along the longitudinal axis of the cylinder until failure occurred. During testing, the cylinders were placed horizontally between the loading platens of the testing machine, and a continuous load was applied until the specimen fractured.

For each concrete mix, three cylindrical specimens were tested, and the reported splitting tensile strength values correspond to the average of the three results obtained under identical mix conditions

3.4.3. Microstructural analysis

Microstructural characterization of the concrete specimens was carried out using X ray Diffraction (XRD) and Energy Dispersive X ray Spectroscopy (EDX). XRD is a fundamental analytical technique for examining the mineralogical composition and hydration behavior of cement-based materials. It enables the identification of crystalline phases, which possess long range atomic order, as well as amorphous phases that lack such ordering. Owing to its capability to track phase evolution, XRD is widely used in concrete research to analyze cement, crushed concrete powder, hydrated cement paste, and supplementary cementitious materials such as pozzolans and nanomaterials.

In this study, RHA powder was first examined by XRD to validate its chemical composition and to confirm its predominantly amorphous silica structure, as suggested by complementary characterization methods. In addition, six powdered samples obtained from both the control and RHA modified concrete mixes were prepared by crushing the hardened concrete and sieving the resulting powder to pass a 75 µm sieve. These samples were subjected to XRD analysis to provide microstructural interpretation of the mechanical strength trends observed across different RHA replacement levels.

Elemental analysis was performed using EDX, which allows quantitative determination of elemental weight percentages within the concrete matrix. The EDX results served two essential purposes:Providing input data for the Monte Carlo and PhyX radiation shielding simulations described in Section 4. Evaluating compositional variations, particularly changes in the calcium to silicon (Ca/Si) ratio, which are known to influence hydration processes and the mechanical properties of cementitious systems.

3.4.4. Radiation shielding measurements

To assess the radiation shielding capabilities of the prepared concrete mixes, both simulation and computational approaches were employed. Monte Carlo simulations and Phy-X software were used to evaluate the radiation shielding performance against gamma and fast neutrons.

3.4.4.1. MC Simulation

In this work, the Monte Carlo method was used to simulate the movement of natural particles as well as to predict the gamma/neutron radiation performance., in the energy range of gamma rays (γp) at $0.015 \leq \gamma p \leq 15$ MeV. The goal is to determine and compare the intensity of γ-rays before and after passing through the samples under study. This code is used in the study of radiation shielding, as well as calculating radiation doses in addition to detector design [46]. The simulation code features operation across a wide range of energy levels, accommodating all different engineering designs and enabling rapid calculations. Several data lines must be available to create the input file for the code, which include the distance between the source and the detector, the dimensions of the source, the elemental composition, and the chemical composition of the samples under study. As shown in Figure 7, the geometric configuration for the simulation was created using a pre-set 3D setup. The data about the used code was detailed in the previous published work [47]. Also, the Phy-X/PSD (PhyX) was used to validate the MC results. It is an online tool for figuring out radiation doses and shielding characteristics [48-50].

The concrete shield consists of concrete cubes representing the control mix and the mixes containing increasing proportions of RHA, each with dimensions of 100 × 100 × 100 mm, where the shield thickness is 10 cm. This thickness is substituted into the Beer-Lambert equation as follows [51]:

$$\mu, \text{cm-1} = (1/T) \ln (C/C0) \quad (1)$$

where μ is the linear attenuation coefficient (cm^{-1}), T is the material thickness (cm), and C_0 and C are the initial and final counts of gamma-ray photons measured before and after shielding. Additionally, the values of other γ-ray attenuation parameters, such as the half-value thickness (HVT), tenth-value thickness (TVT), mean free path (MFP), effective atomic number (Zef), transfer factor (TF) and radiation protection (RPE) were calculated using the following equations. [51-53]:

$$HVT, cm = \ln(2) / \mu \quad (2)$$

$$TVT, cm = \ln(10) / \mu \quad (3)$$

$$MFP, cm = 1 / \mu \quad (4)$$

Each of these attenuation parameters provides unique insights into the shielding performance of concrete against γ-rays. The mass attenuation coefficient represents the attenuation per unit mass and is crucial for comparing materials with different densities, making it a fundamental parameter in material selection for radiation shielding. The HVT and TVT are the thickness of material required to reduce the gamma-ray intensity by half and tenth, offering a practical measure of the material's efficiency in attenuating radiation. While HVT is often used for quick evaluations, TVT is more critical for scenarios requiring higher attenuation, highlighting the complementary nature of these parameters in assessing and optimizing shielding performance.

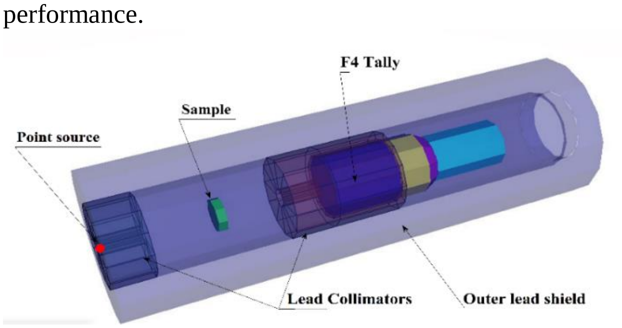

Figure 7. 3-D view of the radiation attenuation simulation system used for the prepared concrete samples

3.4.4.2. PhyX software

Phy-X is a web-based software tool designed for the assessment of radiation shielding parameters and radiation doses. It facilitates the determination of parameters including LAC, MAC, HVL, TVL, MFP, effective atomic number, and electronic density. These calculations are essential for the design of radiation protection materials used in X-ray and gamma-ray applications. The user-friendly interface allows input of the chemical composition of a given substance, enabling the computation of its properties across a broad spectrum of radiation energies and sources.

4. Experimental results

4.1. Physical properties results

4.1.1. Setting times and consistency results

Cement paste samples incorporating RHA exhibited higher standard consistency values compared with the control mix. This behavior can be attributed to several factors. First, the porous structure of RHA particles enables them to absorb and retain a considerable amount of water, thereby increasing the water demand required to achieve normal consistency during cement hydration.

Additionally, the chemical composition of the RHA used in this study (Table 6) contains a high proportion of silicon and aluminum oxides, accounting for 43.2% of the total mass and approximately 92.37% of the mineral fraction of the ash, excluding carbon content. Such a composition enhances the pozzolanic reactivity of RHA, which contributes to increased water consumption during the activation of hydration and pozzolanic reactions within the cementitious system.

Moreover, increasing the replacement ratio of cement with RHA further intensified this effect. The highest increase in standard consistency reached 35.7% at a replacement level of 25%, indicating a substantial rise in water demand as the RHA content increased.

Regarding the setting time of cement paste, a reduction in both initial and final setting times was observed for mixtures containing RHA up to a 15% replacement level. This trend supports the assumption that the RHA used in this study exhibits significant pozzolanic activity, which accelerates the early hydration reactions. Similar observations have been reported in several previous studies.[54-56], which attributed the reduction in initial and final setting times upon biochar addition to its filler effect and absorption of free water. The shortened setting time is attributed to biochar particles acting as filler and moisture absorbers. This effect is further influenced by the hydrophilic or hydrophobic nature of the biochar, which depends on its production temperature and contributes to micro-filling [57]. However, when the replacement ratio exceeded this threshold, an increase in setting times was observed. The recorded increases were slight, with the maximum increase in final setting time in the 25 RHA mix reaching 7.14% compared to the control mix. These results provide a preliminary indication that the optimal replacement ratios for the type of biochar powder used in the current study range from 10% to 15% of the cement weight. Figure 8 shows the values of setting times and consistency values of all designed mixes in this study.

4.1.2. Slump test result

The effect of using RHA powder as a partial cement replacement material on slump values was investigated. As shown in Figure 9, a significant decrease in slump values was observed. The porous microstructure and surface fineness of the RHA powder likely contributed to this reduction in slump, consequently affecting the workability of the resulting concrete. Biochar particles have been shown to retain higher amounts of free water within their porous structure [54]. Replacing 25% of the cement with RHA resulted in a 57.3% decrease in slump values compared to the control mix.

These findings align with previous research on other biochar types, which indicates that increasing the proportion of biochar in concrete mixes generally leads to decreased workability [58].

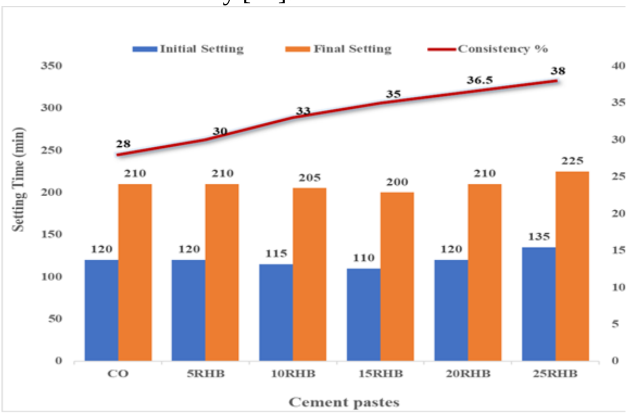

Figure 8. Setting times and consistency values of control and RHA cement pastes

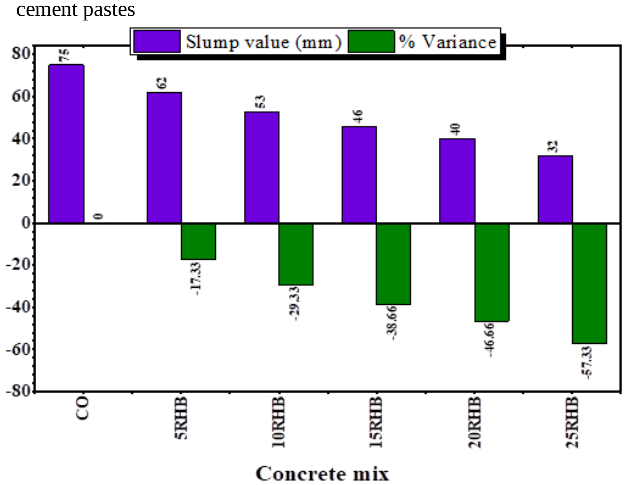

Figure 9. Slump values for control and RHA concrete mixes.

4.2. Mechanical properties results

4.2.1. Compressive strength results

The compressive strength results of the control and RHA modified concrete specimens, presented in Figure 10, demonstrate the potential of rice husk ash (RHA) to enhance the compressive strength of concrete. The improvement in mechanical performance can be attributed primarily to the chemical composition and moderate pozzolanic activity of RHA. This interaction promotes the formation of additional calcium silicate hydrate (C–S–H) gel, which is the main strength giving phase in cementitious systems.

Moreover, the fine particle size of RHA contributes to a filler effect, allowing the particles to occupy micro voids within the cement matrix. This process increases the overall density of the concrete and refines the pore structure by reducing pore size and connectivity. As a result, the microstructure becomes more compact, which enhances the mechanical performance of the concrete.

Among the mixtures containing RHA, the 10% replacement level of cement with RHA provided the most favorable result, producing a 13.74% increase in compressive strength compared with the control mixture. This optimal replacement ratio is consistent with the findings reported by Gomes et al., who also observed improved compressive strength at moderate RHA substitution levels. [59], who reported that incorporating 5% and 10% water treatment sludge biochar enhanced the compressive strength of natural sludge mortar by 37% and 46%, respectively. Other studies have also demonstrated optimal concrete performance at a 10% biochar replacement ratio, albeit with varying degrees of improvement [29, 30]. The biochar used in this study is characterized by a higher combined percentage of silicon and aluminum oxides (43.2%) compared to other biochar types previously incorporated into concrete. For example, rice husk ash used by Yang et al. (2021) [60] In contrast, the RHA used in the study by Gomes et al. contained only 16.51% of the key oxides responsible for enhancing pozzolanic reactions. This relatively low content of reactive silica and alumina, combined with the high porosity of the biochar particles, resulted in a 5.5% reduction in compressive strength at a 5% cement replacement level after 28 days of curing.

In the present study, however, even a 25% replacement ratio produced compressive strength values comparable to the control mix, underscoring the potential for incorporating relatively high amounts of this biochar into concrete without compromising mechanical performance. This finding highlights a promising avenue for developing more sustainable and environmentally friendly concrete.

The sustainability benefits arise from the fact that biochar acts as a stable carbon-rich material derived from organic feedstocks that would otherwise decompose or combust, releasing CO_2 into the atmosphere. When incorporated into concrete, the biochar's stable carbon structure remains locked within the matrix, enabling long-term carbon sequestration and significantly reducing the concrete's overall carbon footprint.

4.2.2. Tensile strength results

The highest splitting tensile strength of the concrete cylinders was achieved at a 15% replacement level of RHA, as shown in Figure 11. At this optimal dosage, the tensile strength exhibited a 9.48% increase compared with the control mix. Beyond the 15% replacement level, a marginal decline in tensile strength was observed; however, all RHA containing mixes continued to outperform the control sample. Notably, even the highest replacement ratio of 25% RHA maintained tensile strength values comparable to the control, with a slight improvement of approximately 1.83%. These results reinforce the feasibility of using RHA as a high volume cement replacement while preserving acceptable mechanical performance.

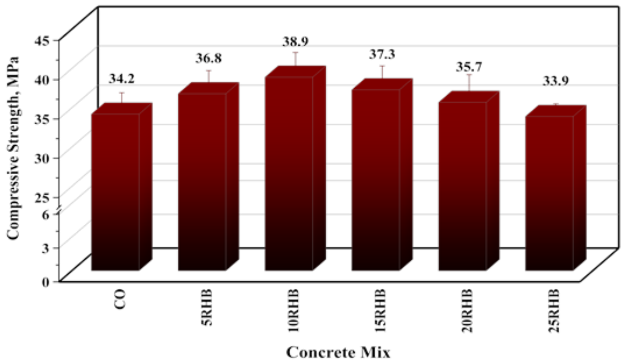

Figure 10. Compressive strength for control and RHA concrete specimens.

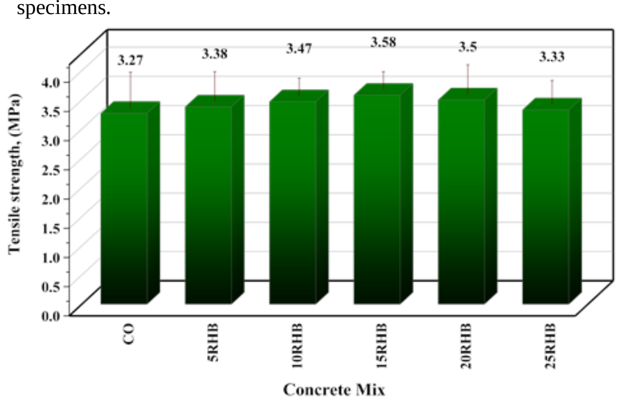

Figure 11. Tensile strength for control and RHA concrete specimens.

In addition to the mechanical advantages, the incorporation of RHA offers substantial environmental benefits, including reduced CO_2 emissions associated with cement manufacturing, diversion of agricultural waste from disposal, and enhanced sustainability of concrete materials.

The mechanical behavior observed in this study highlights a nuanced response of concrete to RHA incorporation. While the 10% replacement level yielded the highest compressive strength—likely due to moderate pozzolanic activity, increased C–S–H gel formation, and microstructural densification through the filler effect—the peak tensile strength at 15% RHA suggests that different mechanisms govern tensile resistance. At higher RHA contents, the distinctive characteristics of the biochar, such as its fibrous morphology and internal porosity, appear to contribute positively to tensile performance. These features may provide crack bridging capabilities, where fibrous RHA particles span developing microcracks under tensile loading, thereby delaying crack propagation. Additionally, the porous structure of RHA can facilitate stress redistribution, reducing local stress concentrations and enhancing the tensile load carrying capacity of the concrete matrix.

4.3. Microstructural analysis results

4.3.1. XRD analysis

X ray diffraction (XRD) is a fundamental technique for investigating the complex hydration processes of cementitious materials. By providing detailed information on mineralogical composition and phase evolution, XRD offers valuable insight into the mechanisms governing the development and performance of cement paste. In this study, XRD analysis was performed to investigate the composition and hydration products of cement pastes containing different proportions of rice husk ash (RHA).

Six cement paste samples were analyzed after 28 days of moisture curing, including the control mix (CO) and mixes containing 5%, 10%, 15%, 20%, and 25% RHA (5RHA, 10RHA, 15RHA, 20RHA, and 25RHA), as illustrated in Figure 12. The XRD patterns revealed the presence of calcium silicate hydrate (C–S–H, PDF#00 033 0306) and portlandite (CH, PDF#00 004 0733) as the primary hydration products in all samples, confirming their well established roles in cement hydration and strength development. In addition, minor peaks corresponding to ettringite (PDF#00 041 1451) and quartz (SiO_2 , PDF#01 083 0539) were detected.

Among these phases, C–S–H is the most critical compound governing the mechanical performance of concrete, as it forms directly during cement hydration and acts as the primary binding phase within the cement matrix. A higher content of C–S–H contributes to the formation of a denser and stronger interfacial transition zone (ITZ) between the cement paste and aggregates, thereby enhancing the overall mechanical properties of concrete, particularly its compressive strength.

The presence of portlandite (CH) plays a more complex role in concrete performance. At moderate levels, portlandite can contribute to reducing pore volume and may slightly enhance strength due to its crystalline structure. However, excessive or insufficient quantities of portlandite can adversely affect both strength and durability, as high CH content may increase vulnerability to chemical attack, while reduced CH availability may limit the progression of hydration reactions.

[61]. The presence of quartz (silica) particles helps in more densification of the concrete matrix and formation of CSH gel. It is also responsible for enhancing the ITZ

between the aggregate and cement paste matrix. Ettringite plays a complex role in concrete. While controlled formation can contribute to a denser microstructure and improved properties, excessive formation can have detrimental effects [62].

Figure 12 demonstrates an increase in CSH peak intensity in RHA samples compared to the control mix, with the most pronounced peaks observed at 10% and 15% RHA incorporation. This increase coincides with a slight reduction in portlandite peaks, suggesting moderate pozzolanic activity of the RHA. The significant increase in CSH intensity observed in the 10% and 15% RHA pastes compared to the control highlights the influence of RHA on the hydration process. RHA's porous structure and functional groups can interact with cement components, potentially influencing hydration kinetics and the formation of hydration products. The high silicon and aluminum oxide content (approximately 43%) of the biochar used in this study suggests moderate pozzolanic potential. Furthermore, RHA incorporation can enhance concrete durability by reducing permeability, improving chloride ion resistance, and refining the overall microstructure, as reported in the literature [63]. XRD analysis provided further insights into the mineralogical transformations within the concrete matrix. While ettringite peaks were evident in both control and RHA samples, a slight reduction in their intensity was observed in the RHA samples, likely attributed to the consumption of calcium ions by pozzolanic reactions between the RHA and the cement. Conversely, the presence of quartz peaks, originating from the silica content within the RHA, was evident and their intensities generally increased with increasing RHA percentages.

This observation, coupled with the enhanced CSH formation and the observed reduction in portlandite, indicates that the incorporation of RHA significantly alters the mineralogical composition of the concrete matrix. These findings provide valuable insights into the mechanisms underlying the observed improvements in the mechanical properties of the RHA-modified concrete.

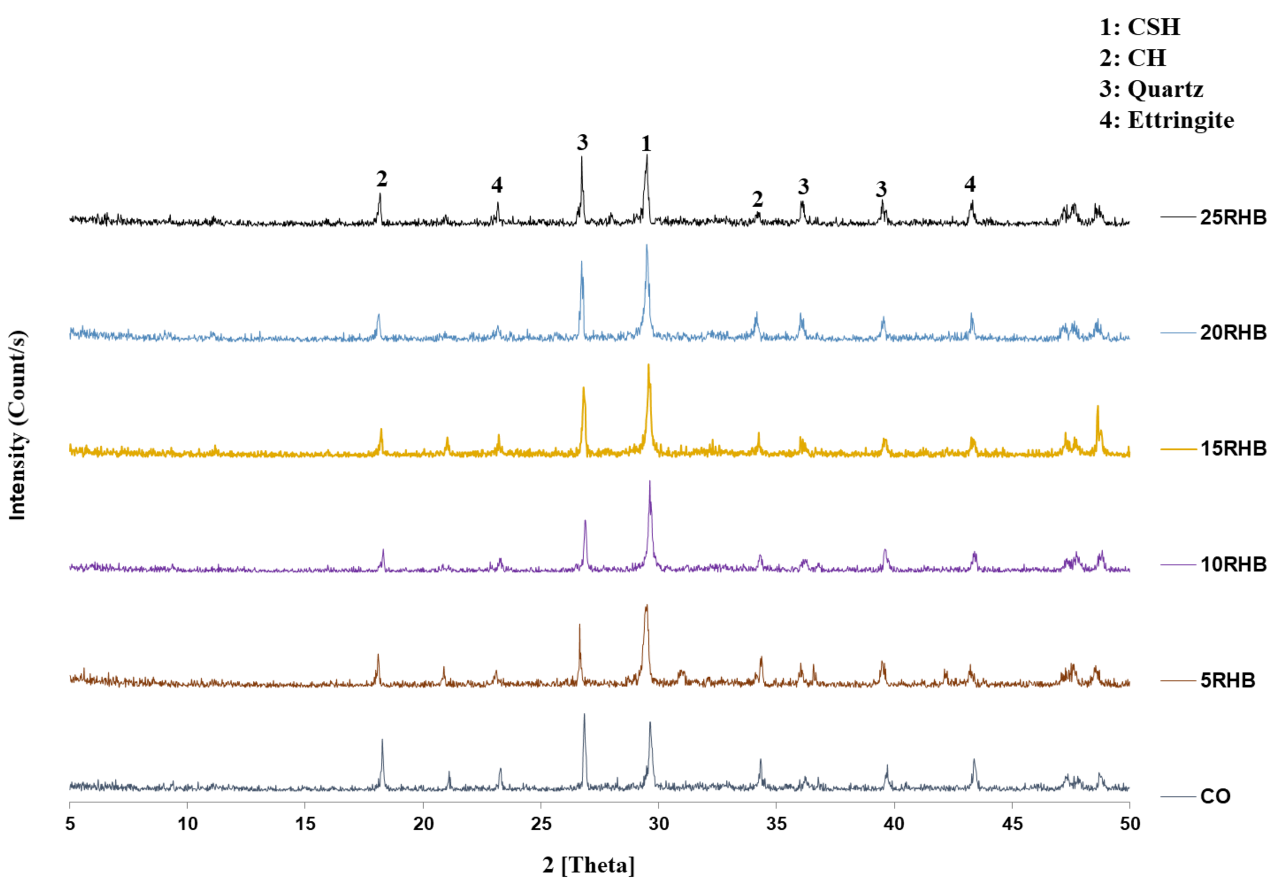

Figure 12. XRD patterns of the control and RHA mixes.

4.3.2. EDX analysis results

As previously discussed, energy dispersive X ray spectroscopy (EDX) was employed to chemically characterize the concrete samples and determine the elemental weight percentages of their constituents. This analysis enabled a comparative evaluation of the elemental composition of the different mixtures. The obtained results served two main purposes. First, they provided the necessary input data for developing radiation shielding simulation models using Monte Carlo (MC) codes and the Phy X software, as described in Section 5. Second, they were used to interpret variations in mechanical strength by examining key compositional parameters, particularly the Ca/Si ratio.

An increase in carbon content was observed in concrete mixtures with higher RHA replacement levels. This increase can be attributed to the fact that more than 52% of the RHA composition consisted of carbon, which was volatilized during the XRF analysis used to determine the chemical composition of RHA.

The Ca/Si ratio was identified as a critical parameter influencing the strength development of the concrete mixtures. Adjusting this ratio through the appropriate selection and proportioning of cementitious materials and admixtures allows the properties of concrete to be optimized for specific performance requirements, thereby improving both structural efficiency and durability.

A clear trend was observed in which a reduction in the Ca/Si ratio corresponded to increased polymerization of the C–S–H gel, resulting in enhanced compressive strength. Within the hardened cement matrix, the Ca/Si ratio of the C–S–H phase serves as an indicator of the degree of polymerization of hydration products. Lower Ca/Si ratios generally indicate a higher degree of polymerization, reflecting the formation of longer and more interconnected C–S–H chains, which contribute to improved mechanical performance. These findings are consistent with the results reported by Kim (2013).[63], a reduction in the Ca/Si ratio within the C-S-H phase is associated with C-S-H chain elongation and increased polymerization. In agreement with Choudhary et al. (2021) [64] and Dadsetan and Bai (2017) [65], a strong correlation was observed between compressive strength and the Ca/Si ratio: a decrease in the Ca/Si ratio corresponded to an increase in compressive strength. These findings emphasize the critical role of C-S-H polymerization in enhancing concrete's mechanical properties. Several literature studies [66, 67] also demonstrated a clear inverse relationship between the Ca/Si ratio and concrete compressive strength. Figure 13 presents EDX patterns of the primary elements that constitute the hydration products in different concrete specimens, which include O, Ca and Si peaks as detailed by (wt.%) in Table 8. Notably, Figure 13 also includes C peak, enabling a comparative analysis of carbon levels between RHA samples and the control. Figure 13 illustrates the comparison between EDX spectra for concrete specimens. Table 8 provides the EDX results for the different mixes and shows the Ca/Si ratio, which is an indicator for C-S-H in concrete which plays an important role in strength development of concrete as previously mentioned. The results show that the Ca/Si ratios of 5.95, 5.69, 4.84, 4.89, 5.11, and 5.6 for CO, 5RHA, 10RHA, 15RHA, 20RHA, and 25RHA, respectively. From the results, it can be concluded that the order in Ca/Si ratio is CO > 5RHA > 25RHA > 20RHA > 15RHA > 10RHA. EDX analysis revealed a correlation between Ca/Si ratio and mechanical properties, with lower Ca/Si ratios generally resulting in higher compressive strengths. While the order of Ca/Si ratios did not perfectly align with the order of compressive strengths, the correlation was strong. Notably, the 10% RHA sample, exhibiting the lowest Ca/Si ratio, demonstrated the highest compressive strength, supporting the observed trend.

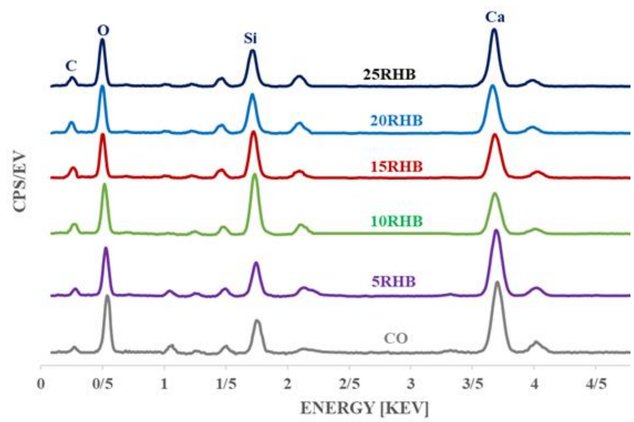

Figure 3. Decomposition of $M_b^{\infty}(t)$

Table 8.
EDX results for different concrete mixes.

Element	Composition (wt.%)					
	CO	5RH	10RH	15RH	20RH	25RH
O K	38.1	39.01	40.9	41.11	39.85	38.46
Ca K	41.3	38.92	34.99	35.11	35.91	37.25
Si K	6.95	6.84	7.23	7.18	7.03	6.65
Al K	1.46	1.47	1.72	1.46	1.31	1.22
Fe K	1.68	1.53	1.63	1.46	1.25	1.23
Mg K	0.33	0.29	0.31	0.33	0.3	0.25
Na K	1.97	1.66	1.79	1.37	1.15	1.17
C K	8.11	10.27	11.43	11.97	13.19	13.75
Density	2.45	2.52	2.57	2.6	2.58	2.55
Ca/Si	5.95	5.69	4.84	4.89	5.11	5.6

5. Radiation shielding performance

5.1. Gamma attenuation

The LAC by MCNP and Phy-X in the photon energy (γp) range of 0.015–15 MeV is shown in Table 9. With a maximum Δ of 2.814%, the values of simulated LAC were in decent agreement with the values determined by Phy-X. The LAC value of the X-RHA concrete samples under investigation decreases as the γ-energy rises. For X-RHA concrete samples, the simulated LAC values decline as follows: 38.657 to 0.057 cm-1 for CO sample, 35.675 to 0.058 cm-1 for 5RHA sample, 33.815 to 0.058 cm-1 for 10RHA sample, 33.960 to 0.058 cm-1 for 15RHA sample, 33.625 to 0.058 cm-1 for 20RHA sample, and 33.390 to 0.057 cm-1 25RHA sample at γp range from 0.015 to 15 MeV. Figure 14(a) shows an abrupt decrease in LAC for each of the X-RHA concrete samples under study because of the PEE interaction, which has changed the cross-section (σp) with γ -3: 5 [68-70]. We observe that when the values of γp energy increase from 0.015 to 0.2 MeV, σp decreases significantly, and the PEE interaction consequently decreases. For X-RHA concrete samples, there is a strong tendency to decrease from 38.657 to 0.311 cm-1 for CO sample, 35.675 to 0.319 cm-1 for 5RHA sample, 33.815 to 0.324 cm-1 for 10RHA sample, 33.960 to 0.328 cm-1 for 15RHA sample, 33.625 to 0.325 cm-1 for 20RHA sample, and 33.390 to 0.322 cm-1 for 25RHA sample.The expected LAC in the γp range from 0.300 to 15 MeV decreases exponentially when γp from 0.300 to 15 MeV is increased, as shown in Figures 14(b,c). The CM interaction and the σp changes brought on by γp-1 are responsible for the exponential decline [71]. This effect can be explained by the fact that because of its increased speed, a larger γp has a lower tendency to interact with the atoms of the material. Consequently, the probability of γp interaction decreases, and the likelihood of γp scattering increases as the energy level rises. A smooth decline in LAC values followed a gradual decrease in σp with fewer electron-γp interactions, which was linked to an increase in γp values. So, the LAC values gradually decrease from 0.262 to 0.57 cm-1 for the CO sample, 0.269 to 0.058 cm-1 for the 5RHA sample, 0.274 to 0.058 cm-1 for the 10RHA sample, 0.278 to 0.058 cm-1 for 15RHA sample, 0.276 to 0.058 cm-1 for 20RHA sample, and 0.273 to 0.057 cm-1 for 25RHA sample. We noted that the 15RHA sample has the highest LAC because of its high density, On the contrary, the 25RHA sample is a less valuable sample. The LAC for the mixed concrete samples and previously published doped concrete samples are compared in Figure 15. The samples of this study achieved results equal to those of the previously studied and published samples at 10 MeV, 0.5 MeV, and 5 MeV. It presents a comparison of the UHPC samples with commercial concrete (mixes of PbO bulk powder with cement, with substitution ratios ranging from 1 to 5% %. Additionally, five other mixtures of GD bulk powder with cement increased the substitution rates to 9% and one hybrid mix combining 5% PbO and 7% GD [52]), Bashtar concretes (S-magnetite, S-scrap, ilmenite, H-serpentine, I-limonite, and B-magnetite [72]), and marble (MD) and granite (GD) waste dust of cement at a replacement ratio of 6%. Furthermore, two additional mixes with the cement weight of nano-alumina (NAl) [51]. The prepared concrete mix containing 15%BPA (15RHA) were higher than those compared (Bashtar concretes, 1BL, NA1, and (1-5) BG) at 0.5 and 10 MeV. Also, it higher than 1BL, 2BL, 1-9BG, MD6%, GD6%, NA1, and GD6%+NA1) at 5 MeV.

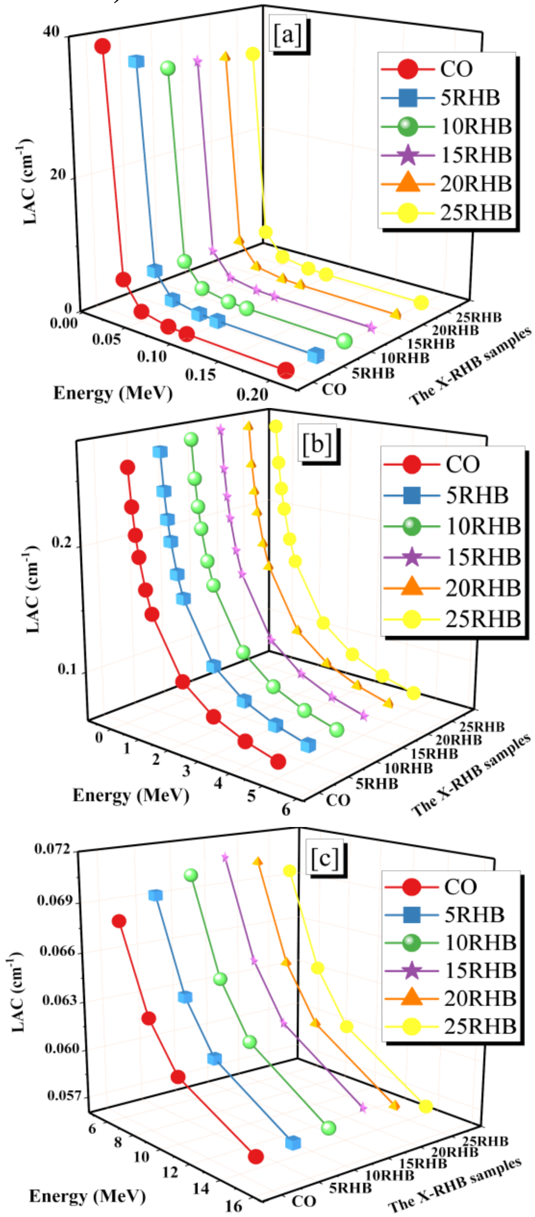

Figure 15. The linear attenuation (a) in the PEE region, (b and c) in the Compton region for the X-RHA concrete samples.

Table 9.
The linear attenuation (LAC), obtained using MCNP code and PhyX software for the prepared X-RHA Concrete samples.

Energy, (MeV)	The linear attenuation (LAC, cm^{-1})								
	CO			5RHA			10RHA		
	PhyX	MC	φ. (%)	PhyX	MC	φ. (%)	PhyX	MC	φ. (%)
0.015	38.745	38.657	0.225	35.754	35.675	0.222	33.887	33.815	0.213
0.03	5.467	5.445	0.408	5.080	5.060	0.404	4.840	4.822	0.388
0.05	1.512	1.492	1.339	1.437	1.418	1.326	1.391	1.373	1.273
0.08	0.653	0.636	2.655	0.643	0.626	2.629	0.637	0.621	2.526
0.1	0.505	0.490	2.814	0.504	0.490	2.787	0.505	0.491	2.677
0.2	0.319	0.311	2.444	0.326	0.319	2.420	0.331	0.324	2.325
0.3	0.267	0.262	1.712	0.274	0.269	1.695	0.279	0.274	1.628
0.4	0.236	0.233	1.289	0.243	0.240	1.277	0.247	0.244	1.226
0.5	0.215	0.212	1.059	0.221	0.218	1.049	0.225	0.223	1.007
0.6	0.198	0.196	0.958	0.204	0.202	0.948	0.208	0.206	0.910
0.8	0.174	0.172	0.725	0.179	0.177	0.717	0.182	0.181	0.689
1	0.156	0.155	0.694	0.160	0.159	0.688	0.163	0.162	0.660
2	0.110	0.109	0.580	0.113	0.112	0.574	0.115	0.114	0.551
3	0.090	0.090	0.482	0.092	0.092	0.477	0.094	0.094	0.458
4	0.079	0.079	0.304	0.081	0.081	0.301	0.082	0.082	0.289
5	0.073	0.072	0.279	0.074	0.074	0.277	0.075	0.075	0.266
6	0.068	0.068	0.255	0.069	0.069	0.252	0.070	0.070	0.242
8	0.063	0.063	0.225	0.064	0.064	0.223	0.064	0.064	0.214
10	0.060	0.060	0.295	0.061	0.061	0.292	0.061	0.061	0.281
15	0.058	0.057	0.092	0.058	0.058	0.092	0.058	0.058	0.088

Energy, (MeV)	The linear attenuation (LAC, cm^{-1})								
	CO			5RHA			10RHA		
	PhyX	MC	φ. (%)	PhyX	MC	φ. (%)	PhyX	MC	φ. (%)
0.015	38.745	38.657	0.225	35.754	35.675	0.222	33.887	33.815	0.213
0.03	5.467	5.445	0.408	5.080	5.060	0.404	4.840	4.822	0.388
0.05	1.512	1.492	1.339	1.437	1.418	1.326	1.391	1.373	1.273
0.08	0.653	0.636	2.655	0.643	0.626	2.629	0.637	0.621	2.526
0.1	0.505	0.490	2.814	0.504	0.490	2.787	0.505	0.491	2.677
0.2	0.319	0.311	2.444	0.326	0.319	2.420	0.331	0.324	2.325
0.3	0.267	0.262	1.712	0.274	0.269	1.695	0.279	0.274	1.628
0.4	0.236	0.233	1.289	0.243	0.240	1.277	0.247	0.244	1.226
0.5	0.215	0.212	1.059	0.221	0.218	1.049	0.225	0.223	1.007
0.6	0.198	0.196	0.958	0.204	0.202	0.948	0.208	0.206	0.910
0.8	0.174	0.172	0.725	0.179	0.177	0.717	0.182	0.181	0.689
1	0.156	0.155	0.694	0.160	0.159	0.688	0.163	0.162	0.660
2	0.110	0.109	0.580	0.113	0.112	0.574	0.115	0.114	0.551
3	0.090	0.090	0.482	0.092	0.092	0.477	0.094	0.094	0.458
4	0.079	0.079	0.304	0.081	0.081	0.301	0.082	0.082	0.289
5	0.073	0.072	0.279	0.074	0.074	0.277	0.075	0.075	0.266
6	0.068	0.068	0.255	0.069	0.069	0.252	0.070	0.070	0.242
8	0.063	0.063	0.225	0.064	0.064	0.223	0.064	0.064	0.214
10	0.060	0.060	0.295	0.061	0.061	0.292	0.061	0.061	0.281
15	0.058	0.057	0.092	0.058	0.058	0.092	0.058	0.058	0.088

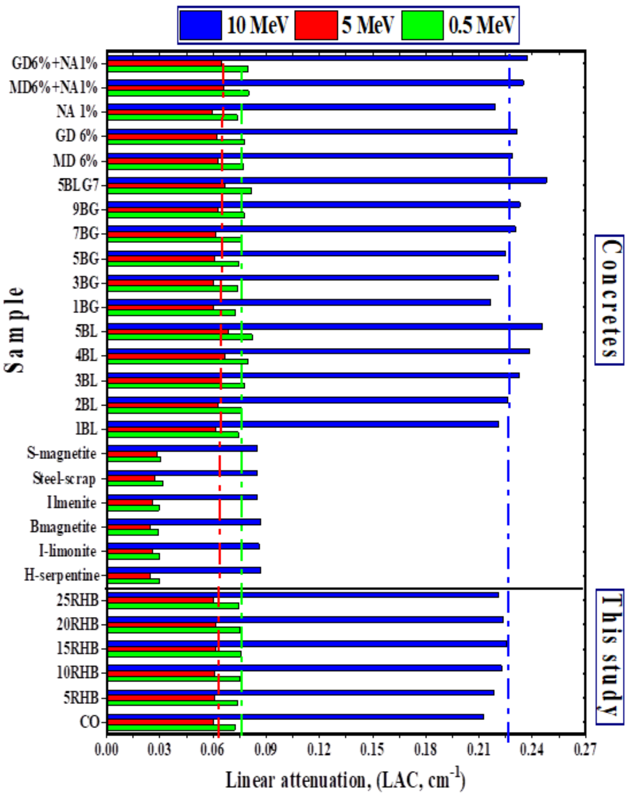

Figure 15. Comparison between the LAC for the mixed concrete samples with two previously published doped concrete samples.

The effectiveness of gamma ray shielding materials is commonly evaluated using three key parameters: the half value thickness (HVT), the tenth value thickness (TVT), and the mean free path (MFP). These parameters collectively describe both the required material thickness and the radiation attenuation capability. For a given photon energy, lower HVT, TVT, or MFP values indicate superior radiation shielding performance, as radiation is attenuated over a shorter distance.

The HVT and TVT values exhibit an inverse relationship with the linear attenuation coefficient (LAC). As the LAC decreases, both HVT and TVT increase. Over the photon energy range of 0.015–15 MeV, the HVT values increased from 0.018 to 12.061 cm for the CO sample, 0.019 to 12.036 cm for 5RHA, 0.020 to 11.991 cm for 10RHA, 0.020 to 11.870 cm for 15RHA, 0.021 to 11.974 cm for 20RHA, and 0.021 to 12.106 cm for 25RHA. As shown in Figure 16(a), the 15RHA sample exhibited the lowest HVT values due to its highest LAC, whereas the 25RHA sample displayed the highest HVT values, corresponding to its lower LAC.

A similar trend was observed for the TVT values, as illustrated in Figure 16(b). The TVT increased from 0.060 to 40.066 cm for the CO mix, 0.065 to 39.984 cm for 5RHA, 0.068 to 39.432 cm for 10RHA, 0.068 to 39.778 cm for 15RHA, 0.068 to 39.778 cm for 20RHA, and reached its highest values for the 25RHA mix. Consistent with HVT behavior, the 25RHA sample exhibited the highest TVT values due to its low LAC, while the 15RHA sample showed the lowest TVT values, confirming its superior gamma ray attenuation capability.

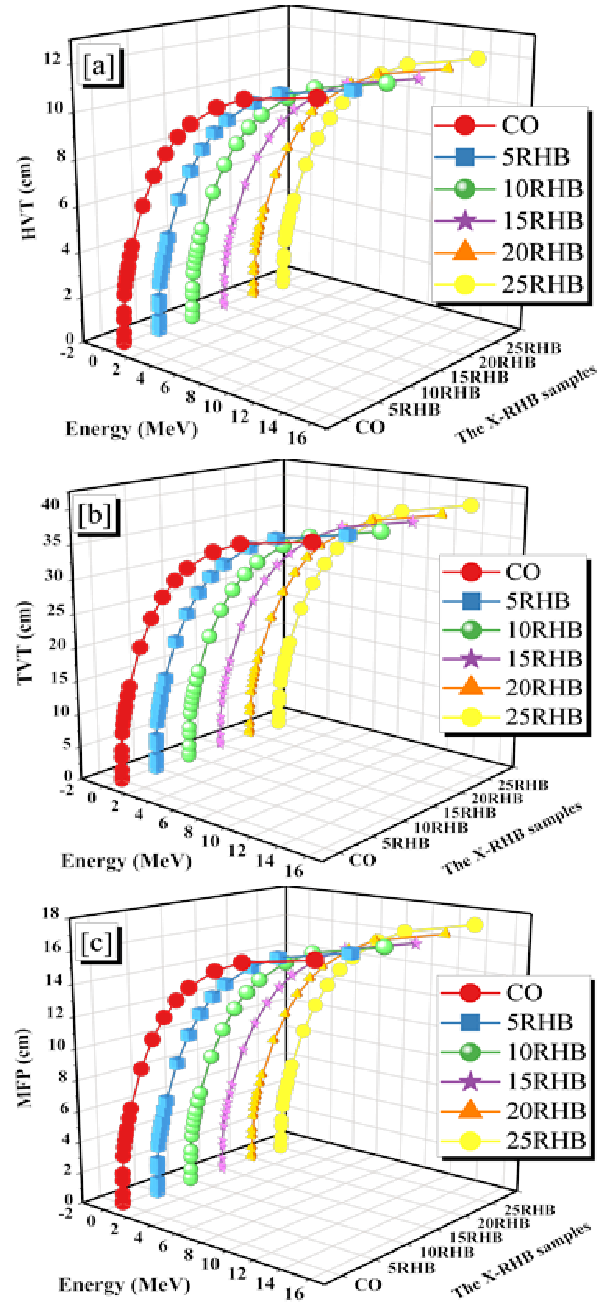

Figure 16. displays the concrete samples' HVT, TVT, and MFP in relation to γ-energy.

The mean free path (MFP) provides additional insight into how effectively a material absorbs or scatters gamma radiation. A lower MFP indicates a higher probability of photon interaction within a shorter distance, reflecting improved shielding efficiency. Consequently, evaluating the MFP is critical when selecting and designing materials for radiation shielding applications in nuclear, medical, and industrial environments, where effective protection of personnel and equipment is essential. [73]. From 0.026 to 17.400 cm for CO, from 0.028 to 17.365 cm for 5RHA, from 0.030 to 17.300 cm for 10RHA, from 0.029 to 17.125 cm for 15RHA, from 0.030 to 17.275 cm for 20RHA, and from 0.030 to 17.466 cm for 25RHA, the MFP values for the X-RHA concrete samples increase as γp energies increase from 0.015 to 15 MeV. MFP values are lowest in the 15RHA sample and highest in the 25RHA sample as shown in Figure 16(c) and that is due to the inverse relationship between MFP and LAC [74].

For the X-RHA concrete samples, Figure 17 displays graphs of the adequate atomic number versus γ-energy ranging from 0.015 to 15 MeV. A higher Zef value indicates a greater interaction with radiation through mechanisms like PEE/Compton interactions. Materials with a higher Zef value may be better for protecting against high-energy [75]. As the γp rises for the materials under study, the Zef values fall. The concrete's Zef ranged from 18.407 to 12.525 for CO, 18.078 to 11.751 for 5RHA, 17.833 to 11.358 for 10RHA, 17.806 to 11.298 for 15RHA, 17.806 to 11.241 for 20RHA, and 17.821 to 11.251 for 25RHA concrete sample, depending on the energy spectra specified in this study. Given this, it is feasible to conclude that the radiation shielding efficiency of materials varies with the radiation energy; that is, certain substances may be more effective at higher or lower energies than others. Due to its content of elements with a high atomic number and its high density compared to the other samples in this study, the 15RHA sample had the highest value of Zef.

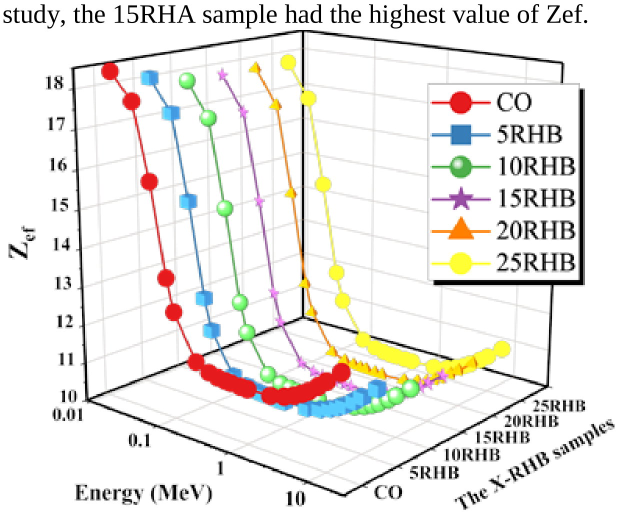

Figure 17. The Zef for the concrete samples as a function of photon energy.

5.2. Neutron attenuation

The radiation scattering ability of biochar has been explored in a limited number of studies [76, 77], Previous studies have reported that incorporating biochar into concrete can significantly enhance neutron shielding performance, particularly as the biochar content increases. This improvement is primarily due to the high carbon content of biochar. Carbon interacts strongly with neutrons through elastic scattering mechanisms, and these interactions depend on factors such as neutron energy, carbon isotope composition, and scattering angle. As a result, carbon rich composites often exhibit superior neutron attenuation compared with their γ radiation shielding performance. Carbon's neutron scattering characteristics make it an essential element for radiation protection materials used in nuclear reactors, shielding systems, and neutron related experimental research. Despite these promising findings, further studies are still required to fully understand the neutron shielding mechanisms in biochar based concretes.

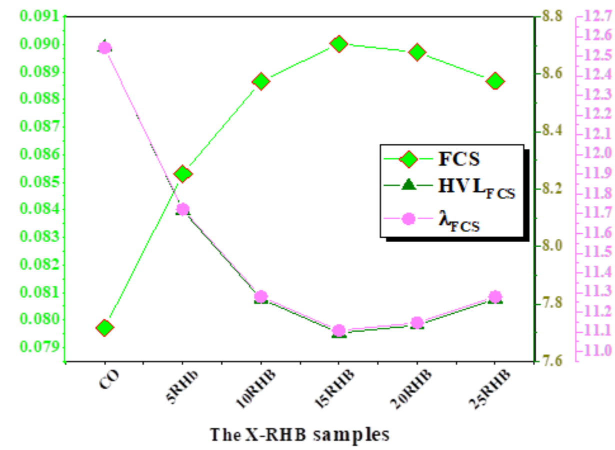

(a)

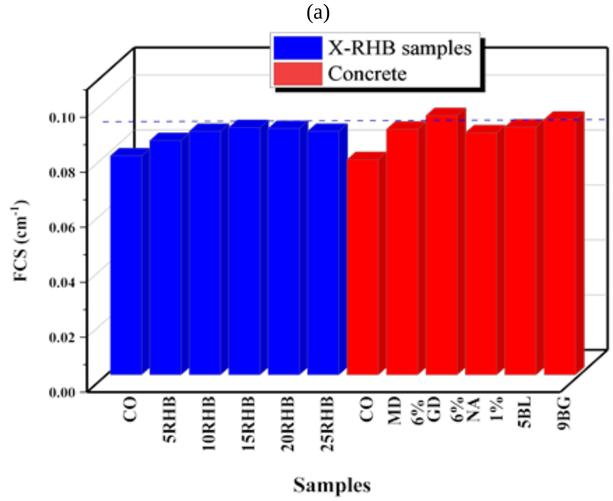

(b)

Figure 18. (a) The mixed concrete's fast neutron removal cross-section (FCS), half value layer (HVLFCS), and relaxation length (λFCS); (b) Comparison of the fast neutron removal cross-section (FCS) for the prepared X-RHA samples and previously published glass and concrete samples.

In this study, the fast neutron removal cross section (FCS), half value layer based on FCS (HVLFCS), and mean free path based on FCS (λFCS) for the RHA modified concrete samples are presented in Figure 18(a). Among all mixtures, the 15RHA sample demonstrated the highest FCS value of 0.090 cm^{-1}, along with the lowest HVLFCS (7.699 cm) and lowest λFCS (11.107 cm). These results indicate that the 15RHA mixture exhibits the strongest neutron shielding capability. This enhanced performance can be attributed to its relatively higher density and increased concentration of light elements, particularly carbon and oxygen, which are highly effective in moderating and scattering fast neutrons.

Figure 18(b) provides a comparative assessment between the concrete samples tested in this study and previously published concrete composites, further highlighting the competitive neutron shielding performance of the RHA based formulations.

[51, 52, 72] . From this comparison, it is clear that the RHA samples were higher than most of the compared concretes. The 15RHA sample was found higher than those compared except GD6% and 9BG samples.

6. Conclusions and future studies

This study examined the use rice husk ash, RHA as a partial cement replacement in concrete at substitution levels up to 25%. The biochar employed—distinguished by its unique chemical composition—represents an environmentally sustainable alternative to traditional cement. By reducing cement consumption, which is responsible for high energy demand and significant CO_2 emissions, RHA serves as a carbon sequestration medium. Its stable structure effectively immobilizes carbon within the matrix, contributing to greenhouse gas mitigation. Formulated with high proportions of silicon and aluminum oxides to promote pozzolanic activity, the material enhanced the concrete's physical, mechanical, and microstructural performance. In addition, the influence of different RHA replacement levels on radiation shielding capability was assessed using simulation codes for both γ ray and neutron radiation.

1- The incorporation of rice husk ash (RHA) had only a marginal influence on the setting times of the concrete mixes. Final setting time decreased slightly—by 4.76% relative to the control—at replacement levels up to 15%. However, beyond this threshold, a minor increase in final setting time was observed, reaching a maximum rise of 7.14% compared with the control mix at a 25% replacement level.

2- The incorporation of RHA had a more pronounced impact on standard consistency. As the RHA replacement level increased, the water demand required to achieve standard consistency also rose steadily, reaching a maximum increase of 35.7% at the 25% replacement level compared with the control mix. This increase in water demand is attributed to the porous structure of the biochar, which elevates its water absorption capacity, as well as its high specific surface area, which necessitates additional water to adequately wet the particles and achieve the required workability.

3. Consistent with the increased water demand required for standard consistency, the workability of concrete mixes containing RHA exhibited a progressive decline, as reflected by reduced slump values. The maximum slump reduction—57.3%—occurred at the 25% replacement level, underscoring the need for plasticizers when incorporating biochar into concrete to maintain adequate workability.

4. Optimal cement replacement with RHA powder resulted in moderate enhancements in both compressive and tensile strength. The optimum replacement levels were identified as 10% for compressive strength and 15% for tensile strength, yielding improvements of 13.74% and 9.48%, respectively. These strength gains stem from the favorable chemical composition and pozzolanic reactivity of RHA, wherein its interaction with calcium hydroxide leads to the formation of additional C–S–H gel, thereby increasing bond strength. Additionally, the fine RHA particles contribute to a denser cement matrix by filling micro voids and refining pore structure, which collectively enhance the overall mechanical performance of the concrete.

5. X ray diffraction (XRD) analysis revealed a reduction in portlandite formation and an increase in C–S–H at the 10% and 15% replacement levels, indicating improved hydration behavior and enhanced pozzolanic activity relative to the control sample.

6. Energy dispersive X ray (EDX) analysis demonstrated a strong correlation between the Ca/Si ratio and compressive strength. In general, lower Ca/Si ratios corresponded to higher compressive strength, although the relationship was not strictly linear. The 10% RHA sample, which exhibited the lowest Ca/Si ratio, achieved the highest compressive strength, further supporting this trend.

7. Gamma ray attenuation testing indicated a modest improvement in the shielding performance of the concrete. The 15RHA sample exhibited a higher linear attenuation coefficient than the other mixes, primarily due to its increased density. Conversely, the 25RHA sample demonstrated inferior shielding performance.

8. The 15RHA sample recorded the highest fast neutron removal cross section (0.090 cm^{-1}) and the lowest values for HVLFCS (7.699 cm) and λFCS (11.107 cm), confirming its effectiveness and suitability as a neutron shielding material.

The 15RHA sample exhibited the highest fast neutron removal cross-section (0.090 cm^{-1}) and the lowest HVLFCS (7.699 cm) and λFCS (11.107 cm), confirming its effectiveness and suitability as a neutron-shielding material. Based on these findings, the biochar employed in this study—characterized by its distinctive chemical composition—demonstrated strong potential as an eco-friendly cement replacement material, aligning well with sustainability objectives. This suitability arises from its capacity to reduce cement consumption, lower CO_2 emissions, and function as a medium for carbon sequestration.

Building upon the outcomes of this study, several promising avenues for future research can be pursued to further expand the application of this RHA. These include evaluating its influence on the structural performance of various concrete elements, such as beams, slabs, and columns. Additionally, the behavior of biochar-modified concrete under extreme environmental conditions, including elevated temperatures and chemical exposure, warrants detailed investigation, alongside comprehensive long-term durability assessments. Finally, exploring the use of this RHA in other concrete systems—such as high-strength concrete, ultra-high-performance concrete, lightweight concrete, and heavyweight concrete—represents a valuable direction for future study.

References

[1] Akhtar, A., & Sarmah, A. K. (2018). Novel biochar-concrete composites: Manufacturing, characterization and evaluation of the mechanical properties. Science of the Total Environment, 616, 408-416. https://doi.org/10.1016/j.scitotenv.2017.10.319

[2] Zhang, Z., & Wang, B. (2016). Research on the life-cycle CO2 emission of China's construction sector. Energy and Buildings, 112, 244-255. https://doi.org/10.1016/j.enbuild.2015.12.026

[3] Senadheera, S. S., Gupta, S., Kua, H. W., Hou, D., Kim, S., Tsang, D. C. W., & Ok, Y. S. (2023). Application of biochar in concrete – A review. Cement and Concrete Composites, 143, 105204. https://doi.org/10.1016/j.cemconcomp.2023.105204

[4] Ataeifar, A., et al. (2025). Mechanical performance and freeze–thaw durability of expansive clay stabilized with graphene oxide and fly ash: A laboratory study.

[5] Yaashikaa, P. R., Kumar, P. S., Varjani, S., & Saravanan, A. (2020). A critical review on the biochar production techniques, characterization, stability and applications for circular bioeconomy. Biotechnology Reports, 28, e00570. https://doi.org/10.1016/j.btre.2020.e00570

[6] Shaheen, S. M., Niazi, N. K., Hassan, N. E. E., Bibi, I., Wang, H., Tsang, D. C. W., ... & Rinklebe, J. (2019). Wood-based biochar for the removal of potentially toxic elements in water and wastewater: a critical review. International Materials Reviews, 64(4), 216-247. https://doi.org/10.1080/09506608.2018.1473096

[7] Oladele, S. O., Adeyemo, A. J., & Awodun, M. A. (2019). Influence of rice husk biochar and inorganic fertilizer on soil nutrients availability and rain-fed rice yield in two contrasting soils. Geoderma, 336, 1-11. https://doi.org/10.1016/j.geoderma.2018.08.025

[8] Wakudkar, H., & Jain, S. (2022). A holistic overview on corn cob biochar: A mini-review. Waste Management & Research, 40(8), 1143-1155. https://doi.org/10.1177/0734242X211069741

[9] Odega, C. A., Ayodele, O. O., Ogutuga, S. O., Anguruwa, G. T., Adekunle, A. E., & Falconede, C. O. (2023). Potential application and regeneration of bamboo biochar for wastewater treatment: A review. Advances in Bamboo Science, 2, 100012. https://doi.org/10.1016/j.bamboo.2023.100012

[10] Ajien, A., Idris, J., Md Sofwan, N., Husen, R., & Seli, H. (2023). Coconut shell and husk biochar: A review of production and activation technology, economic, financial aspect and application. Waste Management & Research, 41(1), 37-51. https://doi.org/10.1177/0734242X221127167

[11] Maljaee, H., Madadi, R., Paiva, H., Tarelho, L., & Ferreira, V. M. (2021). Incorporation of biochar in cementitious materials: A roadmap of biochar selection. Construction and Building Materials, 283, 122757. https://doi.org/10.1016/j.conbuildmat.2021.122757

[12] Barbhuiya, S., Das, B. B., & Kanavaris, F. (2024). Biochar-concrete: A comprehensive review of properties, production and sustainability. Case Studies in Construction Materials, 20, e02859.

[13] Sun, Y., Gao, B., Yao, Y., Fang, J., Zhang, M., Zhou, Y., ... & Yang, L. (2014). Effects of feedstock type, production method, and pyrolysis temperature on biochar and hydrochar properties. Chemical Engineering Journal, 240, 574-578. https://doi.org/10.1016/j.cej.2013.10.081

[14] Alizadeh, A. (2017). A review of the effect of the behavior of core diameter varying H/D ratio on concrete core strength. Journal of Civil Engineering Researchers, 1(5), 42-45.

[15] Mansourghanaei, M., & Biklaryan, M. (2022). Experimental study of compressive strength, permeability and impact testing in geopolymer concrete based on blast furnace slag. Journal of Civil Engineering Researchers, 4(3), 31-39. https://doi.org/10.52547/JCER.4.3.31

[16] Mansourghanaei, M., & Biklaryan, M. (2022). Experimental evaluation of compressive, tensile strength and impact test in blast furnace slag based geopolymer concrete, under high temperature. Journal of Civil Engineering Researchers, 4(2), 12-21.

[17] Muthukrishnan, S., Gupta, S., & Kua, H. W. (2019). Application of rice husk biochar and thermally treated low silica rice husk ash to improve physical properties of cement mortar. Theoretical and Applied Fracture Mechanics, 104, 102376. https://doi.org/10.1016/j.tafmec.2019.102376

[18] Javed, M. H., Sikandar, M. A., Ahmad, W., Bashir, M. T., Alrowais, R., & Wadud, M. B. (2022). Effect of various biochars on physical, mechanical, and microstructural characteristics of cement pastes and mortars. Journal of Building Engineering, 57, 104850. https://doi.org/10.1016/j.jobe.2022.104850

[19] Gupta, S., Kua, H. W., & Pang, S. D. (2020). Effect of biochar on mechanical and permeability properties of concrete exposed to elevated temperature. Construction and Building Materials, 234, 117338. https://doi.org/10.1016/j.conbuildmat.2019.117338

[20] Ahmad, M. R., Chen, B., & Duan, H. (2020). Improvement effect of pyrolyzed agro-food biochar on the properties of magnesium phosphate cement. Science of the Total Environment, 718, 137422. https://doi.org/10.1016/j.scitotenv.2020.137422

[21] Qin, Y., Pang, X., Tan, K., & Bao, T. (2021). Evaluation of pervious concrete performance with pulverized biochar as cement replacement. Cement and Concrete Composites, 119, 104022. https://doi.org/10.1016/j.cemconcomp.2021.104022

[22] Sirico, A., Belletti, B., Bernardi, P., Malcevschi, A., Pagliari, F., Fornoni, P., & Moretti, E. (2022). Effects of biochar addition on long-term behavior of concrete. Theoretical and Applied Fracture

Mechanics, 122, 103626. https://doi.org/10.1016/j.tafmec.2022.103626

[23] Liu, W., Li, K., & Xu, S. (2022). Utilizing bamboo biochar in cement mortar as a bio-modifier to improve the compressive strength and crack-resistance fracture ability. Construction and Building Materials, 327, 126917. https://doi.org/10.1016/j.conbuildmat.2022.126917

[24] Ling, Y., Wu, X., Tan, K., & Zou, Z. (2023). Effect of biochar dosage and fineness on the mechanical properties and durability of concrete. Materials, 16(7), 2809. https://doi.org/10.3390/ma16072809

[25] Qing, L., Zhang, H., & Zhang, Z. (2023). Effect of biochar on compressive strength and fracture performance of concrete. Journal of Building Engineering, 78, 107587. https://doi.org/10.1016/j.jobe.2023.107587

[26] Jia, Y., Li, H., He, X., Li, P., & Wang, Z. (2023). Effect of biochar from municipal solid waste on mechanical and freeze–thaw properties of concrete. Construction and Building Materials, 368, 130374. https://doi.org/10.1016/j.conbuildmat.2023.130374

[27] Pang, X., Qin, Y., Wei, P., & Huang, C. (2024). Enhancing fire resistance: Investigating mechanical properties of biochar-infused concrete under elevated temperatures. Construction and Building Materials, 435, 136813. https://doi.org/10.1016/j.conbuildmat.2024.136813

[28] Mekky, K. M., Ibrahim, M. G., Sharobim, K., Fujii, M., & Nasr, M. (2024). Evaluating environmental and economic benefits of using biochar in concrete: A life cycle assessment and multi-criteria decision-making framework. Case Studies in Construction Materials, 21, e03712. https://doi.org/10.1016/j.cscm.2024.e03712

[29] Hylton, J., Hugen, A., Rowland, S. M., Griffin, M., & Tunstall, L. E. (2024). Relevant biochar characteristics influencing compressive strength of biochar-cement mortars. Biochar, 6(1), 1-27. https://doi.org/10.1007/s42773-024-00375-6

[30] Wang, T., Tang, Y., Qin, S., Li, G., Wu, H., & Leung, C. K. Y. (2025). Sustainable and mechanical properties of engineered cementitious composites with biochar: Integrating micro- and macro-mechanical insight. Cement and Concrete Composites, 155, 105813. https://doi.org/10.1016/j.cemconcomp.2024.105813

[31] ASTM C150/C150M. (2001). Standard specification for Portland cement. ASTM International. https://doi.org/10.1520/C0150_C0150M-21

[32] ASTM C188. (2009). Standard test method for density of hydraulic cement. ASTM International.

[33] EN 196-1. (2005). Methods of testing cement – Part 1: Determination of strength. European Committee for Standardization. https://doi.org/10.3403/30291447

[34] ASTM C109/C109M. (2011). Standard test method for compressive strength of hydraulic cement mortars. ASTM International. https://doi.org/10.1520/c0109_c0109m-13e01

[35] Nimmo, J. R., & Perkins, K. S. (2002). Aggregate stability and size distribution. In Methods of Soil Analysis: Part 4 Physical Methods (Vol. 5, pp. 317-328). Soil Science Society of America.

[36] ASTM C136/C136M. (2006). Standard test method for sieve analysis of fine and coarse aggregates. ASTM International.

[37] BS 812-110. (1990). Testing aggregates – Part 110: Methods for determination of aggregate crushing value (ACV). BSI, UK.

[38] ASTM C128. (2012). Standard test method for density, relative density (specific gravity), and absorption of fine aggregate. ASTM International. https://doi.org/10.1520/C0128-22

[39] ASTM C29/C29M. (2009). Standard test method for bulk density ("unit weight") and voids in aggregate. ASTM International.

[40] ASTM C142/C142M. (1998). Standard test method for clay lumps and friable particles in aggregates. ASTM International.

[41] Kucche, K. J., Jamkar, S. S., & Sadgir, P. A. (2015). Quality of water for making concrete: a review of literature. International Journal of Scientific and Research Publications, 5(1), 1-10. https://doi.org/10.12691/ajcea-7-2-1

[42] Christensen, B. J., & Farzam, H. (2006). Chemical admixtures. In Significance of Tests and Properties of Concrete and Concrete-Making Materials (pp. 484-494). ASTM International. https://doi.org/10.1520/stp37760s

[43] Dehkhoda, A. M., Ellis, N., & Gyenge, E. (2014). Electrosorption on activated biochar: effect of thermo-chemical activation treatment on the electric double layer capacitance. Journal of Applied Electrochemistry, 44, 141-157. https://doi.org/10.1007/s10800-013-0636-1

[44] Kang, X., Kang, G.-C., & Ge, L. (2013). Modified time of setting test for fly ash paste and fly ash–soil mixtures. Journal of Materials in Civil Engineering, 25(2), 296-301. https://doi.org/10.1061/(asce)mt.1943-5533.0000604

[45] ASTM C157/C157M. (2010). Standard test method for length change of hardened hydraulic-cement mortar and concrete. ASTM International.

[46] Al-Saleh, W. M., Almutairi, H. M., Sayyed, M. I., & Elsafi, M. (2024). A comprehensive study of the shielding ability from ionizing radiation of different mortars using iron filings and bismuth oxide. Scientific Reports, 14(1), 10014. https://doi.org/10.1038/s41598-024-60188-2

[47] El-Samrah, M. G., Nabil, I. M., Shamekh, M. E., Elmasry, M., & Osman, M. (2024). Microstructure and radiation shielding capabilities of Al-Cu and Al-Mn alloys. Scientific Reports, 14(1), 26721. https://doi.org/10.1038/s41598-024-76177-4

[48] Singh, V., Shirmardi, S. P., Medhat, M. E., & Badiger, N. M. (2015). Determination of mass attenuation coefficient for some polymers using Monte Carlo simulation. Vacuum, 119, 284-288. https://doi.org/10.1016/j.vacuum.2015.06.006

[49] Al-Ghamdi, H., Alsaif, N. A. M., Alfryyan, N., Rammah, Y. S., & Nabil, I. M. (2024). Investigation of gamma-ray and neutron protection competence of oxyfluoride aluminosilicate glasses reinforced with TbF3: Comparative study. Radiation Physics and Chemistry, 112105. https://doi.org/10.1016/j.radphyschem.2024.112105

[50] Şakar, E., Han, İ., Arslan, İ., & Singh, V. (2020). Phy-X/PSD: Development of a user friendly online software for calculation of parameters relevant to radiation shielding and dosimetry. Radiation Physics and Chemistry, 166, 108496.

[51] Mahmoud, A. A., Abouelnour, M. A., Fathy, I. N., Alturki, M., & Abdelaziz, M. (2024). Influence of sustainable waste granite, marble and nano-alumina additives on ordinary concretes: a physical, structural, and radiological study. Scientific Reports, 14(1), 22011.

[52] Fathy, I. N., El-Sayed, A. A., Elfakharany, M. E., Mahmoud, A. A., Mohamed, A. A., & Mahmoud, A. S. (2024). Enhancing mechanical properties and radiation shielding of high-strength concrete with bulk lead oxide and granodiorite. Nuclear Engineering and Design, 429, 113626. https://doi.org/10.1016/j.nucengdes.2024.113626

[53] Fathy, I. N., El-Sayed, A. A., Elfakharany, M. E., Mahmoud, A. A., Mohamed, A. A., & Mahmoud, A. S. (2025). Upgrading the compressive strength and radiation shielding properties of high strength concrete supported with nano additives of lead monoxide and granodiorite. Progress in Nuclear Energy, 180, 105562.

[54] Gupta, S., Kua, H. W., & Low, C. Y. (2018). Use of biochar as carbon sequestering additive in cement mortar. Cement and Concrete Composites, 87, 110-129. https://doi.org/10.1016/j.cemconcomp.2017.12.009

[55] Akinyemi, B. A., & Adesina, A. (2020). Recent advancements in the use of biochar for cementitious applications: A review. Journal of Building Engineering, 32, 101705. https://doi.org/10.1016/j.jobe.2020.101705

[56] Wang, L., Chen, L., Tsang, D. C. W., Kua, H. W., Yang, J., Ok, Y. S., ... & Poon, C. S. (2019). The roles of biochar as green admixture for sediment-based construction products. Cement and Concrete Composites, 104, 103348. https://doi.org/10.1016/j.cemconcomp.2019.103348

[57] Murali, G., & Wong, L. S. (2024). A comprehensive review of biochar-modified concrete: Mechanical performance and microstructural insights. Construction and Building Materials, 425, 135986.

[58] Gupta, S., Kua, H. W., & Pang, S. D. (2018). Biochar-mortar composite: Manufacturing, evaluation of physical properties and economic viability. Construction and Building Materials, 167, 874-889. https://doi.org/10.1016/j.conbuildmat.2018.02.104

[59] Gomes, S. D. C., Zhou, J. L., Zeng, X., & Long, G. (2022). Water treatment sludge conversion to biochar as cementitious material in cement composite. Journal of Environmental Management, 306, 114463. https://doi.org/10.1016/j.jenvman.2022.114463

[60] Yang, X., & Wang, X.-Y. (2021). Hydration-strength-durability-workability of biochar-cement binary blends. Journal of Building Engineering, 42, 103064. https://doi.org/10.1016/j.jobe.2021.103064

[61] Siddique, S., Shrivastava, S., & Chaudhary, S. (2018). Influence of ceramic waste as fine aggregate in concrete: Pozzolanic, XRD, FT-IR, and NMR investigations. Journal of Materials in Civil Engineering, 30(9), 04018227. https://doi.org/10.1061/(asce)mt.1943-5533.0002438

[62] Thomas, M., et al. (2008). Diagnosing delayed ettringite formation in concrete structures. Cement and Concrete Research, 38(6), 841-847.

[63] Kim, J. J., Foley, E. M., & Taha, M. M. R. (2013). Nano-mechanical characterization of synthetic calcium–silicate–hydrate (C–S–H) with varying CaO/SiO2 mixture ratios. Cement and Concrete Composites, 36, 65-70.

[64] Choudhary, R., et al. (2021). Mechanical and abrasion resistance performance of silica fume, marble slurry powder, and fly ash amalgamated high strength self-consolidating concrete. Construction and Building Materials, 269, 121282.

[65] Dadsetan, S., & Bai, J. (2017). Mechanical and microstructural properties of self-compacting concrete blended with metakaolin, ground granulated blast-furnace slag and fly ash. Construction and Building Materials, 146, 658-667.

[66] Abouelnour, M. A., Fathy, I. N., Mahmoud, A. A., Alturki, M., & Abdelaziz, M. (2024). Recycling of marble and granite waste in concrete by incorporating nano alumina. Construction and Building Materials, 411, 134456. https://doi.org/10.1016/j.conbuildmat.2023.134456

[67] Fathy, I. N., Elfakharany, M. E., & El-Sayed, A. A. (2024). Recycling of waste granodiorite powder as a partial cement replacement material in ordinary concrete. Advances in Materials Science, 24(3), 56-88.

[68] El-Samrah, M., et al. (2022). Radiation shielding properties of modified concrete mixes and their suitability in dry storage cask. Progress in Nuclear Energy, 148, 104195.

[69] Kassem, S. M., et al. (2023). Optical and radiation shielding properties of PVC/BiVO4 nanocomposite. Scientific Reports, 13(1), 10964. https://doi.org/10.1038/s41598-023-37916-7

[70] Saleh, A., et al. (2024). The role of MoO3 on the physical, elasto-mechanical and nuclear shielding efficiency of barium-boro-bismuthate glass system: Comparative investigation. Materials Chemistry and Physics, 129574.

[71] Ekinci, N., et al. (2022). Impacts of the colemanite on the enhancement of the radiation shielding capacity of polypropylene. Journal of Materials Science: Materials in Electronics, 33(25), 20046-20055. https://doi.org/10.1007/s10854-022-08803-w

[72] Al-Ghamdi, H., et al. (2024). Investigation of gamma-ray and neutron protection competence of oxyfluoride aluminosilicate https://doi.org/10.1016/j.radphyschem.2024.112105

[73] Kaky, K. M., et al. (2020). Theoretical and experimental validation gamma shielding properties of B2O3–ZnO–MgO–Bi2O3 glass system. Materials Chemistry and Physics, 242, 122504. https://doi.org/10.1016/j.matchemphys.2019.122504

[74] Japari, S., et al. (2021). Effects of Na2O on optical and radiation shielding properties of xNa2O-(20-x)K2O-30V2O5-50TeO2 mixed alkali glasses. Results in Physics, 22, 103946. https://doi.org/10.1016/j.rinp.2021.103946

[75] Kiran, K., et al. (2015). Effective atomic number of selected construction materials using gamma backscattering technique. Annals of Nuclear Energy, 85, 1077-1084.

[76] Martellucci, R., & Torsello, D. (2022). Potential of biochar reinforced concrete as neutron shielding material. Nuclear Engineering and Technology, 54(9), 3448-3451. https://doi.org/10.1016/j.net.2022.03.022

[77] Yasir, M., et al. (2020). Shielding properties of cement composites filled with commercial biochar. Electronics, 9(5), 819. https://doi.org/10.3390/electronics9050819

J-Researchers

Journal of Civil Engineering Researchers

Journal homepage: www.journals-researchers.com

From Agricultural Waste to Construction Material: The Necessity of Controlled Water Curing for CLR-Concrete

Zahra Heydari,[a] Rasoul Shadnia ,[b*] Davood Mostofinejad [c]

[a] Former M.Sc Student. of Civil Engineering, Hakim Sabzevari University, Sabzevar, Iran

[b] Associate Professor of Civil Engineering, Hakim Sabzevari University, Sabzevar, Iran

[c] Professor of Civil Engineering, Isfahan University of Technology, Isfahan, Iran

ABSTRACT

The sugar industry generates substantial agricultural waste, necessitating sustainable recycling pathways. This study explores the valorization of Carbonation Lime Residue (CLR), a waste from sugar beet processing, in concrete as a partial cement replacement. Given the critical impact of curing on performance, this research specifically investigates the effect of curing conditions on CLR-based concrete. Specimens with 0% to 40% CLR were prepared and subjected to two distinct curing regimes: stagnant water and controlled curing with periodic water replacement. Compressive strength was evaluated at 7, 28, 56, and 90 days, while the curing water was monitored for electrical conductivity (EC) and total dissolved solids (TDS). The results revealed that stagnant water curing led to a sharp decline in long-term strength, attributed to the leaching of impurities and a consequent harmful increase in water salinity. Conversely, controlled water curing with periodic refreshing prevented salt accumulation and facilitated a continuous strength gain for all mixes. A 20% cement replacement with CLR was found to be structurally viable under this proper curing method. This study conclusively demonstrates that controlled water curing is not merely beneficial but essential for producing durable green concrete from agricultural waste, effectively transforming it into a valuable construction material.

ARTICLE INFO

Received: May 05, 2026
Accepted: May 28, 2026

Keywords:
Carbonation Lime Residue (CLR)
Curing Conditions
Green Concrete
Compressive Strength
Agricultural Waste

DOI: 10.66224/JCER.8.2.42
DOR: 20.1001.1.2538516.2026.8.2.3.8

1. Introduction

The agricultural sector is a cornerstone of global food security, yet it simultaneously generates significant volumes of organic and inorganic waste streams. The sugar industry, intrinsically linked to the cultivation of sugar beet, is a prime example, producing by-products that pose considerable disposal challenges. Integrating these agricultural residues into value-added applications, particularly in the construction industry, presents a promising pathway toward a circular economy, reducing environmental burden and conserving natural resources.

Today, despite the remarkable progress of science in human societies and the high speed of industrialization and the establishment of large and small factories to meet the needs of the community, which is very gratifying, the production of large volumes of waste from these industries and factories is damaging and concerning. On the other hand, many of these wastes contain chemical and industrial materials that, if released into the environment, are harmful to humans and other living organisms in their surrounding

* Corresponding author. e-mail: r.shadnia@hsu.ac.ir

environment. These concerns have led most societies to remove waste and residues from their surroundings. One of the most practical options in waste management is recycling and optimal reuse, which, in addition to environmental benefits, can also generate income and lead to economic savings.

With the expansion of urbanization worldwide, the construction industry is a new and significant gateway for accepting recycled materials. Concrete is one of the most important and common building materials that, due to its advanced technology and expertise in its production, has opened its arms to accept industrial waste. Given the characteristics of concrete production and the flexibility in formulating its main constituent materials, concrete is one of the best platforms for testing and investigating industrial waste. On the other hand, using these materials as a substitute for cement, since cement itself is a major pollutant for the environment, significantly enhances the value of recycling.

During the production and operation process of sugar factories, a large amount of waste is generated, including pulp, molasses, and Carbonation Lime Residue (CLR). These wastes can be used as raw materials for producing other high-value products. Recently, several studies have investigated the use of molasses in the production of cement, mortar, and concrete [1-4]. Other research has focused on the reuse of pulp in other industries [5-14], especially the food industry [15-17]. However, currently, the biggest problem and waste of sugar factories is CLR. CLR is a mandatory by-product and waste of these factories, which is currently unused and generally accumulated in large volumes around the factories. Field surveys from several active sugar factories revealed that during peak operation periods, about 80 tons of CLR is obtained daily per factory [18]. The accumulation of this waste has caused environmental pollution in their surroundings and posed a serious disposal problem for sugar factories. Furthermore, follow-ups and warnings from Iran's environmental agencies have even led to the shutdown of some of these factories and their inclusion on the Environmental Protection Organization's blacklist As a result, sugar factories, to escape this issue and dispose of these materials, are sometimes forced to bury them, transfer them to other areas, or even dump them into nearby rivers. It is worth noting that unfortunately, due to the very high lime properties of these materials, this action causes irreparable damage to the environment, animals, and aquatic life in the areas. Dried Carbonation Lime Residue accumulated around sugar factories disperses as very fine powder in the surrounding environments. Furthermore, since sugar beet farms are usually located near most sugar factories, the dispersion of these materials clogs soil pores and disrupts plant growth processes.

Although CLR in sugar factories (due to the absorption of impurities from non-sugar contaminants during the sugar refining process) is different from original calcium carbonate, since these wastes have a lime origin, reviewing the results of studies where calcium carbonate replaced cement in concrete production can be beneficial [19-25]. Unfortunately, few studies on the recycling of CLR have been reported so far. Recently, research has been conducted on the effect of using this waste as a soil stabilizer [26], on various parameters of geopolymers [27-30], polymer concretes [31], cement [32], and ordinary Portland concrete [33-35]. A review of the literature indicates that Heidari et al. [33], Gharieb and Rashad [34], and Phuyal et al. [35] are among the limited researchers who have so far investigated the reuse of CLR waste in concrete production. Heidari et al. [33] investigated the effect of the method of using this waste on the mechanical properties of concrete through laboratory experiments. They used three different methods, including dissolving in mix design water, sieving, and grinding, to replace cement in concrete production with different percentages of CLR. Their experimental results demonstrated that the optimal method for utilizing CLR in concrete is to incorporate it in a ground form. Their findings indicated that replacing up to at least 20% of the cement by weight with this processed waste is feasible, resulting in only a minimal reduction in concrete strength. Gharieb and Rashad [34] also investigated the effect of replacing cement with CLR in different ratios between 5% and 25% by weight on the compressive strength, specific weight, water absorption, and porosity of concrete. Their laboratory test results showed that the best replacement ratio is 5%, and higher replacement ratios lead to a decrease in the compressive strength of concrete. The laboratory investigations of Phuyal et al. [35] showed that increasing the percentage replacement of cement with CLR in concrete production reduces the compressive, tensile, and flexural strengths of concrete. It is predicted that by introducing these materials into the construction industry and producing environmentally friendly green concrete, a large volume of this type of sugar factory waste can be consumed and recycled, and the problem of accumulating this waste, which has become problematic for their environment, can be completely or largely eliminated, providing profitability for both industries. However, to improve the efficiency, the best curing conditions for concrete produced with this type of waste must be investigated.

Effectively implementing any procedure or method to optimize concrete curing conditions requires sufficient expertise and a deep understanding of the process. To ensure the practical applicability of these methods, a comprehensive study is essential. Utilizing previous research significantly accelerates this process [36-40]. In general, the results of these studies highlight the critical importance of proper curing and its impact on the properties of hardened concrete. In other words, curing influences all characteristics of hardened concrete. For instance, the required duration for protecting and curing concrete depends on factors including the type of cementitious materials used, mix proportions, specified strength, the size and shape of the concrete element, and the ambient temperature and humidity during and after the curing period.

Therefore, given the significant role of curing in developing the strength and durability of concrete, and considering the lack of attention paid to this aspect in previous research on carbonated green concrete, the primary objective of current research is to identify the optimal curing conditions. This aims to facilitate the more practical utilization of sugar factory waste (CLR) as a partial replacement for cement in concrete production, ultimately paving the way for the processing and commercialization of this type of green concrete.

2. Materials and Proposed Research Methodology

In this research, Type II Portland cement produced by Ardestan Cement Factory located in Isfahan city (Iran) was used. Potable water available in the laboratory was also used, and the maximum water-to-cement ratio in the mixes was considered to be 0.35. The gradation of the used sand and gravel was evaluated based on National Standard No. 302 (Iran). Pea gravel and sand were obtained from the Noor complex mine, and crushed mountain almond gravel was obtained from the Paya Sang mine, all from Isfahan city (Iran). Waste Carbonation Lime Residue produced at the Naghsh-e Jahan Sugar Factory in Isfahan was used as a cement replacement in the production of carbonated green concrete. It is worth noting that the specifications of all used materials, including cement, water, aggregates, and CLR, are in accordance with the research presented by Heidari et al. [33].

To make the cylindrical concrete specimens containing different replacement percentages of 5%, 10%, 20%, 30%, and 40% as a substitute for part of the cement, this waste (whose appearance is shown in Figure 1) was first powdered using an industrial grinder to make its particle size more uniform and similar to cement [33]. The control specimens were prepared without adding any waste powder. For each mix design, 15 cylindrical specimens were made to determine the compressive strength at 7, 28, 56, and 90 days, noting that three extra molds were also kept for inspection and evaluation of the concrete when necessary. The reported compressive strength for each mix design was obtained by averaging the compressive strength of three specimens.

According to Standard Building Regulations, concrete curing is a process during which moisture loss from the concrete is prevented and the temperature of the concrete is maintained at a satisfactory level. While preliminary investigations highlight the importance of curing for concrete containing waste CLR, this subject remains still unexplored. To address this gap, two curing methods were evaluated: curing by the use of a pond with stagnant, non-replaceable water (Figure 2), and a pond equipped with water replacement system (Figure 3). A comparative analysis of the compressive strength results was then conducted.

Figure 1. Granulation and composition of CLR particles in nature

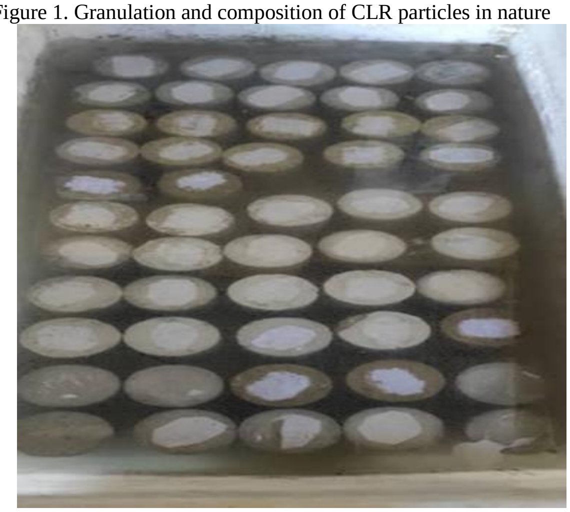

Figure 2. Sample storage pond with stagnant and non-replaceable water

3. Results and Discussion

3.1. Results of compressive strength of concrete specimens cured using a pond with stagnant, non-replaceable water

The results of compressive strength tests for concrete specimens cured in a pond with stagnant, non-replaceable water are shown in Figure 4. Scrutinizing the results easily shows that the strength of the specimens had an upward trend until the first 28 days after production, but after about two months, the compressive strength of the specimens decreased sharply; such that the compressive strength of the 56 and 90-day specimens decreased significantly. It is worth mentioning that the three additional specimens prepared in all mixes, which were made and kept for necessity, deteriorated after a 120-day period, and their strength decreased severely, to the extent that some specimens easily disintegrated with hand pressure, as can be seen in Figure 5.

Figure 3. Sample storage pond with temperature control and replaceable water

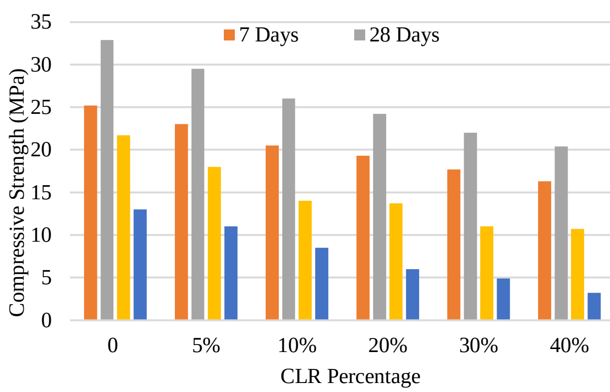

Figure 4. Compressive strength of concrete specimens containing different percentages of CLR cured using a pond with stagnant, non-replaceable water

It is reminded that at this stage, the produced specimens were placed next to each other in the pond with stagnant, non-replaceable water. Visual observations after one month indicated a change in the color of the water and the formation of sludge inside the pond. Visual inspection also indicated that a layer of white residue gradually formed on the surface of the specimens, as shown in Figure 6. The reason for this can be related to the presence of impurities and organic materials in the concrete specimens containing CLR and their seepage in contact with water.

Figure 5. Loss of strength and disintegration of concrete specimens cured using a pond with stagnant, non-replaceable water after 120 days.

Figure 6. Appearance changes of specimens cured using a pond with stagnant, non-replaceable water after one month

To investigate the cause of the severe strength reduction in specimens cured in the stagnant ponds, the pond water was analyzed. Water samples were collected from the curing ponds at five different intervals (30, 45, 60, 75, and 90 days) and subjected to chemical testing. The results of these analyses are presented in Figure 7.

Electrical Conductivity (EC) measures a solution's ability to conduct electricity, which is directly related to its ionic concentration. Total Dissolved Solids (TDS) represents the total concentration of dissolved inorganic salts and minerals in the water, often referred to as water hardness. A higher EC value indicates a greater concentration of ions, while a higher TDS value signifies increased mineral content and harder water. The significance of these parameters lies in their correlation with the corrosivity of water; a higher EC generally indicates a higher corrosion rate under similar conditions. Although EC and TDS are distinct parameters, they exhibit a strong and direct correlation. However, the exact ratio between TDS and EC varies for different water samples, depending on the specific composition and concentration of dissolved impurities.

Standard guidelines recommend that the TDS in concrete curing ponds should not exceed 1000 mg/L to prevent potential damage. However, as detailed Figure 7, the TDS in the stagnant curing ponds increased progressively over time. Within two months of introducing the specimens, the TDS surpassed the 1000 mg/L threshold, reaching over 3000 mg/L after three months—a level comparable to seawater salinity and detrimental to concrete made with Type II Portland cement. Therefore, it can be concluded that curing CLR-containing concrete in stagnant water ponds leads to a significant accumulation of salts in the water. This increase in salinity, which intensifies with prolonged curing duration, is the primary cause of the observed severe strength reduction in the specimens.

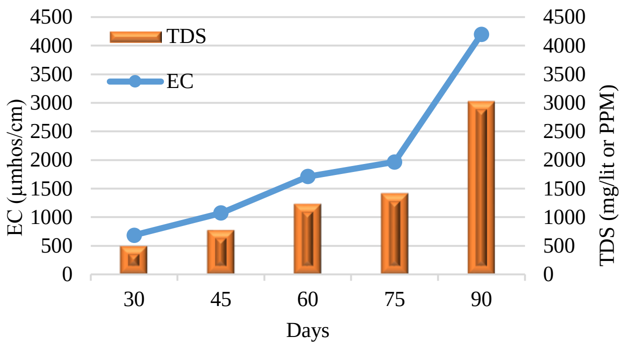

Figure 7. Results of water chemical tests after different intervals (pond with stagnant, non-replaceable water)

3.2. Results of compressive strength of concrete specimens cured using ponds equipped with temperature control and water replacement system

In response to the significant strength reduction observed in specimens cured in stagnant water, a controlled curing system was designed and implemented to mitigate the detrimental effects of salt accumulation. This system featured dedicated ponds equipped with temperature control and water replacement system, ensuring a stable and homogeneous curing environment. To maintain water quality, a protocol was established for complete water replacement every two weeks, or whenever visual inspection indicated cloudiness, thereby preventing the buildup of dissolved ions leached from CLR.

Using the same mix designs as the initial phase, a new set of cylindrical specimens was cast with CLR replacement levels of 0%, 5%, 10%, 20%, 30%, and 40% by weight of cement. These specimens were then subjected to the improved curing regime, and their compressive strength was evaluated at 7, 28, 56 and 90 days. The results, summarized in Figure 8, demonstrate a markedly different and more favorable trend compared to stagnant water curing.

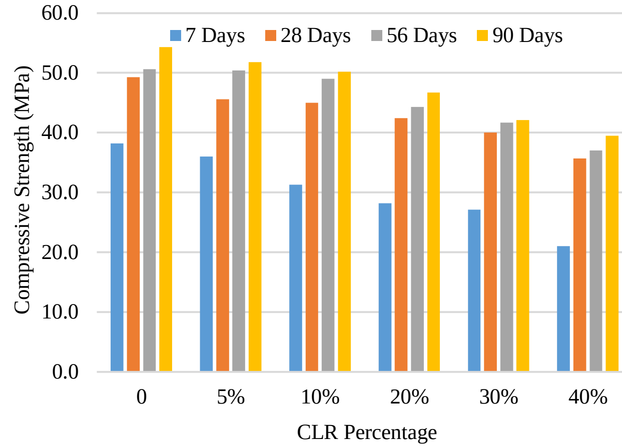

Figure 8. Compressive strength of concrete specimens containing different percentages of CLR cured using a pond equipped with temperature control and water replacement system.

The compressive strength development under controlled curing conditions is shown in Figure 8. The data indicate consistent strength gain for all mixes throughout the 90-day curing period. As expected, incorporating CLR generally led to a reduction in compressive strength compared to the control specimens (0% CLR), attributable to cement dilution and the lower reactivity of CLR. However, a significant finding emerges that at replacement levels up to 20%, the strength reduction remained relatively modest. For instance, the 20% CLR mix achieved approximately 42 MPa at 28 days and 44 MPa at 56 days, compared to the control's 49 MPa and 50 MPa, respectively—representing a strength retention of about 86-88%. This suggests that replacement ratios up to 20% are structurally viable for many applications.

Furthermore, the results reveal an important long-term trend; while the control mix showed minimal strength gain beyond 28 days, the CLR-containing mixes exhibited continued strength development between 28 and 90 days. This sustained hydration suggests a possible pozzolanic or filler effect from the processed CLR that compensates for the initial cement dilution and contributes to long-term strength development.

The stark contrast between the two curing methods is undeniable. The controlled curing environment, characterized by water periodic replacement, successfully prevented the spike in water salinity (as measured by TDS and EC) that was detrimental in the stagnant ponds. Consequently, all specimens cured under controlled conditions remained sound and intact throughout the testing period, with no signs of the deterioration that plagued their stagnant-water counterparts. This compelling evidence allows us to conclude that the severe strength loss previously observed was not an inherent property of CLR-concrete, but rather a direct consequence of an unsuitable curing method. Therefore, the adoption of a managed curing regime, which controls water chemistry through periodic replacement, is not merely beneficial but essential for realizing the full structural potential of green concrete incorporating waste Carbonation Lime Residue.

4. Conclusion

This study demonstrates a viable pathway for recycling agricultural waste from the sugar industry into construction materials. By investigating the use of Carbonation Lime Residue (CLR) in green concrete, it was established that the curing method is the critical factor determining its structural viability. Specimens were subjected to two distinct curing regimes: stagnant water and controlled curing with periodic water replacement. Evaluation of compressive strength results and chemical analysis of the water yielded the following key findings:

- Stagnant Water Curing: Curing in ponds with stagnant water led to a severe decline in strength at later ages (56 and 90 days). Chemical analysis of the water revealed a progressive increase in salinity resulting from the leaching of impurities from the CLR. This highly corrosive environment not only halted strength development but also caused progressive deterioration of the specimens, to the extent that 120-day specimens completely lost their integrity and could be disintegrated by hand.
- Controlled Curing with Periodic Water Replacement: In contrast, curing under controlled conditions (with periodic water replacement) resulted in a consistent and sustained increase in strength up to 90 days for all mix designs. Although incorporating CLR at levels up to 40% led to an overall reduction in strength compared to the control, the reduction for replacements up to 20% was limited (approximately 14% at 28 days). More importantly, mixes containing CLR exhibited a significant rate of strength gain between 28 and 90 days. For instance, the 20% CLR mix showed only a 12% reduction in strength compared to the control at 90 days. This behavior indicates a possible prolonged pozzolanic or filler effect from the processed CLR, which continues at later ages and compensates for the initial strength loss due to cement dilution.

This study clearly demonstrates that the curing method is a critical factor determining the performance of green concrete containing CLR. Curing in stagnant water is entirely unsuitable due to the creation of a corrosive, and high-salinity environment. Conversely, a managed curing regime with regular water replacement to control the chemical quality of the water is essential for achieving durable strength development and realizing the full potential of this green concrete. Consequently, a replacement level of up to 20% CLR, when coupled with proper curing, presents a viable and reliable option for structural applications.

5. Acknowledgments

The authors sincerely acknowledge the Isfahan Concrete Foundation Company, particularly its Manager, Dr. Haj Rasouliha, and Mr. Sadeghi. The assistance provided by the technical staff of the Concrete Foundation Laboratory, especially Messrs. Sokhanvar, Kuchaknezhad, and Mohammadi, is also gratefully appreciated. Furthermore, the valuable cooperation of the Naghsh-e Jahan Sugar Factory, notably Dr. Deybakhsh and Dr. Khayyam, is deeply acknowledged."

References

[1] Gao, X., Yang, Y., & Deng, H. (2011). Utilization of beet molasses as a grinding aid in blended cements. Construction and BuildingMaterials, 25(9), 3782-3789.https://doi.org/10.1016/j.conbuildmat.2011.04.014

[2] Jumadurdiyev, A., Ozkul, M. H., Saglam, A. R., & Parlak, N. (2005). The utilization of beet molasses as a retarding and water-reducing admixture for concrete. Cement and Concrete Research, 35(5), 874-882.https://doi.org/10.1016/j.cemconres.2004.05.044

[3] Ali, B., & Qureshi, L. A. (2019). Durability of recycled aggregate concrete modified with sugarcane molasses. Construction and Building Materials, 229, 116913. https://doi.org/10.1016/j.conbuildmat.2019.116913

[4] [4] Huang, G., Pudasainee, D., Gupta, R., & Liu, W. V. (2020). Utilization and performance evaluation of molasses as a retarder and plasticizer for calcium sulfoaluminate cement-based mortar. Construction and Building Materials, 243, 118201.https://doi.org/10.1016/j.conbuildmat.2020.118201

[5] Puligundla, P., & Mok, C. (2021). Valorization of sugar beet pulp through biotechnological approaches: recent developments. Biotechnology Letters, 43(7), 1253-1263. https://doi.org/10.1007/s10529-021-03097-6

[6] Ziemiński, K., & Kowalska-Wentel, M. (2017). Effect of different sugar beet pulp pretreatments on biogas production efficiency. Applied Biochemistry and Biotechnology, 181, 1211-1227. https://doi.org/10.1007/s12010-016-2283-3

[7] Joanna, B., Michal, B., Piotr, D., Agnieszka, W., Dorota, K., & Izabela, W. (2018). Sugar beet pulp as a source of valuable biotechnological products. In Advances in Biotechnology for Food Industry (pp. 359-392). Academic Press.

[8] Borysiuk, P., Jenczyk-Tolloczko, I., Auriga, R., & Kordzikowski, M. (2019). Sugar beet pulp as raw material for particleboard production. Industrial Crops and Products, 141, 111829. https://doi.org/10.1016/j.indcrop.2019.111829

[9] Alves de Oliveira, R., Schneider, R., Hoss Lunelli, B., Vaz Rossell, C. E., Maciel Filho, R., & Venus, J. (2020). A simple biorefinery concept to produce 2G-lactic acid from sugar beet pulp (SBP): A high-value target approach to valorize a waste stream. Molecules, 25(9), 2113. https://doi.org/10.3390/molecules25092113

[10] [10] Rana, A. K., Gupta, V. K., Newbold, J., Roberts, D., Rees, R. M., Krishnamurthy, S., & Thakur, V. K. (2022). Sugar beet pulp: Resurgence and trailblazing journey towards a circular bioeconomy. Fuel, 312, 122953. https://doi.org/10.1016/j.fuel.2021.122953
[11] Martinez, M., Gullon, B., Schols, H. A., Alonso, J. L., & Parajo, J. C. (2009). Assessment of the production of oligomeric compounds from sugar beet pulp. Industrial & Engineering Chemistry Research, 48(10), 4681-4687.https://doi.org/10.1021/ie8017753
[12] Suffo, M., De La Mata, M., & Molina, S. I. (2020). A sugar-beet waste based thermoplastic agro-composite as substitute for raw materials. Journal of Cleaner Production, 257, 120382. https://doi.org/10.1016/j.jclepro.2020.120382
[13] Caliceti, C., Malaguti, M., Marracino, L., Barbalace, M. C., Rizzo, P., & Hrelia, S. (2022). Agri-food waste from apple, pear, and sugar beet as a source of protective bioactive molecules for endothelial dysfunction and its major complications. Antioxidants, 11(9), 1786. https://doi.org/10.3390/antiox11091786
[14] Aljabri, M., Alharbi, S., Al-Qthanin, R. N., Ismaeil, F. M., Chen, J., & Abou-Elwafa, S. F. (2021). Recycling of beet sugar byproducts and wastes enhances sugar beet productivity and salt redistribution in saline soils. Environmental Science and Pollution Research, 28, 45745-45755. https://doi.org/10.1007/s11356-021-13903-x
[15] Schiavon, S., Tagliapietra, F., Bailoni, L., & Bortolozzo, A. (2004). Effects of sugar beet pulp on growth and health status of weaned piglets. Italian Journal of Animal Science, 3(4), 337-351. https://doi.org/10.4081/ijas.2004.337
[16] Wang, L. F., Beltranena, E., & Zijlstra, R. T. (2016). Diet nutrient digestibility and growth performance of weaned pigs fed sugar beet pulp. Animal Feed Science and Technology, 211, 145-152. https://doi.org/10.1016/j.anifeedsci.2015.11.008
[17] Bodas, R., Giráldez, F. J., López, S., Rodríguez, A. B., & Mantecón, A. R. (2007). Inclusion of sugar beet pulp in cereal-based diets for fattening lambs. Small Ruminant Research, 71(1-3), 250-254. https://doi.org/10.1016/j.smallrumres.2006.07.007
[18] Heydari, Z., Shadnia, R., & Mostofinejad, D. (2023). Characterization and comparison with the addition of fresh and old carbonation lime residue powder for the production of carbonated concrete. In Third International Conference on Architecture, Civil Engineering, Urban Development, Environment and Horizons of Islamic Art... Tabriz, Iran (in Persian).
[19] Salman, M. M., & Muttar, A. A. (2017). The mechanical properties of lime concrete. Journal of Engineering and Sustainable Development, 21(2), 180-191.
[20] Cao, M., Ming, X., He, K., Li, L., & Shen, S. (2019). Effect of macro-, micro-and nano-calcium carbonate on properties of cementitious composites—A review. Materials, 12(5), 781. https://doi.org/10.3390/ma12050781
[21] Acharya, P. K., Patro, S. K., & Moharana, N. C. (2016). Effect of lime on mechanical and durability properties of blended cement based concrete. Journal of the Institution of Engineers (India): Series A, 97, 71-79. https://doi.org/10.1007/s40030-016-0153-5
[22] Nejad, F. M., Tolouei, M., Nazari, H., & Naderan, A. (2018). Effects of calcium carbonate nanoparticles and fly ash on mechanical and permeability properties of concrete. Advances in Civil Engineering Materials, 7(1), 651-668. https://doi.org/10.1520/ACEM20180045
[23] Adesina, P. A., & Olutoge, F. A. (2019). Structural properties of sustainable concrete developed using rice husk ash and hydrated lime. Journal of Building Engineering, 25, 100804. https://doi.org/10.1016/j.jobe.2019.100804
[24] Ali, M., Abdullah, M. S., & Saad, S. A. (2015). Effect of calcium carbonate replacement on workability and mechanical strength of Portland cement concrete. Advanced Materials Research, 1115, 137-141. https://doi.org/10.4028/www.scientific.net/AMR.1115.137
[25] Maruyama, I., Kotaka, W., Kien, B. N., Kurihara, R., Kanematsu, M., Hyodo, H., ... & Noguchi, T. (2021). A new concept of calcium carbonate concrete using demolished concrete and CO2. Journal of Advanced Concrete Technology, 19(10), 1052-1060. https://doi.org/10.3151/jact.19.1052
[26] Phuyal, K., Sharma, U., Mahar, J., Mondal, K., & Mashal, M. (2023). Reducing carbon footprint with precipitated calcium carbonate (PCC) in geotechnical applications.
[27] Rashad, A. M., & Gharieb, M. (2021). Valorization of sugar beet waste as an additive for fly ash geopolymer cement cured at room temperature. Journal of Building Engineering, 44, 102989. https://doi.org/10.1016/j.jobe.2021.102989
[28] Rashad, A. M., Zeedan, S. R., & Gharieb, M. (2024). Appreciation of sugar beet waste in metakaolin geopolymer mortar for compressive strength and drying shrinkage. Sustainable Chemistry and Pharmacy, 37, 101429. https://doi.org/10.1016/j.scp.2023.101429
[29] Rashad, A. M., Gharieb, M., Shoukry, H., & Mokhtar, M. M. (2022). Valorization of sugar beet waste as a foaming agent for metakaolin geopolymer activated with phosphoric acid. Construction and Building Materials, 344, 128240. https://doi.org/10.1016/j.conbuildmat.2022.128240
[30] Gharieb, M., & Rashad, A. M. (2022). Impact of sugar beet waste on strength and durability of alkali-activated slag cement. ACI Materials Journal, 119(2). https://doi.org/10.14359/51734345
[31] Sapronova, Z., Sverguzova, S., Fomina, E., & Fokina, E. (2018). Carbonate-containing precipitate of sugar production from sugar beet as filler for polymer concrete. In IOP Conference Series: Materials Science and Engineering (Vol. 365, No. 3, p. 032042). IOP Publishing. https://doi.org/10.1088/1757-899X/365/3/032042
[32] Li, H., Xu, W., Yang, X., & Wu, J. (2014). Preparation of Portland cement with sugar filter mud as lime-based raw material. Journal of Cleaner Production, 66, 107-112. https://doi.org/10.1016/j.jclepro.2013.11.003
[33] Heydari, Z., Shadnia, R., Mostofinejad, D., & Rezaei, S. (2024). The effect of the method of using waste carbonate cake on the compressive and tensile strength of green concrete. Ferdowsi Civil Engineering, 37(3). https://doi.org/10.22067/jfcei.2024.88715.1307
[34] Gharieb, M., & Rashad, A. M. (2020). An initial study of using sugar-beet waste as a cementitious material. Construction and Building Materials, 250, 118843. https://doi.org/10.1016/j.conbuildmat.2020.118843
[35] Phuyal, K., Sharma, U., Mahar, J., Mondal, K., & Mashal, M. (2023). A sustainable and environmentally friendly concrete for structural applications. Sustainability, 15(20), 14694. https://doi.org/10.3390/su152014694
[36] Yang, L., Shi, C., Liu, J., & Wu, Z. (2021). Factors affecting the effectiveness of internal curing: A review. Construction and Building Materials, 267, 121017. https://doi.org/10.1016/j.conbuildmat.2020.121017

[37] Shi, C., Liu, M., He, P., & Ou, Z. (2012). Factors affecting kinetics of CO2 curing of concrete. *Journal of Sustainable Cement-Based Materials, 1*(1-2), 24-33. https://doi.org/10.1080/21650373.2012.727322

[38] [38] Pawar, Y., & Kate, S. (2020). Curing of concrete: A review. International Research Journal of Engineering and Technology, 7, 1820-1824.

[39] Wang, J., An, J., Li, Y., Xiang, Y., Xiao, Q., Tang, Z., & Long, G. (2024). Influencing factors of the temperature rise of direct electric curing concrete and its effect on concrete properties. Construction and Building Materials, 438, 137110. https://doi.org/10.1016/j.conbuildmat.2024.137110

[40] Sidhu, A. S., & Siddique, R. (2024). Review on effect of curing methods on high strength concrete. Construction and Building Materials, 438, 136858. https://doi.org/10.1016/j.conbuildmat.2024.136858

Journal of Civil Engineering Researchers

Journal homepage: www.journals-researchers.com

Seismic Retrofit of Corrosion-Damaged Reinforced Concrete Bridges Using Fiber-Reinforced Polymer Composites: A Comprehensive Review

Elham Rajabpor,[a,*]

[a] *Department of Civil Engineering, Cha.C., Islamic Azad University, Chalus, Iran.*

ABSTRACT

Reinforced concrete (RC) bridges worldwide are increasingly vulnerable to seismic events and deterioration mechanisms, particularly reinforcement corrosion. This review paper examines the application of Fiber-Reinforced Polymer (FRP) composites as an innovative solution for seismic retrofitting of corrosion-damaged RC bridges. FRP materials offer exceptional properties including high strength-to-weight ratio, excellent corrosion resistance, ease of installation, and minimal geometric modification of structural elements. The paper synthesizes findings from recent experimental and numerical studies on FRP-strengthened RC members, with emphasis on beams, columns, slabs, and bridge pile applications. Key aspects discussed include the corrosion mechanisms affecting steel reinforcement, the electrochemical implications of FRP-steel interaction, and the comparative performance of various FRP types including carbon, glass, and aramid fibers under seismic loading conditions. The review demonstrates that properly designed FRP retrofitting systems can significantly enhance flexural and shear capacity, ductility, and energy dissipation of corrosion-damaged bridge components. However, careful consideration must be given to galvanic coupling effects when carbon FRP is employed in chloride-contaminated concrete environments. This paper contributes to the growing body of knowledge on sustainable infrastructure rehabilitation and provides practical insights for engineers engaged in bridge retrofit projects.

ARTICLE INFO

Received: February 27, 2026
Accepted: April 06, 2026

Keywords:
Seismic retrofitting
Reinforced concrete bridges
Corrosion damage
Fiber-reinforced polymers
Structural strengthening
FRP composites
Bridge rehabilitation
Galvanic corrosion

DOI: 10.66224/JCER.8.2.50
DOR: 20.1001.1.2538516.2026.8.2.4.9

1. Introduction

Aging infrastructure presents one of the most significant challenges facing civil engineers in the twenty-first century. Reinforced concrete bridges, which form the backbone of transportation networks worldwide, are particularly susceptible to deterioration mechanisms that compromise their structural integrity and seismic resilience. Among these deterioration processes, reinforcement corrosion stands as the most prevalent and damaging phenomenon, affecting countless bridges constructed during the mid-to-late twentieth century (Mohammadizadeh et al., 2021).

The vulnerability of existing RC bridges is further exacerbated by evolving seismic design codes, increased traffic demands, and changing environmental conditions. Many bridges designed according to outdated standards lack adequate ductility, shear capacity, and confinement

[*] Corresponding author. Tel: +989118632016; Email: Elham.Rajabpour@iau.ir,

details necessary to withstand moderate to strong seismic events. Consequently, there exists an urgent need for effective retrofitting strategies that can extend service life, enhance seismic performance, and ensure public safety.

Traditional retrofitting approaches, including steel jacketing, concrete enlargement, and external post-tensioning, have demonstrated effectiveness but are accompanied by significant drawbacks. These conventional methods often add considerable weight to the structure, require extensive labor and specialized equipment, increase member dimensions (reducing clearance), and remain susceptible to further corrosion degradation (Farahi et al., 2018). Moreover, the implementation of such techniques in operational bridges poses logistical challenges and often necessitates prolonged traffic disruptions.

Fiber-Reinforced Polymer composites have emerged as a transformative technology in the field of structural rehabilitation since their first application in Switzerland in 1984 (Habibpour & Farhang, 2014). These advanced materials, consisting of high-strength fibers embedded in a polymeric matrix, offer compelling advantages over traditional retrofitting methods.

The lightweight nature of FRP composites—approximately one-fifth that of steel—combined with their exceptional tensile strength (2-5 times that of reinforcing steel) and inherent corrosion resistance makes them particularly attractive for bridge applications (Anup Chole et al., 2023).

The adoption of FRP for seismic retrofitting gained momentum during the 1980s when Katsumata and colleagues pioneered their use for enhancing the seismic resistance of RC columns in Japan (Habibpour & Farhang, 2014). Since then, extensive research has explored the behavior of FRP-strengthened RC members under various loading conditions, leading to the development of design guidelines and widespread acceptance in the engineering community. The flexibility of FRP systems allows their application to beams, columns, slabs, joints, and even submerged pile foundations, making them versatile tools for comprehensive bridge retrofitting programs. Despite the considerable advantages of FRP composites, their application to corrosion-damaged structures introduces complexities that warrant careful examination. The interaction between carbon-based FRP materials and corroding steel reinforcement can generate galvanic couples, potentially accelerating localized corrosion in chloride-contaminated concrete (Khedmatgozar Dolati et al., 2023). Furthermore, the long-term durability of the FRP-concrete bond under aggressive environmental conditions remains an active area of investigation.

This review paper aims to synthesize current knowledge on the seismic retrofitting of corrosion-damaged RC bridges using FRP composites. Specific objectives include: (1) examining the corrosion mechanisms affecting bridge structures and their implications for seismic performance; (2) evaluating the mechanical properties and behavioral characteristics of various FRP types; (3) reviewing recent experimental and numerical studies on FRP-strengthened bridge components; (4) assessing the galvanic compatibility of FRP with corroding steel reinforcement; and (5) identifying knowledge gaps and future research directions. By consolidating findings from international research, this paper provides engineers and researchers with a comprehensive understanding of FRP-based retrofitting strategies for corrosion-damaged bridges.

2. Corrosion Deterioration in Reinforced Concrete Bridges

2.1. Mechanisms of Reinforcement Corrosion

Reinforcement corrosion in concrete bridges occurs through two primary mechanisms: carbonation-induced corrosion and chloride-induced corrosion. Both processes disrupt the passive oxide layer that normally protects steel reinforcement within the alkaline concrete environment (pH 12.5-13.5).

Carbonation results from the reaction of atmospheric carbon dioxide with calcium hydroxide in concrete, progressively reducing the pH of the pore solution to approximately 8-9. At this reduced alkalinity, the passive layer destabilizes, allowing uniform corrosion to initiate across extensive areas of reinforcement. This phenomenon typically affects older bridge structures with inadequate concrete cover or poor-quality concrete (Soltani Mohammadi & Safaian, 2012).

Chloride-induced corrosion, conversely, represents a more aggressive and localized deterioration mechanism. Chlorides from deicing salts, marine environments, or industrial sources penetrate the concrete cover and, upon reaching a critical concentration threshold at the reinforcement depth, disrupt the passive layer locally. The resulting pitting corrosion can cause severe cross-section loss without extensive surface manifestations, making detection challenging until significant damage has occurred.

The corrosion process itself involves electrochemical reactions at anodic and cathodic sites on the reinforcement surface. At anodic sites, iron dissolves according to:

$$Fe \rightarrow Fe^{2+} + 2e^-$$

Simultaneously, at cathodic sites, oxygen reduction occurs:

$$O_2 + 2H_2O + 4e^- \rightarrow 4OH^-$$

The ferrous ions combine with hydroxyl ions to form ferrous hydroxide, which further oxidizes to various iron oxides and hydroxides collectively known as rust.

Critically, these corrosion products occupy volumes 2-6 times greater than the original steel, generating substantial expansive pressures within the surrounding concrete (Huynh-Xuan et al., 2023).

2.2. Structural Consequences of Corrosion Damage

The volumetric expansion accompanying reinforcement corrosion produces three interrelated damage mechanisms that progressively degrade bridge structural performance.

First, the expansive pressures induce tensile stresses in the surrounding concrete, leading to cracking along the reinforcement axis. These longitudinal cracks typically initiate at the steel-concrete interface and propagate outward toward the concrete surface. As corrosion progresses, crack widths increase, and additional cracks form perpendicular to the reinforcement, eventually causing spalling and delamination of the concrete cover. Such cover loss not only reduces the effective cross-section but also exposes reinforcement to accelerated corrosion, creating a self-perpetuating deterioration cycle.

Second, corrosion progressively reduces the cross-sectional area of reinforcing bars, directly diminishing their load-carrying capacity. The relationship between corrosion level and strength reduction is nonlinear, with localized pitting causing more severe capacity degradation than uniform section loss of equivalent mass. Pitting corrosion, characteristic of chloride attack, can reduce bar ductility and may precipitate brittle fracture under seismic loading (Tin Huynh-Xuan et al., 2023).

Third, the accumulation of corrosion products at the steel-concrete interface fundamentally alters bond behavior. Initially, rust formation may increase apparent bond strength through mechanical interlock and increased confinement. However, as corrosion progresses, the friable rust layer lubricates the interface, and the development of splitting cracks progressively destroys bond integrity. This bond deterioration compromises the composite action essential to reinforced concrete behavior, potentially leading to anchorage failures and excessive deflections.

The combined effects of section loss, concrete degradation, and bond deterioration render corrosion-damaged bridges particularly vulnerable to seismic loading. The reduced ductility and energy dissipation capacity of corroded members may precipitate brittle failure modes during earthquake ground motions, underscoring the importance of timely intervention through appropriate retrofitting strategies.

2.3. Implications for Seismic Performance

Corrosion damage affects all aspects of seismic response in RC bridge components. In columns, the primary vertical load-carrying elements, corrosion of transverse reinforcement reduces confinement and shear capacity, potentially triggering brittle shear failures before flexural hinging can develop. Corrosion of longitudinal reinforcement compromises flexural capacity and may precipitate low-cycle fatigue failures under cyclic loading.

Bridge piers exposed to marine environments or deicing salts often exhibit accelerated corrosion in the splash zone, where cyclic wetting and drying promotes chloride ingress. This localized deterioration can create "weak stories" in the structural system, concentrating seismic damage in already compromised regions. Furthermore, corrosion at beam-column joints—typically congested with reinforcement—can precipitate joint shear failures with catastrophic consequences for overall structural stability.

The interaction between corrosion damage and seismic demands necessitates retrofitting approaches that address both deteriorated material conditions and inadequate detailing relative to modern code requirements. FRP composites offer unique advantages in this context, providing supplemental reinforcement without adding significant mass or requiring extensive demolition of existing concrete.

3. Fiber-Reinforced Polymer Composites: Material Characteristics

3.1. Constituent Materials and Manufacturing

Fiber-Reinforced Polymer composites are heterogeneous materials consisting of high-strength fibers embedded within a polymeric matrix. The fibers, which provide primary load-carrying capacity, may be continuous or discontinuous and oriented to optimize performance in specific directions. The matrix, typically epoxy, vinyl ester, or polyester resin, transfers stresses between fibers, protects fibers from environmental attack, and determines the composite's durability characteristics.

Three fiber types dominate civil engineering applications:

Carbon FRP (CFRP) offers the highest tensile strength (2400-3700 MPa) and modulus of elasticity (150-580 GPa), making it suitable for applications requiring significant stiffness enhancement. Carbon fibers exhibit excellent fatigue resistance and creep behavior but are electrically conductive, creating potential galvanic compatibility issues with steel reinforcement (Ram et al., 2019).

Glass FRP (GFRP) provides tensile strengths comparable to steel (480-1600 MPa) but with lower modulus (35-65 GPa) and higher elongation at failure. The lower cost of GFRP makes it economically attractive for many applications, though its susceptibility to alkali attack and stress corrosion requires careful consideration in concrete environments (Maliki et al., 2021).

Aramid FRP (AFRP) offers intermediate properties between carbon and glass, with good impact resistance and non-conductive behavior. However, its high cost and sensitivity to ultraviolet radiation limit widespread adoption in bridge retrofitting.

FRP composites are available in various forms for structural strengthening applications. Pre-cured laminates and strips provide consistent quality and are bonded to concrete surfaces using epoxy adhesives. Wet layup systems, wherein dry fabrics are saturated with resin on-site, offer flexibility for irregular geometries and are particularly suitable for column wrapping applications. Near-surface mounted (NSM) systems involve embedding FRP bars or strips into grooves cut into the concrete cover, providing enhanced bond and protection from environmental exposure (Abdoli & Mostofinejad, 2023).

3.2. Mechanical Properties and Behavior

The mechanical behavior of FRP composites differs fundamentally from that of conventional construction materials. Unlike steel, which exhibits ductile yielding followed by strain hardening, FRP materials demonstrate linear elastic behavior up to brittle failure. This absence of plasticity has significant implications for seismic design, where energy dissipation typically relies on inelastic deformation of reinforcement.

The tensile strength and modulus of FRP composites depend primarily on fiber type, fiber volume fraction, and fiber orientation. Unidirectional composites, with all fibers aligned in the load direction, maximize strength and stiffness in that orientation but offer minimal resistance to transverse or shear stresses. Multidirectional laminates, incorporating fibers at various orientations, provide more balanced properties at the cost of reduced axial capacity.

The compressive behavior of FRP differs markedly from tension response, with compressive strengths typically 30-50% of tensile values. This anisotropy necessitates careful consideration in applications subject to stress reversals, such as seismic loading.

Critical to retrofitting applications is the bond behavior between FRP and concrete. The effectiveness of externally bonded FRP relies on adequate stress transfer across the concrete-FRP interface through the adhesive layer. Premature debonding, often initiating at intermediate cracks or terminating at laminate ends, represents a common failure mode that limits the strain utilization of FRP reinforcement. Various anchorage techniques, including U-wraps, mechanical fasteners, and end plates, have been developed to delay or prevent debonding failures (Nematzadeh et al., 2021).

3.3. Durability Considerations

While FRP composites offer inherent corrosion resistance, their long-term durability under service conditions requires careful evaluation. The polymeric matrix may degrade under ultraviolet radiation, elevated temperatures, and moisture exposure. Glass fibers are susceptible to stress corrosion and alkali attack, necessitating resin systems that provide adequate protection. Carbon fibers, though chemically stable, may facilitate galvanic corrosion when coupled with steel reinforcement in conductive environments.

Fire performance represents a particular concern for FRP-strengthened structures. The organic matrix softens and decomposes at temperatures above the glass transition temperature (typically 60-80°C for epoxy systems), potentially leading to bond failure and loss of composite action. Fire protection measures, including insulation layers or sacrificial concrete cover, may be necessary for critical applications.

4. FRP Retrofitting Strategies for Bridge Components

4.1. Column Strengthening and Confinement

Bridge columns, as critical load-bearing elements, have been the focus of extensive FRP retrofitting research. The primary objective of column strengthening is to enhance confinement, thereby increasing compressive strength, ductility, and shear capacity. FRP wraps, with fibers oriented predominantly in the hoop direction, provide continuous confinement that effectively restrains lateral expansion of concrete under axial compression.

The confinement mechanism in FRP-wrapped columns differs fundamentally from that provided by steel ties. While steel yields and maintains constant confining pressure, FRP exhibits linear elastic behavior, with confining pressure increasing proportionally to lateral expansion. This passive confinement becomes active only after concrete dilation, providing maximum confinement at peak load and beyond.

Experimental investigations have demonstrated remarkable improvements in the behavior of FRP-confined columns. Axial compressive strength increases of 50-200% have been reported, depending on FRP stiffness and thickness. More significantly, the axial strain capacity increases dramatically, transforming brittle concrete behavior into a highly ductile response with extensive post-peak strain capacity (Shen et al., 2019).For seismic applications, FRP wrapping provides multiple benefits:

Shear strengthening through fibers oriented at 90° to the column axis directly resists diagonal tension stresses, increasing shear capacity by 30-100% depending on wrap configuration. This enhancement can suppress brittle shear failures, allowing flexural hinging to develop and dissipate seismic energy.

Flexural ductility enhancement through confinement of the plastic hinge region increases the ultimate compressive strain capacity of concrete, enabling larger curvature demands without core crushing. FRP wraps also restrain longitudinal bar buckling under cyclic loading, preserving flexural capacity through multiple inelastic cycles. Lap splice clamping in columns with inadequately detailed lap splices represents a critical application. FRP wraps provide passive confinement that suppresses splice failure, allowing development of full bar yield strength under seismic loading.

Recent research by Shi-Jie Mei et al. (2023) investigated the seismic behavior of shear-critical square RC columns strengthened with large rupture strain (LRS) FRP. Their experimental program demonstrated that LRS FRP wrapping increased displacement ductility by 491.7% and energy dissipation by 6498.3% compared to control specimens. Notably, columns strengthened with LRS FRP exhibited progressive failure modes, while CFRP-wrapped columns under high axial load showed sudden explosive failure, highlighting the advantages of high-elongation FRP systems for seismic retrofitting.

4.2. Beam Strengthening

Bridge beams and girders require strengthening for flexure, shear, or both, depending on deficiency type. FRP systems can be configured to address each failure mode through appropriate fiber orientation and placement.

Flexural strengthening is accomplished by bonding FRP laminates or sheets to the tension face of beams, providing additional reinforcement that acts compositely with the existing section. The FRP contribution to flexural capacity depends on its area, tensile strength, and effective strain at ultimate. However, the linear elastic behavior of FRP means that its full strength cannot be realized unless the section undergoes large rotations, potentially leading to concrete crushing before FRP rupture (Osama A. Mohamed et al., 2023).

Design considerations for flexural strengthening include:

· Balanced reinforcement ratio to ensure ductile failure modes (concrete crushing) rather than brittle FRP rupture

· End anchorage to prevent premature debonding initiating at laminate ends

· Crack control through intermediate crack debonding provisions

· Serviceability limits to control deflections and crack widths under service loads

Shear strengthening employs FRP with fibers oriented perpendicular to the beam axis or at 45° to intersect shear cracks. U-wraps, fully-wrapped sections, or side-bonded strips can be configured based on access constraints and deficiency severity. The shear contribution of FRP is limited by the effective strain that can be developed, which depends on the wrap configuration and anchorage conditions.

Wang et al. (2022) demonstrated that CFRP-strengthened beams exhibited 30-50% increases in shear capacity with properly anchored U-wraps. The combination of flexural and shear strengthening can restore or exceed the original capacity of corrosion-damaged beams while improving ductility through confinement of the compression zone.

4.3. Slab and Deck Strengthening

Bridge decks and approach slabs, subject to direct traffic loading and environmental exposure, often require strengthening to accommodate increased load ratings or to repair corrosion damage. FRP systems for slab strengthening include:

Flexural strengthening of one-way slabs using longitudinally oriented FRP strips bonded to the tension surface. Two-way slabs require reinforcement in both directions, with proper detailing at continuity regions. FRP application to the top surface of slabs may be necessary for negative moment regions, though protection from traffic abrasion and environmental exposure must be considered.

Punching shear strengthening around column supports in flat slab bridges employs FRP fans or grids to intercept critical shear cracks. The thin profile of FRP reinforcement (typically 1-3 mm) minimizes aesthetic impact and maintains clearance, advantages particularly valuable in parking structures and pedestrian bridges.

Corrosion protection through FRP application reduces moisture ingress and chloride penetration, slowing ongoing corrosion processes. While FRP does not arrest active corrosion, its barrier function can extend the service life of repaired elements when combined with appropriate corrosion mitigation measures.

4.4. Pile and Substructures

Bridge piles and substructure elements present unique challenges for retrofitting, particularly when partially submerged or embedded in soil. FRP systems offer solutions for these difficult access conditions through their lightweight, corrosion-resistant, and easily transportable characteristics.

Submerged pile retrofitting has been demonstrated using wet layup FRP systems applied within cofferdams or by divers in underwater applications. The rapid curing of specially formulated resins allows construction within tidal cycles, minimizing disruption to waterway traffic. FRP wrapping of corroded piles restores confinement, increases flexural and shear capacity, and provides a barrier against further chloride ingress.

Research by Wu et al. (2023) on submerged floating tunnels reinforced with FRP rigid trusses demonstrated the viability of FRP for challenging marine environments. Their findings indicated that FRP reinforcement significantly improved vibration performance and structural integrity under hydrodynamic loading.

4.5. Joint Retrofitting

Beam-column joints in bridge structures represent critical regions where seismic performance is often governed by complex interaction of forces and reinforcement details. Corrosion damage at joints is particularly problematic due to reinforcement congestion and difficulty of inspection.

FRP retrofitting of joints employs a combination of orientations to address multiple failure modes. Diagonal wrapping resists joint shear stresses, while horizontal and vertical strips provide anchorage for beam and column reinforcement passing through the joint. Mohammadizadeh and Hosseinzadeh (2022) conducted numerical analysis of FRP-strengthened exterior beam-column joints under cyclic loading, demonstrating significant improvements in strength, stiffness, and energy dissipation capacity. Their finite element models, calibrated against experimental results, showed that properly designed FRP wrapping transformed brittle joint failures into ductile beam-hinging mechanisms.

5. Interaction of FRP with Corroding Reinforcement

5.1. Galvanic Coupling Mechanisms

The application of carbon FRP to corrosion-damaged RC structures introduces electrochemical considerations not present with conventional retrofitting materials. Carbon fibers, like graphite, are electrically conductive and exhibit noble electrochemical potentials relative to steel in concrete environments. When CFRP is electrically connected to steel reinforcement through the concrete pore solution or direct contact, a galvanic couple may form, potentially accelerating corrosion of the less noble steel.

The galvanic corrosion mechanism involves electron transfer from the anodic steel (which oxidizes) to the cathodic CFRP (where oxygen reduction occurs). The driving force for this reaction is the potential difference between the two materials, which can exceed 0.5 V in chloride-contaminated concrete (Gholizadeh, 2016). The magnitude of galvanic current depends on the relative areas of anode and cathode, the conductivity of the concrete electrolyte, and the kinetics of the cathodic reaction on the CFRP surface.

Research has demonstrated that CFRP can indeed act as an effective cathode, supporting oxygen reduction at rates sufficient to generate significant galvanic currents. Khedmatgozar Dolati et al. (2023) reported that CFRP laminates coupled with steel in chloride-contaminated concrete produced macrocell currents several times larger than those observed with passive steel cathodes. This effect is particularly pronounced in splash zone conditions where oxygen availability is high.

5.2. Implications for Retrofitting Design

The potential for galvanic corrosion does not preclude CFRP use in corrosion-damaged structures but does require careful design consideration. Several mitigation strategies have been developed:

Electrical isolation of CFRP from reinforcement through the use of insulating layers (glass fiber scrims or non-conductive adhesives) breaks the galvanic circuit. However, ensuring complete isolation in field conditions is challenging, and minor defects may create localized coupling.

Barrier protection through complete encapsulation prevents electrolyte access to the CFRP-steel interface. Properly detailed FRP wraps that seal the concrete surface may actually reduce corrosion rates by limiting oxygen and moisture availability, outweighing any galvanic effects.

Sacrificial anodes or impressed current cathodic protection can be incorporated into the retrofitting system to provide active corrosion control. These approaches add complexity but may be justified for severely contaminated structures.

Material selection favoring non-conductive FRP types (glass or aramid) eliminates galvanic concerns entirely. GFRP and AFRP offer electrically insulating behavior while providing mechanical properties suitable for many retrofitting applications.

5.3. Repair of Corrosion-Damaged Concrete Prior to FRP Application

The condition of the underlying concrete fundamentally influences FRP retrofitting effectiveness and durability. Corrosion-damaged concrete typically contains cracks, delaminations, and chloride contamination that must be addressed before FRP application.

Proper surface preparation involves:

· Removal of delaminated and spalled concrete to sound substrate

· Cleaning of corroded reinforcement to remove rust products, though complete removal of tightly adherent rust may be impractical

· Application of corrosion inhibitors or sacrificial anodes in contaminated areas

· Re-profiling with repair mortars to restore geometric continuity

· Surface grinding to achieve required flatness for FRP bonding

The extent of concrete removal required for durable repair remains debated. Some researchers advocate for complete removal of chloride-contaminated concrete, while others accept limited contamination beneath FRP wraps, relying on the barrier effect to control future corrosion. Huynh-Xuan et al. (2023) investigated the effect of pre-existing corrosion on FRP-confined columns under eccentric loads, finding that moderate corrosion levels did not preclude effective strengthening, though careful bond assessment was essential.

6. Recent Research Advances

6.1. Experimental Investigations

Recent experimental programs have expanded understanding of FRP retrofitting for corrosion-damaged structures. Mohammadizadeh et al. (2021) employed wavelet transformation techniques to detect damage progression in FRP-strengthened RC sections under flexural and torsional loading. Their approach identified cracking, yielding, and ultimate capacity thresholds through signal processing of load-response data, demonstrating the potential for structural health monitoring integrated with FRP retrofitting.

Nematzadeh et al. (2021) developed analytical models for FRP-strengthened beam-column joints, incorporating nonlinear behavior through diagonal strut-and-tie modeling. Their approach successfully predicted load-deformation response and failure modes observed in experimental programs, providing design tools for practical application.

Maliki et al. (2021) investigated deep concrete beams reinforced with GFRP bars, examining parameters including concrete cover thickness, compressive reinforcement, and reinforcement ratio. Their results demonstrated that increased GFRP ratio improved load capacity by up to 46% compared to singly reinforced sections, though crack widths and deflections exceeded those of steel-reinforced control beams.

6.2. Numerical Modeling Advances

Finite element analysis has enabled parametric investigation of FRP retrofitting beyond experimental constraints. Sophisticated material models now capture:

· Concrete confinement through plasticity-based formulations incorporating FRP hoop strain limits

· Bond-slip behavior at the FRP-concrete interface using cohesive zone models

· Corrosion effects through reduced bar areas, modified bond properties, and explicit modeling of corrosion product expansion

· Cyclic degradation under seismic loading incorporating stiffness and strength deterioration

Abdoli and Mostofinejad (2023) developed analytical models for torsional behavior of FRP-strengthened RC members considering various wrapping configurations. Their theoretical predictions, validated against extensive experimental databases, captured the contribution of longitudinal and transverse FRP to torsional capacity and identified optimal wrapping schemes for different member geometries.

6.3. Field Applications and Case Studies

While laboratory research provides fundamental understanding, field applications demonstrate practical viability. Documented FRP retrofitting projects for bridges include:

· I-275 Bridge, Michigan - CFRP wrapping of corroded pier columns

· Hayakawa Bridge, Japan - Seismic retrofitting of RC piers with aramid FRP

· Various UK highway structures - Flexural strengthening of bridge decks with CFRP laminates

These applications have demonstrated construction time savings of 50-70% compared to conventional methods, with minimal traffic disruption and excellent long-term performance under service conditions.

7. Design Considerations and Code Provisions

7.1. International Design Guidelines

Several countries have developed design guidelines for FRP strengthening of concrete structures. Notable documents include:

· ACI 440.2R-17 (USA) - Guide for the Design and Construction of Externally Bonded FRP Systems

· fib Bulletin 14 (Europe) - Externally bonded FRP reinforcement for RC structures

· CNR-DT 200 R1/2013 (Italy) - Guide for the Design and Construction of Externally Bonded FRP Systems

· Concrete Society Technical Report 55 (UK) - Design guidance for strengthening concrete structures using fibre composite materials

These documents address material characterization, design philosophies, strength reduction factors, and serviceability requirements, providing a framework for safe and effective FRP application.

7.2. Key Design Parameters

Critical design considerations for seismic retrofitting include:

Confinement effectiveness quantified through confinement ratios relating FRP stiffness to concrete strength. The enhanced concrete compressive strength and ultimate strain are calculated using models calibrated to experimental databases.

Shear contribution of FRP determined from effective strain limits that account for debonding and fracture. The angle of principal stress and interaction with existing transverse reinforcement influence capacity calculations.

Development length requirements ensuring that FRP can achieve its design strength before debonding. Anchorage details at laminate ends and intermediate crack locations are specified to prevent premature failures.

Environmental reduction factors accounting for long-term exposure effects on FRP material properties. These factors vary by fiber type, exposure condition, and performance period.

Seismic detailing provisions for FRP in plastic hinge regions include minimum wrap lengths, corner radius requirements to prevent stress concentrations, and lap splice details for prefabricated jackets.

8. Conclusions and Future Directions

8.1. Summary of Findings

This comprehensive review has examined the application of FRP composites for seismic retrofitting of corrosion-damaged RC bridges. The following conclusions can be drawn:

1. FRP composites offer exceptional advantages for bridge retrofitting, including high strength-to-weight ratio, corrosion resistance, ease of installation, and minimal geometric modification. These characteristics make FRP particularly suitable for seismic upgrading of existing structures where weight addition and construction disruption must be minimized.

2. Corrosion damage in RC bridges progressively degrades structural performance through concrete cracking, reinforcement section loss, and bond deterioration. The combined effects render corroded bridges particularly vulnerable to seismic loading, necessitating timely intervention.

3. FRP retrofitting effectively addresses corrosion-induced deficiencies through confinement enhancement, supplemental shear and flexural reinforcement, and barrier protection against further chloride ingress. Column wrapping can increase displacement ductility by 400-600% and energy dissipation by over 6000% compared to unstrengthened corroded members.

4. Carbon FRP may participate in galvanic corrosion when applied to chloride-contaminated structures, though proper design detailing can mitigate this effect. Glass and aramid FRP eliminate galvanic concerns while providing adequate mechanical properties for many applications.

5. Recent research advances include sophisticated numerical models, damage detection techniques using signal processing, and experimental validation of retrofitting strategies for various bridge components.

8.2. Knowledge Gaps and Research Needs

Despite significant progress, several knowledge gaps warrant further investigation:

Long-term durability of FRP-strengthened corrosion-damaged structures under combined environmental exposure and cyclic loading requires extended monitoring periods. The interaction between ongoing corrosion and FRP confinement over decades remains poorly quantified.

Performance under multi-hazard scenarios including earthquake followed by fire, or corrosion combined with fatigue loading, needs systematic investigation to ensure robust design.

Non-destructive evaluation techniques for assessing FRP bond condition and detecting hidden corrosion beneath FRP wraps require development and validation.

Standardized design procedures for corrosion-damaged substrates that account for reduced bond capacity and uncertain reinforcement condition would enhance reliability.

Life-cycle cost analysis comparing FRP retrofitting with conventional methods over extended time horizons would inform infrastructure investment decisions.

8.3. Concluding Remarks

Fiber-Reinforced Polymer composites represent a mature and effective technology for seismic retrofitting of corrosion-damaged reinforced concrete bridges. The extensive research base developed over four decades provides confidence in design approaches, while ongoing innovations continue to expand application possibilities. As bridge infrastructure worldwide ages and seismic design requirements evolve, FRP retrofitting will play an increasingly vital role in extending service life, enhancing public safety, and ensuring the resilience of transportation networks against natural hazards. The integration of corrosion science, structural engineering, and materials technology exemplified by FRP retrofitting demonstrates the multidisciplinary approach necessary to address the complex challenges of infrastructure rehabilitation in the twenty-first century.

References

[1] Abdoli, M., & Mostofinejad, D. (2023). Torsional behavior of FRP-strengthened reinforced concrete members considering various wrapping configurations: Theoretical analysis and modeling. Construction and Building Materials, 401, 132636. https://doi.org/10.1016/j.conbuildmat.2023.132636

[2] Anup Chole, A., Tembhurne, A., Bawanthade, A., Bhadade, H., Khan, H. A., & Shaw, S. K. (2023). Strengthening of reinforced concrete beams by using FRPs-An overview. Materials Today: Proceedings. Advance online publication, 17 May 2023.

[3] Farahi, B., Esfahani, M., & Sabzi, J. (2018). Behavior of reinforced concrete beams reinforced with NSM-SMA/FRP method. Amirkabir Civil Engineering, 51(4), 685-698. https://doi.org/10.22060/ceej.2018.14573.5602

[4] Gholizadeh, S. (2016). A review of non-destructive testing methods of composite materials. Procedia Structural Integrity, 1, 5-5. https://doi.org/10.1016/j.prostr.2016.02.008

[5]

[6] Habibpour, M., & Farhang, F. (2014). Reinforcement of reinforced concrete columns using multidirectional FRP composites. Concrete Research, 8(2), 113-124.

[7] Huynh-Xuan, T., Do-Dai, T., Ngo-Huu, C., Pham, T. M., & Nguyen-Minh, L. (2023). Effect of corroded reinforcement on capacity of square reinforced concrete columns confined with FRP sheets under eccentric loads. Engineering Structures, 218, 115821. https://doi.org/10.1016/j.engstruct.2023.115821

[8] Khedmatgozar Dolati, S. S., Malla, P., Ortiz, J. D., Mehrabi, A., & Nanni, A. (2023). Identifying NDT methods for damage detection in concrete elements reinforced or strengthened with FRP. Engineering Structures, 218, 116155. https://doi.org/10.1016/j.engstruct.2023.116155

[9] Maliki, F., Qalehaki, M., Khairuddin, A., & Rezaeifar, O. (2021). Investigating the behavior of deep concrete beams reinforced with FRP rebars. Concrete Research, 14(3), 83-93.

[10] Mohammadizadeh, M., & Hosseinzadeh, S. (2022). Numerical analysis of external reinforced concrete beam-column joints reinforced using FRP under the effect of cyclic loads. Civil and Environmental Engineering, 52(1), 169-183.

[11] Mohammadizadeh, M., Salami, S., et al. (2021). Estimation of cracking, yielding and ultimate capacity of reinforced concrete and steel reinforced sections using FRP with the help of wavelet transformation. Amirkabir Civil Engineering, 53(5), 1937-1958.

[12] Nematzadeh, M., Baharlu, S., Shayanfar, J., & Hosni, S. M. R. (2021). Simulation of the effects of FRP sheets on the nonlinear behavior of reinforced concrete beam-column joints. Civil Infrastructure Research, 7(1), 131-151.

[13] Osama A. Mohamed, O. A., Kewalramani, M. A., & Imran, A. M. (2023). Shear and flexure of FRP-reinforced concrete beams and slabs. Materials Today: Proceedings. Advance online publication, 20 April 2023. https://doi.org/10.1016/j.matpr.2023.04.220

[14] Ram, I., Sabri, V., Sabri, H., Ram, A. M., Ram, A. H., & Sadeghi, A. A. (2019). Evaluation of cyclic performance of reinforced concrete frames reinforced with different FRP patterns. New Approaches in Civil Engineering, 4(2), 74-8.

[15] Shen, Q., Wang, J., Wang, J., & Ding, Z. (2019). Axial compressive performance of circular CFST columns partially wrapped by carbon FRP. Journal of Constructional Steel Research, 155, 9-106. https://doi.org/10.1016/j.jcsr.2018.12.017

[16] Shi-Jie Mei, S.-J., Bai, Y.-L., Dai, J.-G., & Han, Q. (2023). Seismic behaviour of shear critical square RC columns strengthened by large rupture strain FRP. Engineering Structures, 240, 115679. https://doi.org/10.1016/j.engstruct.2023.115679

[17] Soltani Mohammadi, M., & Safaian, A. (2012). Behavioral models of reinforced concrete element repaired with FRP coating after reinforcement corrosion. Amirkabir Civil Engineering, 45(2), 13-29.

[18] Wang, Y., Chen, H., Li, Y., Chen, J., & Zhuang, N. (2022). Numerical and experimental investigation on the chloride ion resistance of reinforced concrete piles externally bonded with CFRP sheets under dry-wet cycles. Construction and Building Materials, 359, 129521. https://doi.org/10.1016/j.conbuildmat.2022.129521

[19] Wu, Z., Cheng, Z., Garg, A., Jiang, M., Meng, X., & Mei, G. (2023). Investigating anti-vibration performance of a novel three-tube submerged floating tunnel reinforced with FRP rigid truss. Ocean Engineering, 269, 113447.

[20] Zhang, J., Lin, G., Vaidya, U., et al. (2023). Past, present and future prospective of global carbon fibre composite developments and applications. Composites Part B, 250, 110463. https://doi.org/10.1016/j.compositesb.2022.110463

Journal of Civil Engineering Researchers

Journal homepage: www.journals-researchers.com

Optimal Aggregate Content in Recycled Concrete

Amir Najjarpour Kojoor,[a,*] Hamed Hemati Poorgashti [a]

[a] *Department of Civil Engineering, Maziyar Institute of Higher Education, Royan, Iran*

ABSTRACT

The rapid increase in concrete waste has emerged as a significant global environmental challenge. In addition, the depletion of natural resources commonly used in concrete production highlights the necessity of adopting sustainable alternative materials. The incorporation of recycled aggregates in new concrete is considered an effective approach to reducing environmental degradation and preserving natural resources. This study aims to evaluate the influence of replacing natural coarse aggregates with recycled coarse aggregates on the properties of fresh and hardened concrete. For this purpose, three replacement levels—0%, 50%, and 100%—were examined. A slump test was conducted to assess the workability of fresh concrete, while 28-day hardened samples were subjected to compressive strength, direct tensile strength, and indirect tensile (splitting) strength tests. The results indicate that increasing the replacement ratio of recycled aggregates leads to a notable reduction in compressive strength as well as direct and indirect tensile strengths. Furthermore, higher proportions of recycled aggregates significantly decreased the slump value, thereby reducing the workability of fresh concrete. These findings suggest that although the use of recycled aggregates is environmentally advantageous, their incorporation requires careful technical considerations in concrete mix design.

ARTICLE INFO

Received: December 30, 2025
Accepted: May 12, 2026

Keywords:
Recycled Concrete Aggregate
Compressive Strength
Indirect Tensile Strength
Direct Tensile Strength
Structure

DOI: 10.66224/JCER.8.2.59
DOR: 20.1001.1.2538516.2026.8.2.5.0

1. Introduction

Concrete use has been expanding rapidly worldwide in recent years. With this increasing demand, the shortage of natural aggregate sources is becoming a significant concern. In the near future, it is expected that natural aggregate quarries will experience depletion, forcing us to look for suitable alternatives. Due to the limited lifespan of concrete structures and their destruction caused by natural disasters such as earthquakes, floods, and storms, massive volumes of demolished concrete waste are generated. Landfilling this waste creates serious environmental issues. Reusing old demolished concrete as recycled concrete aggregate (RCA) in new concrete production helps conserve natural resources, preserve the environment, reduce energy consumption, and lower construction costs [1,2]. Research on the reuse of demolished concrete for new concrete aggregates dates back to post–World War II reconstruction efforts. Khalaf and his colleagues were among the first to recycle concrete waste obtained from structures destroyed during the war in Germany [3]. Since then, extensive research has been conducted in developed countries regarding the feasibility of using recycled aggregates in new concrete. In Europe, the United States, and Japan, a significant percentage of construction and demolition (C&D) waste comes from demolished concrete

[*] Corresponding author. Tel: +989028973883; Email: najjarpour.amir007@gmail.com,

structures. For example: Nearly 67% of construction waste in the U.S. consists of concrete. Around 50% of C&D waste in Europe is concrete [4]. Japan produces 19% of its total waste from demolished concrete—approximately 70 million tons per year [6]. In Iran, rapid housing development has increased the volume of C&D waste. In Tehran alone, nearly 12 million tons of construction debris are generated annually.

Table 1.
Test Types and Curing Plan

Mix ID	Sample Dimensions	Number of Samples	Curing Method	Test Type
RC0, RC50, RC100	15*15*15 cm cube	3	moist	Compressive strength
RC0, RC50, RC100	15*30 cm cylinder	3	moist	Indirect tensile strength
RC0, RC50, RC100	15*30 cm cylinder	3	moist	Direct Tensile Strength

Test Age:28days

2. Experimental Program

The goal of this study is to use recycled concrete aggregates (RCA) as coarse aggregates at replacement levels of 0%, 50%, and 100% relative to natural aggregates. After mixing, slump tests were performed on fresh concrete, and the mechanical properties of hardened concrete cured under moist conditions were evaluated. A summary of the sample dimensions, number of specimens, test types, and curing periods is presented in Table 1.

3. Materials

Ordinary Portland Pozzolanic Cement (Fars & Khuzestan Cement Co.) was used in all mixes. Fine aggregates (0–6 mm) and natural coarse aggregates (10–19 mm) were used. Recycled coarse aggregates were produced by crushing old concrete specimens using a laboratory crusher. Before crushing, the concrete samples were cleaned to remove contaminants. Drinking water from Rasht was used in concrete production.

4. Concrete Mix Design

Four mix designs with different water–cement ratios (w/c = 0.4 and 0.5) and different maximum aggregate sizes (10 mm and 19 mm) were used.

Table 2 shows the mixing plan for different water to cement ratios. Also, Tables 3 to 6 show the RCA replacement rate at different water to cement ratios.

Table 2.
Mix Design for Different Water–Cement Ratios

Mix No.	Mix ID	Cement(kg/m3)	Water(kg/m3)	Sand(kg/m3)	Gravel(kg/m3)
1	Mix Design 1:(w/c = 0.4, max aggregate 19mm)	365	128	139	51
2	Mix Design 2:(w/c = 0.4, max aggregate 10mm)	271	128	389	51
3	Mix Design 3:(w/c = 0.5, max aggregate 19mm)	366	128	307	65
4	Mix Design 4:(w/c = 0.5, max aggregate 10mm)	270	128	375	65

Table 3.
w/c = 0.5, Max, Aggregate Size = 19mm

Mix ID	Cement(kg)	Water(kg)	Sand(kg)	Natural Coarse(kg)	RCA(kg)
RC0	366	128	307	366	0
RC50	366	128	307	183	183
RC100	366	128	307	65	366

Table 4.
w/c = 0.5, Max, Aggregate Size = 10mm

Mix ID	Cement(kg)	Water(kg)	Sand(kg)	Natural Coarse(kg)	RCA(kg)
RC0	270	128	375	270	0
RC50	270	128	375	135	135
RC100	270	128	375	0	270

Table 5.
w/c = 0.4, Max, Aggregate Size = 19mm

Mix ID	Cement(kg)	Water(kg)	Sand(kg)	Natural Coarse(kg)	RCA(kg)
RC0	365	128	319	365	0
RC50	365	128	319	183	183
RC100	365	128	319	0	366

Table 6.
w/c = 0.4, Max, Aggregate Size = 10mm

Mix ID	Cement(kg)	Water(kg)	Sand(kg)	Natural Coarse(kg)	RCA(kg)
RC0	271	128	389	271	0
RC50	271	128	389	135	135
RC100	271	128	389	0	270

5. Results

5.1. Compressive Strength Results

Table 7.
Compressive Strength, w/c = 0.4, 19 mm Aggregates

Mix ID	28-Day Compressive Strength (Mpa)
RC0	36.10
RC50	32.70
RC100	24.30

Table 8.
Compressive Strength, w/c = 0.4, 10 mm Aggregates

Mix ID	28-Day Compressive Strength (Mpa)
RC0	36.20
RC50	31.20
RC100	27.20

Table 9.
Compressive Strength, w/c = 0.5, 19 mm Aggregates

Mix ID	28-Day Compressive Strength (Mpa)
RC0	40.10
RC50	35.50
RC100	30.10

Table 10.
Compressive Strength, w/c = 0.5, 10 mm Aggregates

Mix ID	28-Day Compressive Strength (Mpa)
RC0	39.90
RC50	36.20
RC100	28.20

5.2. Indirect Tensile Strength (Brazilian Test)

Table 11.
Brazilian Tensile Strength, w/c = 0.4, 19 mm Aggregates

Mix ID	28-Day Compressive Strength (Mpa)
RC0	2.80
RC50	2.62
RC100	2.15

Table 12.
Brazilian Tensile Strength, w/c = 0.4, 10 mm Aggregates

Mix ID	28-Day Compressive Strength (Mpa)
RC0	2.92
RC50	2.78
RC100	2.29

Table 13.
Brazilian Tensile Strength, w/c = 0.5, 19 mm Aggregates

Mix ID	28-Day Compressive Strength (Mpa)
RC0	3.40
RC50	2.70
RC100	2.30

Table 14.
Brazilian Tensile Strength, w/c = 0.5, 10 mm Aggregates

Mix ID	28-Day Compressive Strength (Mpa)
RC0	3.80
RC50	2.39
RC100	2.03

5.3. Direct Tensile Strength

Table 15.
Direct Tensile Strength, w/c = 0.4, 19mm

Mix ID	28-Day Compressive Strength (Mpa)
RC0	2.24
RC50	2.00
RC100	1.52

Table 16.
Direct Tensile Strength, w/c = 0.4, 10mm

Mix ID	28-Day Compressive Strength (Mpa)
RC0	2.34
RC50	1.95
RC100	1.83

Table 17.
Direct Tensile Strength, w/c = 0.5, 19mm

Mix ID	28-Day Compressive Strength (Mpa)
RC0	2.72
RC50	1.89
RC100	1.61

Table 18.
Direct Tensile Strength, w/c = 0.5, 10mm

Mix ID	28-Day Compressive Strength (Mpa)
RC0	2.90
RC50	1.67
RC100	1.52

6. Conclusion

1-Increasing RCA content reduces compressive strength, direct tensile strength, and indirect tensile strength.

2-Recycled aggregates have lower strength due to the presence of old mortar adhered to their surface.

3-RCA particles tend to break into finer particles during mixing, increasing the fine aggregate content and reducing slump.

References

[1] Rao, A., Jha, K. N., & Misra, S. (2007). Use of aggregate from recycled construction and demolition waste in concrete. Resources, Conservation and Recycling, 50(1), 71–81. https://doi.org/10.1016/j.resconrec.2006.05.010

[2] Olorunsogo, F. T., & Padayachee, N. (2002). Performance of recycled aggregate concrete monitored by durability indexes. Cement and Concrete Research, 32(2), 179–185. https://doi.org/10.1016/S0008-8846(01)00653-8

[3] Malhotra, V. M., & Neville, A. M. (1995). Symposium on concrete technology and the use of demolition waste in concrete. In P. J. Wainwright (Ed.), Proceedings of PJ26 (pp. 179–197).

[4] Frondistou-Yannas, S. (1980). Economics of concrete recycling in the United States. In Advanced Research Institute—Problems in Recycling Concrete, France, 25–28 (pp. 193–186).

[5] Hansen, T. C. (Ed.). (1992). Recycling of demolished concrete and masonry. RILEM.

[6] Ajdukiewicz, A., & Kliszczewicz, A. (2002). Influence of recycled aggregate on mechanical properties of HP/HPC. Cement and Concrete Composites, 24(2), 269–279. https://doi.org/10.1016/S0958-9465(01)00012-9

[7] Eguchi, K., Teranishi, K., Nakagome, A., Kishimoto, H., Shinozaki, K., & Narikawa, M. (2007). Application of recycled coarse aggregate by mixture to concrete construction. Construction and Building Materials, 21(7), 1542–1551. https://doi.org/10.1016/j.conbuildmat.2006.06.007

J-Researchers

Journal of Civil Engineering Researchers

Journal homepage: www.journals-researchers.com

Comparison of the Response of a Structure Isolated from the Base with a Similar Structure in a Fixed Form

Hosein Sarkoyeh,[a,*] Morteza Shahsavari Pirkouei,[b] Saeed Khajevand,[c] Reza Moghimi[d]

[a] *Department of Civil Engineering, Cha.C., Islamic Azad University, Chalus, Iran.*
[b] *Department of Civil Engineering, Cha.C., Islamic Azad University, Chalus, Iran*
[c] *Department of Civil Engineering, K.N.Toosi university of technology, Tehran Iran*
[d] *Department of Civil Engineering, Shahid Bahner University of Kerman, Kerman, Iran*

ABSTRACT

The seismic response characteristics of a 5-story isolated structure on the foundation surface and a non-isolated foundation with an equal number of indeterminate degrees and three types of design earthquakes have been investigated. The isolators were modeled using a mathematical model and elastic and hysteretic rotors, and significant results were obtained. The effect of the shape of the isolator force-deformation ring on the response of the isolated structure is studied under the variation of important system parameters such as the isolator yield displacement, superstructure flexibility, separation period, and the number of stories of the structure separated from the foundation. The changes of the upper story absolute acceleration and bearing displacement are calculated for different two-line systems under different earthquakes to study the effects of the isolator residual ring shape. The maximum displacement in the isolated structure is at the ground floor and is zero in the same structure without the isolator at the same location. The forces generated, shear and moment, are also less in the isolated state than in the fixed state to the foundation. Low values of isolator yield displacement (i.e., sliding-type isolator systems) tend to increase the superstructure accelerations associated with high frequencies. In addition, superstructure acceleration also increases with increasing superstructure flexibility.

ARTICLE INFO

Received: March 13, 2025
Accepted: May 11, 2026

Keywords:
Base isolation,
Earthquake,
Displacement,
Hysteresis,
Equivalent linear

DOI: 10.66224/JCER.8.2.63
DOR: 20.1001.1.2538516.2026.8.2.6.1

1. Introduction

Seismic isolation is a method of controlling seismic vibrations by separating the structure from the ground in buildings and bridges. In contrast to conventional methods of seismic retrofitting and improvement, which increase the size of the structure, this method focuses on reducing the seismic response and the force and acceleration of the earthquake input to the structure isolation, which is now recognized as a mature and efficient technology, can be adopted to improve the seismic performance of strategically important buildings such as schools, hospitals, industrial structures, etc. in addition to the places where sensitive equipment are intended to protect from hazardous effects during earthquake [1-2]. Based on the extent of control to be achieved over the seismic response, the choice of the isolation system varies and thereupon its design is done to suit the requirements of use of the structure. In seismically base-isolated systems, the superstructure is decoupled from the earthquake ground motion by introducing a flexible interface between the foundation and the base of the structure. Thereby, the isolation system shifts the fundamental period of the structure to a large value and dissipates the energy in damping, limiting the

[*] Corresponding author. Tel: +989111944420; e-mail: hossein.sarkoyeh@gmail.com

amount of force that can be transferred to the superstructure such that inter-story drift and floor accelerations are reduced drastically. The matching of fundamental frequencies of base-isolated structures and the predominant frequency contents of earthquakes is also consequently avoided, leading to a flexible structural system more suitable from an earthquake resistance viewpoint. The two most common types of base isolation systems adopted in practice utilize either rubber bearings or sliding systems between the foundation and superstructure for isolation from ground motions in buildings as well as bridges.

It is very essential to understand the different parameters affecting the response of base-isolated structures when used for seismic protection of the structures. Especially in the case of the base-isolated structures, that house sensitive equipment, determination of acceleration imparted and associated peak displacement are the key issues for the design engineer [3].

Moreover, the pounding and structural impacts in the case of base-isolated structures made upon the adjacent structures, when separation gap distances are inadequate become a major concern because these phenomena may lead to catastrophic failures leading to immense isolator damage. Such failures and damages can be avoided by properly estimating the peak isolator displacement and recommending appropriate isolation gap distances. To predict peak displacement and determine the accurate separation gap distance required- meant for a base-isolated structure it is mandatory to know, in prior, the different parameters that affect the bearing displacement and its consequent effect on the superstructure acceleration. The failures due to such impacts can be avoided by reducing the peak bearing displacement by compromising with an increase in superstructure acceleration to an acceptable level i.e. tolerable reduction in the effectiveness of isolation. Selection of different parameters characterizing an isolation system is important given keeping control over response quantities, especially the excessive bearing displacement at the isolator level. The dynamic response of a base-isolated structure, therefore, is considerably reduced when compared to its counterpart, the fixed base structure as documented in the literature available on base isolation [4-5].

The behavior of isolation systems and the base-isolated structures is now well established and codes are developed for designing the base-isolated structures [6-7]. For non-linear isolation systems, the codes allow to use of the equivalent linear model to permit the use of the response spectrum method for designing the isolated structures. The equivalent linear models are based on the effective stiffness at the design displacement and the equivalent viscous damping is evaluated from the area of the hysteresis loop. The comparison of equivalent linear and actual non-linear models for the response of isolated bridge structures has been demonstrated in the past [8-9] and shown that the equivalent linear model can be used for predicting the actual non-linear response of the system.

The LRB isolators with hardening behavior were developed for low to mid-rise buildings located in the moderate seismicity area, and besides, the behavior of the base-isolated building was accurately predicted by nonlinear dynamic analyses performed with relatively long-period ground motions [10].

2. Structural model of base-isolated building

The figure shows the idealized mathematical model of the N-story base-isolated building considered for the present study. The base-isolated building is modeled as a shear-type structure mounted on isolation systems with one lateral degree of freedom on each floor.

The following assumptions are made for the structural system under consideration:

1. The superstructure is considered to remain within the elastic limit during the earthquake excitation. This is a reasonable assumption as the isolation attempts to reduce the earthquake response in such a way that the structure remains within the elastic range.

2. The floors are assumed rigid in their plane and the mass is supposed to be lumped at each floor level.

3. The columns are inextensible and weightless providing the lateral stiffness

4. The system is subjected to a single horizontal component of the earthquake ground motion

5. The effects of soil structure interaction are not taken into consideration

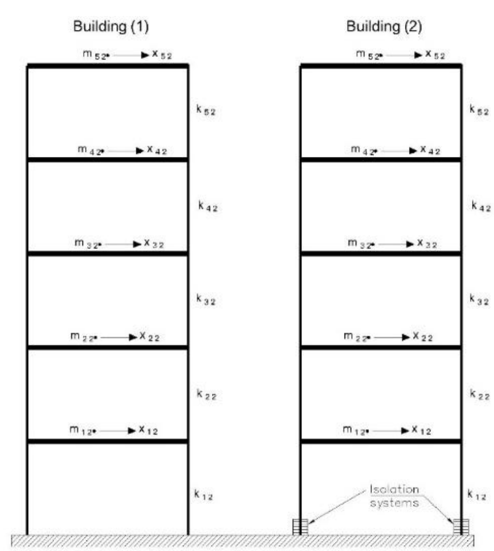

Figure 1. Mathematical model of N-story base-isolated structure

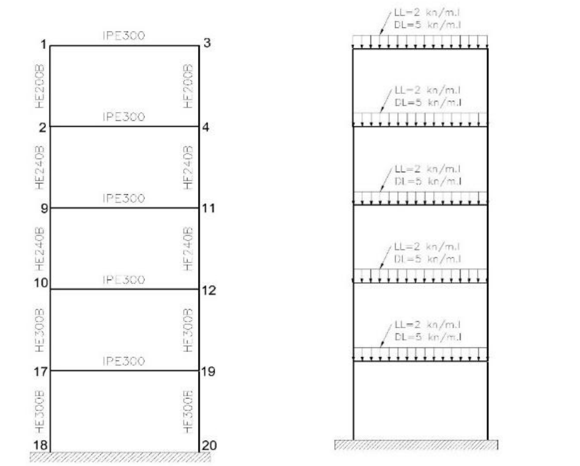

(a) Living and dead forces entering the frame (b) Node number - frame sections

Figure 2. Specifications of structural components, node number and amount of load applied at floor level

2.1. Damping force

Figure 1. Mat hem The force generated in the viscoelastic damper comprises two components: elastic force and damping force. The elastic force is proportional to the relative displacement between the connected floors, whereas the damping force is essentially proportional to the relative velocity of the piston head concerning the damper casing. Hence, the damper force can be expressed ascetical model of the N-story base-isolated structure.

$$F_d = [K_d]\{Ub. U1. U2. \ldots . Ul\}^T + [C_d]\{\dot{U}b. \dot{U}1. \dot{U}2. \ldots . \dot{U}l\}^T \quad (1)$$

The vectors of relative displacement and velocity between the damper-connected floors of the adjacent buildings and the over-dot denote the derivative concerning time. Here, the stiffness elements of dampers placed along the height of the adjacent structures is

2.2. Bilinear model and parameters of the lead core isolator model

The bilinear model, used to express the relation between the shear force and the lateral displacement, can be defined by three parameters: elastic stiffness, key, post yield stiffness, kip, and characteristic strength, Q The characteristic strength, Q, is usually utilized to estimate the stability of hysteretic behavior when the bearing experiences many loading cycles. Fig 3 shows an idealized bilinear model based on test data [11].

3. Unconnected building systems

In general, three different types of isolation systems are used in the structure in question: High Damping Rubber Bearings (HDRB), Lead Rubber Bearings (LRB), and Friction Pendulum Systems (FPS) which are placed under the base isolation buildings. For a fixed base building, the corresponding isolation in the above governing equations of motion with appropriate modifications in the mass, stiffness and damping matrices

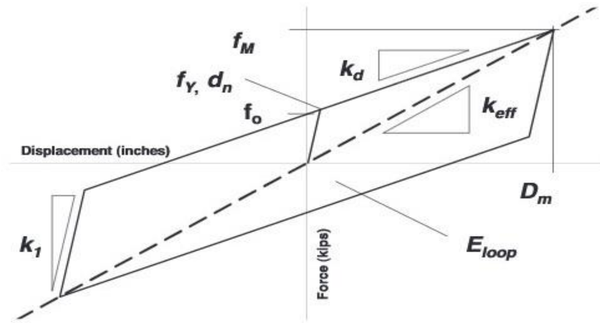

Figure 3. SBFEM applied to semi-infinite layer

3.1. High-damping rubber bearing

The bi-linear behavior is selected because this model can be used for all isolation systems used in practice. The characteristic strength Q is related to the yield strength of the lead core in the elastomeric bearings and friction coefficient of the sliding type isolation systems. The stiffness and damping of the HDRB are selected to provide the specific values of the two parameters characterizing the system namely the isolation time period (Tbi) and damping ratio (ξ_{bi}) defined as.

$$T_{bi} = 2\pi\sqrt{\frac{M_i}{K_{bi}}} \quad (2)$$

$$\xi_{bi} = \frac{C_{bi}}{2M_i\ \omega_{bi}} \quad (3)$$

where $\omega_{bi} = \frac{2\pi}{T_{bi}}$ is the isolation frequency.

3.2. Equivalent linear elastic viscous damping model of isolators

As per the Uniform Building Code [13] and International Building Code [7], the non-linear force deformation characteristic of the isolator can be replaced by an equivalent linear model through effective elastic stiffness and effective viscous damping. The linear force developed in the isolation system can be expressed as

$$F_b = K_{eff}\, x_b + c_{eff}\dot{x}_b \quad (4)$$

The equivalent linear elastic stiffness for each cycle of loading is calculated from experimentally obtained force deformation curve of the isolator and expressed mathematically as

$$= K_{eff}\frac{F^{+}-F^{-}}{\Delta^{+}-\Delta^{-}} \quad (5)$$

The effective viscous damping of the isolator unit calculated for each cycle of loading is specified as

$$\beta = {}_{eff}\frac{2}{\pi}\left[\frac{E_{loop}}{K_{eff}\,(|\Delta^{+}|+|\Delta^{-}|)^{2}}\right] \quad (6)$$

Where E loop is the energy dissipation per cycle of loading.

At a specified design isolation displacement, D, the effective stiffness and damping ratio for a bi-linear system are expressed as

$$K_{eff} = K_b + \frac{Q}{D} \quad (7)$$

$$\beta = eff\frac{4\,Q\,(D-q)}{2\,\pi\,K_{eff}\,D^{2}} \quad (8)$$

4. Solution of equations of motion

The classical modal superposition technique cannot be employed in the solution of equations because the system is not classically damped due to the difference in damping in the isolation system as compared to the damping in the superstructure of a base-isolated building as well as the damper links. Therefore, for different earthquakes, the equations of motion are solved numerically using Newmark's method of step-by-step integration; adopting a linear variation of acceleration over a small time interval of Ar. The time interval for solving the equations of motion is taken as 0.02/20 sec (ie □t 0.001 sec). At each time instant, the responses, namely the accelerations and displacements are obtained at each floor level of the two adjacent buildings.

5. Numerical study

The seismic response of two adjacent multi-storied buildings, connected using viscoelastic dampers, either both or one of them supported on isolation devices is investigated here. The multi-degree-of-freedom shear models of the adjacent buildings are used, with linear viscoelastic damping devices at different floor levels in Fig 1. The earthquake selected for this study (1) The Bam earthquake was a magnitude 6.6 earthquake that shook the city of Bam and its surrounding areas in eastern Kerman Province at 5:26 a.m. on Friday, January 25, 2003, for 12 seconds (2) The Tabas earthquake was a 7.8 magnitude earthquake that occurred at 7:36 PM on Saturday, September 15, 1978, at a depth of 10 kilometers, destroying the city of Tabas and its surrounding villages (3) The Rudbar-Manjil earthquake of 31 June 1980, with a magnitude of 7.4, occurred at 30:00 AM Iranian time, i.e. in the early hours of Thursday, 31 June 1980 (equivalent to 20 June 1990 at 21:00 GMT), approximately 16 km from Rudbar, centered in the village of Pakdeh and its affiliated villages in Gilan province

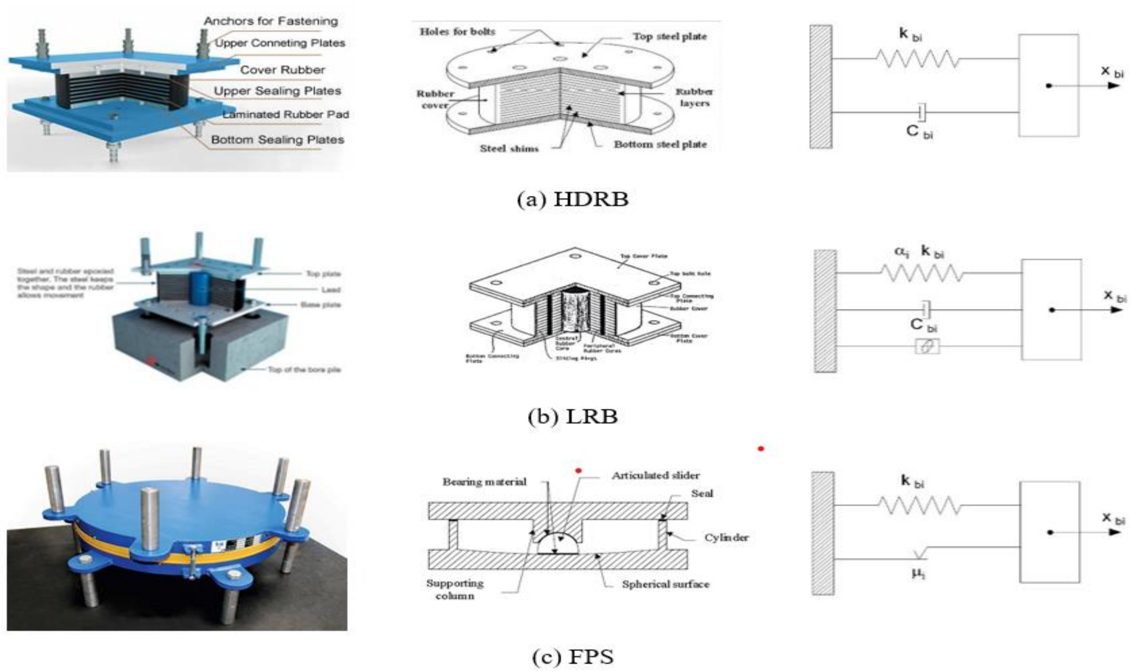

Figure 4. Schematic models of isolation systems (a) HDRB (b) LRB and (c) FPS

5.1. The shape coefficient of the spectrum of the ground plan

According to Standard 2800 of Iran, the shape coefficient of the spectrum of the plan used in this study, type II land and the acceleration of the plan for the area with a very high-risk area is considered 0.35. In the figure3, the shape factor of the design spectrum for all types of soils in the zone of high risk and high void can be seen.

5.2. Technical and mechanical specifications used in dampers and separators

A seismic isolation head and a viscoelastic damper were used to analyze 5-story structures and observe the displacement in the structure based on 3 design earthquakes. The mechanical specifications and initial analytical results for use in the SAP2000 program are specified in the tables below. Considering the initial results and placing each of them in 5-story structures, they were analyzed according to Figure 1

The following tables show the results of structural analysis in cases where a viscoelastic damper is used to connect two structures on the floor or as a metal member. Also, a seismic isolator is also used in the structures at the same time, as shown in Figure 1. The amount of dead and live loads used in structural analysis is also specified in Figure 1.

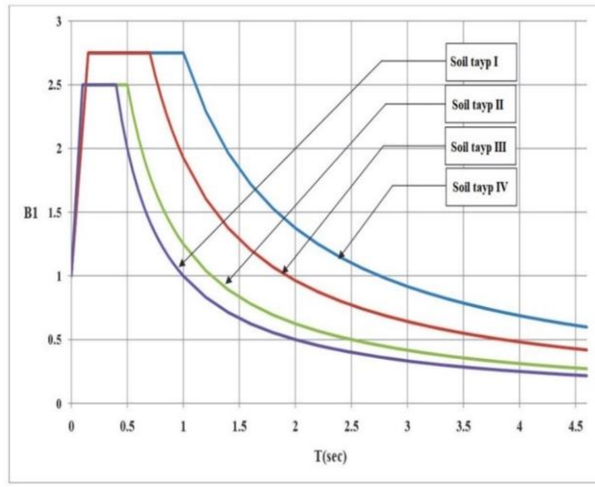

Figure 5. Shape coefficient of the design spectrum for all types of soils

Table 1.
Characteristics of Earthquakes

position	Load applied to the column W (ton)	Lead core yield strength Q (ton)	Yield strength Fy (kn)	stiffness k0 (kn/m)	Effective stiffness Keff (kn/m)	Effective periodicity Teff (sec)	Effective damping ratio ζeff	Effective damping Ceff (kn.s/m)
5-storey structure	63.00	3.15	37.12	3711.94	849.03	1.71	0.16	73.02

5.3. Hysteresis diagram of the separator at the column foot position

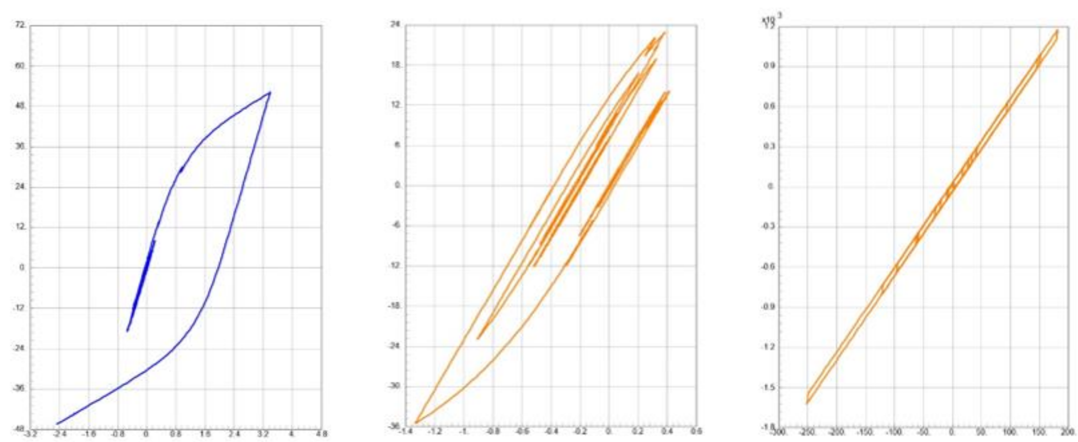

(a) The Bam earthquake (b) The Tabas earthquake (c) The Rudbar-Manjil earthquake

Chart 1. Isolator hysteresis diagram according to design earthquake

5.4. Damping energy at node positions

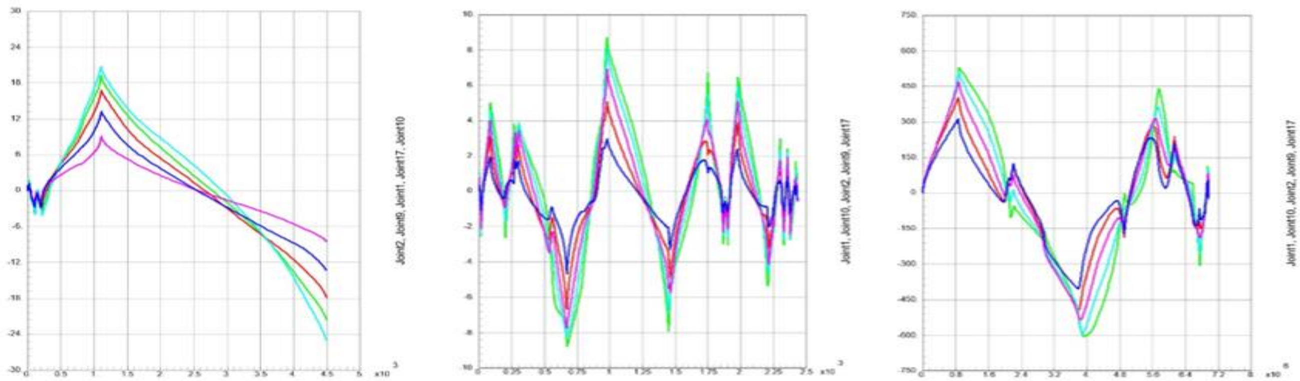

(a) The Bam earthquake (b) The Tabas earthquake (c) The Rudbar-Manjil earthquake

Chart 2. Damping energy at node positions when using an isolator

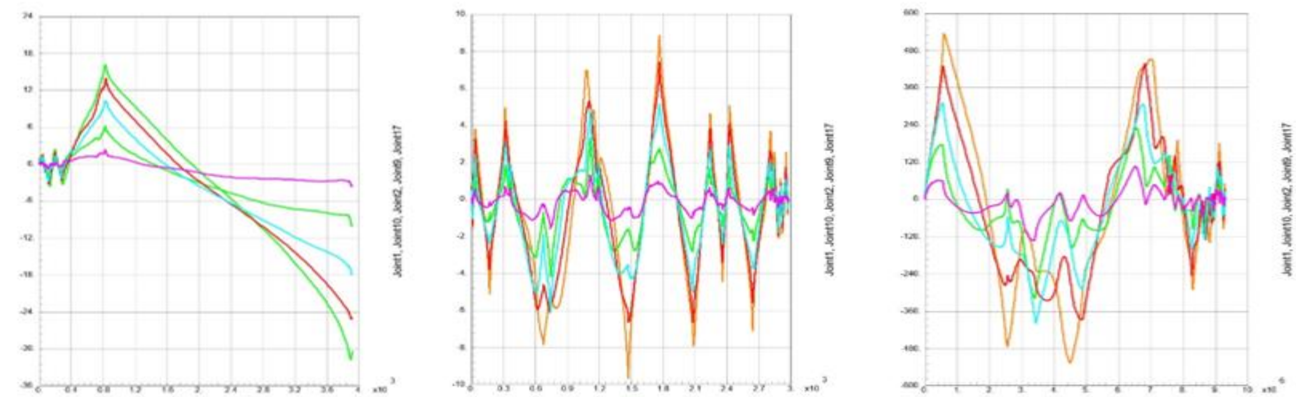

(a) The Bam earthquake (b) The Tabas earthquake (c) The Rudbar-Manjil earthquake

Chart 3. Damping energy at node positions in the fixed connection mode in the foundation

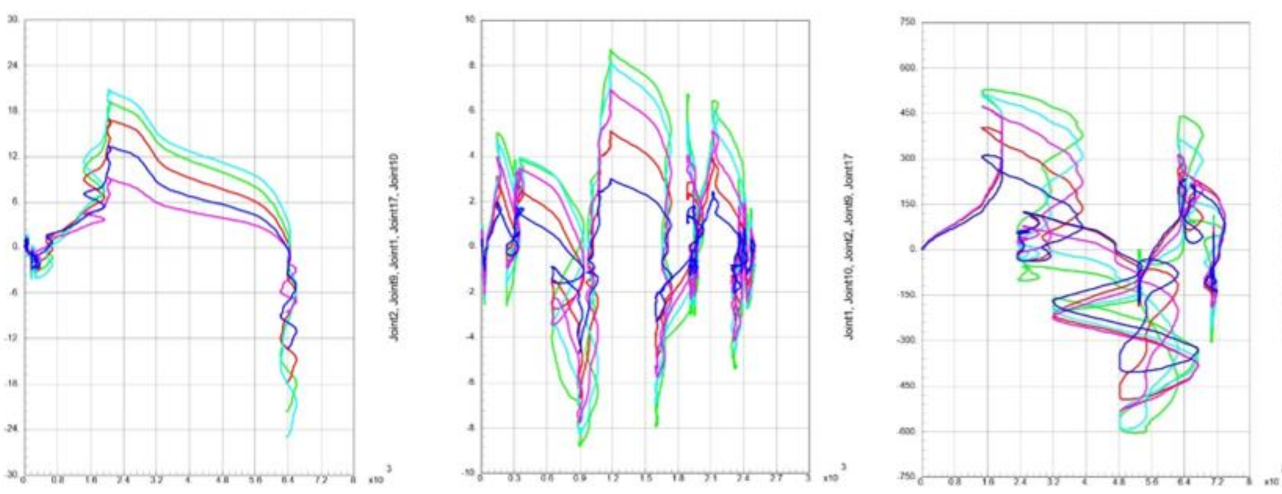

(a) The Bam earthquake (b) The Tabas earthquake (c) The Rudbar-Manjil earthquake

Chart 4. Diagram of energy input at node positions when using the isolator

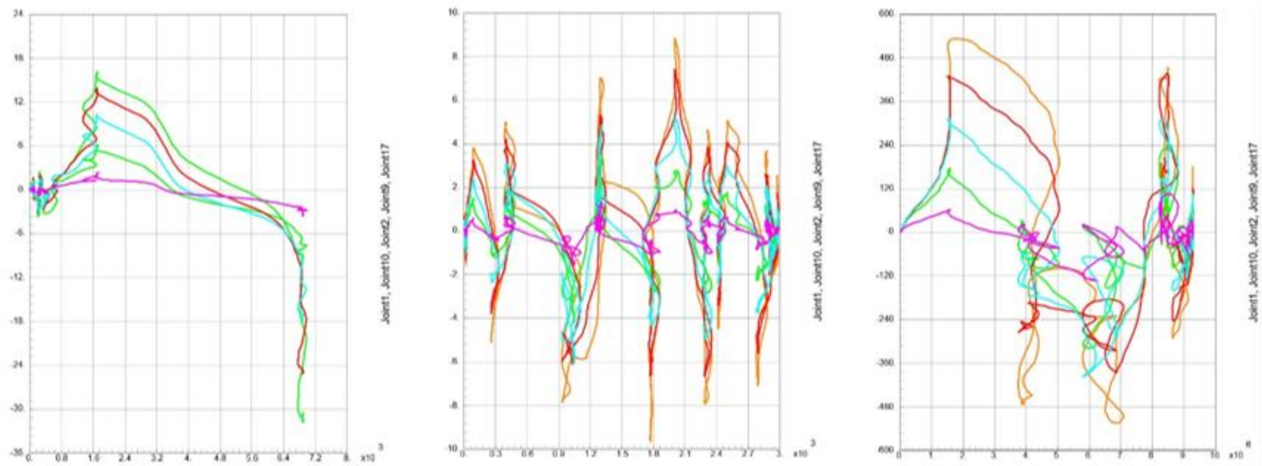

(a) The Bam earthquake (b) The Tabas earthquake (c) The Rudbar-Manjil earthquake

Chart 5. Diagram of energy input at the node positions in the beam-foundation connection mode

6. Conclusions

The displacement and seismic response of buildings in two cases (1) placed on a foundation in a fixed connection mode and (2) placed on a seismic isolator were investigated in this study, and the following results were obtained.

1. The hysteresis behavior of the isolator placed under the columns in the isolated state (Building 2) has different performance due to the loading cycles caused by the earthquake, depending on the type of uniform structure, so that in Figure (C) related to the Rudbar-Manjil earthquake, it tends to be linear.

2. As can be seen in Chart 2 and 3, with respect to the design earthquake, the damping value at node positions at different levels of the structure in the isolated state is less than in the case where the structure is directly fixed on the foundation.

3. Chart 4 and 5 show the amount of energy entering the structure. Considering the design earthquake, the damping value at node positions at different levels of the structure in the isolated state is much lower than in the case where the structure is located directly on the foundation.

Rferences

[1] Kelly, James M. "Aseismic base isolation: review and bibliography." Soil Dynamics and earthquake engineering 5.4 (1986): 202-216. https://doi.org/10.1016/0267-7261(86)90006-0

[2] Jangid, R. S., and T. K. Datta. "SEISMIC BEHAVIOUR OF BASE-ISOLATED BUILDINGS: A STATE-OF-THE ART REVIEW." Proceedings of the institution of civil engineer’s structures and buildings 110.2 (1995): 186-203. https://doi.org/10.1680/istbu.1995.27599

[3] Stanton, John, and Charles Roeder. "Advantages and limitations of seismic isolation." Earthquake Spectra 7.2 (1991): 301-324. https://doi.org/10.1193/1.1585630

[4] Kelly, James M. "Aseismic base isolation: review and bibliography." Soil Dynamics and earthquake engineering 5.4 (1986): 202-216. https://doi.org/10.1016/0267-7261(86)90006-0

[5] Jangid, R. S., and T. K. Datta. "SEISMIC BEHAVIOUR OF BASE-ISOLATED BUILDINGS: A STATE-OF-THE ART REVIEW." Proceedings of the Institution of Civil Engineers Structures and Buildings 110.2 (1995): 186-203. https://doi.org/10.1680/istbu.1995.27599

[6] Kelly, James M. "Base isolation: linear theory and design." Earthquake spectra 6.2 (1990): 223-244. https://doi.org/10.1193/1.1585566

[7] International Code Council, et al. International energy conservation code. International Code Council, 2000.

[8] Turkington, D. H., et al. "Design method for bridges on lead-rubber bearings." Journal of Structural Engineering 115.12 (1989): 3017-3030. https://doi.org/10.1061/(ASCE)0733-9445(1989)115:12(3017)

[9] Turkington, D. H., et al. "Design method for bridges on lead-rubber bearings." Journal of Structural Engineering 115.12 (1989): 3017-3030. https://doi.org/10.1061/(ASCE)0733-9445(1989)115:12(3017)

[10] Noruzi, Faramarz, Ahmad Hasanpour, and Sahand Saeedian. "Seismic Response Assessment of high-rise RC building with Lead Rubber bearing base isolator on different soil types." Journal of Civil Engineering Researchers 0 (2017): 1-9. https://www.journals-researchers.com/ojs/index.php/jcer/article/view/23

[11] Bagherinejad, Kamyar, Shahin Charkhtab, and Seyedhamed Hosseini. "Cost Viability of a Base Isolation System for the Seismic Protection of mid-rise reinforced concrete moment frames." Journal Of Civil Engineering Researchers 1.1 (2017): 1-7. https://www.journals-researchers.com/ojs/index.php/jcer/article/view/2

[12] American Society of Civil Engineers. "Minimum design loads and associated criteria for buildings and other structures." American Society of Civil Engineers, 2017. https://doi.org/10.1061/9780784414248
[13] Code, Uniform Building. "International building code." International Code Council, USA (1997).

Journal of Civil Engineering Researchers

Journal homepage: www.journals-researchers.com

Evaluation of High Capacity Helical Piles in Silty Clay

Farhad Nabizadeh,[a,*]

[a] Department of Civil Engineering, Cha.C., Islamic Azad University, Chalus, Iran

ABSTRACT

A new foundation system employing in situ grouting of helical screw piles has recently been developed. The paper discusses design considerations, installation procedures and results of full scale field load tests. This study assessed axial static loading tests on single, double and triple helix helical piles under grouted and un-grouted conditions. The field study was conducted to investigate the behavior of helical piles in silty clay soil. Also, the ultimate load capacity (Qu) for each pile test was predicted using six different interpretation methods. Also, the effect of post-grouting on the strength of these piles was assessed and the results of the piles load tests were interpreted using 6 methods presented in literature to predict the ultimate load capacity (Qu) for each pile. Results showed that the grouted helical piles are excellent foundation systems for the resistance of uplift, as well as, compressive loads and resistance against corrosion and less harmful to the environment than other types of piles especially in urban areas.

ARTICLE INFO

Received: April 16, 2026
Accepted: May 24, 2026

Keywords:
Capacity
Helical piles
Post Grouting
Silty Clay
Soil Mechanics

DOI: 10.66224/JCER.8.2.71
DOR: 20.1001.1.2538516.2026.8.2.7.2

1. Introduction

Large design loads, poor soil at shallow depth, or site constraints like property lines are some of the most important reasons for using deep foundations. The use of helical pile as a kind of deep foundation has considerably increased in recent years. Currently, more than 50 manufacturers in the world produce a wide range of helical piles and anchors [1]. For the past 170 years, helical piles have been in use. Alexander Mitchell, an Irish civil engineer, is known as the inventor of the first helical piles which were used in the design of foundations for lighthouses [1–7]. A helical pile is a deep foundation system that consists of regularly spaced helical steel plates welded to a slender steel shaft. The central shaft can be square, round or a combination of square and round shafts, depending on the soil and loading conditions. The helices, which are typically fixed to a lead shaft section of up to 3 m length, can all have a common diameter or the helices may increase in diameter with distance above the tip of the pile. The pile is installed into the ground by applying torque to the shaft, causing the pile to screw through the soil. An axial compression force is applied to ensure that the pile advances through the soil [8–12].

Up to the year 2005, torque motors commonly used for helical pile installation produced a torque of 4500 to 80,000 ft—lb (6.1 to 108.5 kN.m) while new generation of torque motors that became available on the market in the late first decade of the 2000's offer torque up to 250,000 ft—lb (339 kN.m). Due to this development of powerful hydraulic rotary heads, helical piles have become more popular in recent years [13]. Helical piles have been used in the

* Corresponding author. Tel: +989113914437; Email: f.nabi799799@gmail.com

construction of structures subject to uplift forces such as buried pipelines, telecommunication and transmission towers, machine foundations, commercial and residential buildings [10,14]. They provide several construction and performance advantages over conventional concrete and steel piles including light weight, high compressive and uplift capacities, short installation time with minimal noise and vibration levels, suitability for construction in limited access conditions, installation in frozen or swamp soil conditions and their cost effectiveness and providing overturning and uplift stability immediately after installation due to the elimination of the curing that is encountered in concrete anchors [2,9]. Furthermore, helical piles don't have loud noise during installation so they are suitable for urban areas since they are not harmful to the environment.

Despite the many benefits of helical piles, the available literature provides only limited insight into their behavior compared to the other types of piles. Furthermore, the advantages of helical piles can be improved by some methods such as post-grouting, on which there are only few studies., Therefore, it is necessary to perform further studies on the behavior of helical piles.

Several studies have been conducted on the behavior of helical piles; Clemence; Mooney et al. Conducted field and laboratory testing; Hoyt, Hoyt et al., and Ghaly and Clemence conducted theoretical and experimental testing, Puri and Vijay, Huang et al., Perko, and Pack conducted theoretical analyses. Rao and Prasad, Prasad and Rao, conducted experimental testing; Vickars and Clemence studied the performance of helical piles with grouted shafts and discussed design considerations, installation procedures and results of full scale field load tests. It was noted that the grouted column significantly increases the anchor shaft's resistance to buckling and provides additional corrosion protection. It was also stated that the grouted shaft increases the stiffness of the column and bearing capacity of foundation [15].

Furthermore, few studies conducted on the performance of helical piles in full scale including a research by Mohammed Sakr showed that helical piles with double helixes provided about 40% higher resistance compared with piles with a single helix[14]. Therefore, the use of an additional helix, which adds only a minimal cost, is a very cost-effective method for increasing the capacity of helical piles.

In another research by Sakr in 2011, the first full-scale axial compression and tension (uplift) testing program executed on large capacity helical piles was presented, according to the author's claim. A total of thirteen tests were carried out, including nine axial compression tests and four tension (uplift) tests. The results of the axial compressive and tensile pile load tests and field monitoring of helical piles with either single helix or double helixes installed in either dense sand or very dense to very hard clay till soils showed that helical piles can develop significant resistance to axial compressive loads up to 2500 kN and tensile loads up to 2000 kN [13].

Also Weech and Howie presented the results of observations of pore pressures during and after installation of helical piles and interpreted the results of load test on these piles in a soft, sensitive clayey silt. The results showed that the capacity mobilized by the helices with cylindrical bearing failure increases substantially with time as the shear strength of the soil surrounding the piles recovers after pile installation. Conversely, the capacity of the helices with individual bearing failure does not appear to increase significantly with time after installation and so the effect of installation disturbance is less [12].

In this research, field study was conducted on piles with various numbers of helixes to investigate the behavior of helical piles in silty clay. Also, the effect of post-grouting on the strength of these piles was assessed and the results of the piles load tests were interpreted using 6 methods presented in literature.

2. Testing Procedure

2.1. Test Site (Geotechnical Condition)

The pile test was performed in a site in the city of Sari located in the north of Iran. The site location is shown in Figure 1.

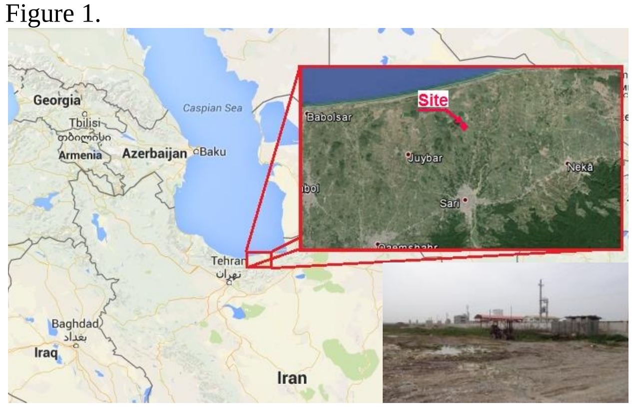

Figure 1. Location of the pile test site

Geotechnical study was conducted at the site and standard penetration (SPT) and cone penetration (CPT) tests were carried out. Soil stratigraphy at the test site consists of silty clay layers with middle layers of sand that extended to a depth of 30 m underlain by stiff layers of silt and clay that extended to a depth of 40 m. A rock layer ranging from sandstone to soft siltstone was encountered at depths greater than 40 m. Ground water level was 0.5 m below existing ground surface. Soil properties are summarized in Table 1.

Table 1.
summary of soil properties site 1

Depth(m)	Soil description	STP blow count per 300 mm	Total unit weight (gr/cm^3)	Undrained Shear Strength (Kg/cm^2)	Frictional resistance angle (°)
0-10	silty clay layers with middle layers of sand	22	1.45~1.55	0.12~0.20	18~20
10-20	silty clay layers with middle layers of sand	24	1.50~1.60	0.15~0.25	18~20
20-30	Silty clay	17	1.60~1.70	0.20~0.30	15~17
30-40	Silty clay	30	1.65~1.75	0.25~0.35	15~17
> 40	Silty clay	> 50	1.70~1.80	0.40~0.60	16~20

Based on test results, which was up to 28 m depth, number of SPT blow counts per 300 mm of penetration was 20 and afterward reached 30. Also, CPT results showed that in depths greater than 20 m, pile point resistance was about 60 kg/cm2 and pile friction resistance ranged between 2 and 4 kg/cm2.

2.2. Pile Configuration

Field behavior of helical piles was studied by assessing the piles with one, two and three helixes and with 6m length. Also, effect of post-grouting on the behavior of piles was evaluated using piles with shaft diameter of 117 mm and helix diameter of 250 mm. The configurations for different piles considered for the helical pile load test program are summarized in Table 2. Typical test helical piles configurations and the double helix pile used in this study are shown in Figures 3&4, respectively.

Table 2.
Summary of pile configurations

	No. of helices	Shaft diameter, (mm)	Helix diameter (mm)	Prototype anchor depth (m)
pile	1	117	250	6

2.3. Pile Installation and Test Set-up

The helical pile shaft is turned into the ground by application of torsion using a truck mounted auger or hydraulic torque motor attached to a hydraulic machine. The principal component of the equipment is the hydraulic torque motor, which is used to apply torsion (or rotational force) to the top of the helical pile. Helical piles should be installed with high-torque, low-speed torque motors, which allow the helical bearing plates to advance with minimal soil disturbance. Torque motors commonly used for helical pile installation produce a torque of 6,000 to 100,000 Nm or higher. The connection between the torque motor and helical pile should be in-line, straight, and rigid, and should consist of a hexagonal, square, or round adapter and helical shaft socket. This is typically accomplished using a manufactured drive tool. The central shaft of the helical pile is best attached to the drive tool by a high-strength, smooth tapered pin with average diameter equal to the helical pile bolt hole size. A very basic, convenient and useful aspect of most helical piles is that the capacity can be verified from the installation torque. The relationship between capacity and torque is experimentally and theoretically well-established. A torque indicator should be used to measure torque during installation. Most torque indicators are capable of measurements in increments with a precision of 500 to 1,000 Nm. A photograph showing installation equipment is shown in Figure 5.

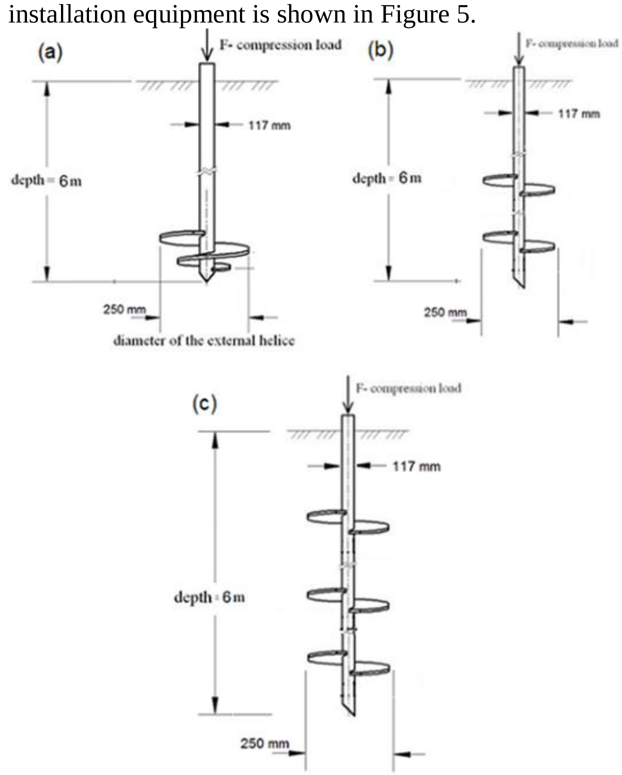

Figure 3. Typical test helical piles configurations, a) single helix pile; b) double helix pile; c) triple helix pile

Installation begins by attaching the helical pile lead section to the torque motor using a drive tool and drive pin. The lead section should be positioned and aligned at the desired location and inclination. Next, axial force should be applied to push the pilot point into the ground, then plumpness and alignment of the torque motor should be checked before rotation begins then the pile should be advanced into the soil in a smooth, continuous manner at a rate of rotation typically less than 30 rpm. Installation torque and depth should be recorded at selected intervals. Constant axial force should be applied while rotating helical piles into the ground. Helical piles are generally advanced until the termination criteria are satisfied. Termination criteria for helical piles involve achieving the required final installation torque and obtaining the minimum depth [3].

Figure 4. The double helix pile used in this study

Figure 5. Helical pile installation equipment

The axial compression load tests were carried out in accordance with ASTM standards D 1143-07. Since the main objective of the load tests was to determine the ultimate bearing capacity of the pile, Procedure A (Quick Test) was adopted for all tests wherein numerous small load increments were applied and maintained constant over short period of time intervals[16]. A photograph showing axial compression load test is shown in Figure 6(a,b&c).

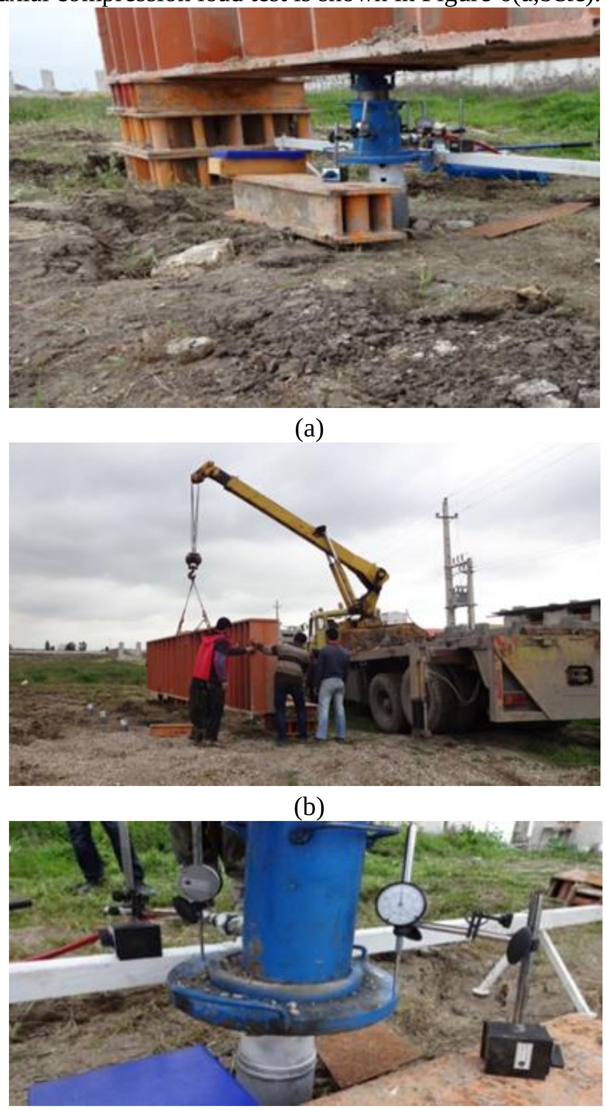

(a)

(b)

(c)

Figure 6. Test Set-up(a,b,c)

2.4. Post Grouting

The primary purpose of grouting is compaction of the soil under and around the pile point. In grouting procedure, cement grout is placed around the shaft to fill the annulus created by the anchor connection couplings while being screwed into the soil to make the shaft connecting the anchors more stiffer [17]. Grout is the most important component in grouted helical piles.

Ideal grout have a fine aggregate, such as silica fume (5-20% by weight), to increase the density and flow ability of the grout and is liquid enough to flow down around the pile shaft and should bonds to the anchor shaft so that skin friction capacity can be achieved. Also, the grout should be compatible with the soil chemistry with regards to acidity, conductivity and the presence of sulfates and chlorides.

In order to perform grouting, holes were made on the pile body. Using several separate grout flow paths provide a system that does not stop grouting operation. The grout is usually a mixture of water and cement with a water to cement ratio (W/C) of 0.4 to 0.55. Portland cement type II was thoroughly mixed with water in a colloidal mixer. Grout was compressed using simple pump. In a condition that the pile provides an adequate reaction for the frictional resistance, pressure at the top of the pile can be achieved at 311 psi. A typical view of grouting operation is shown in Figure 7.

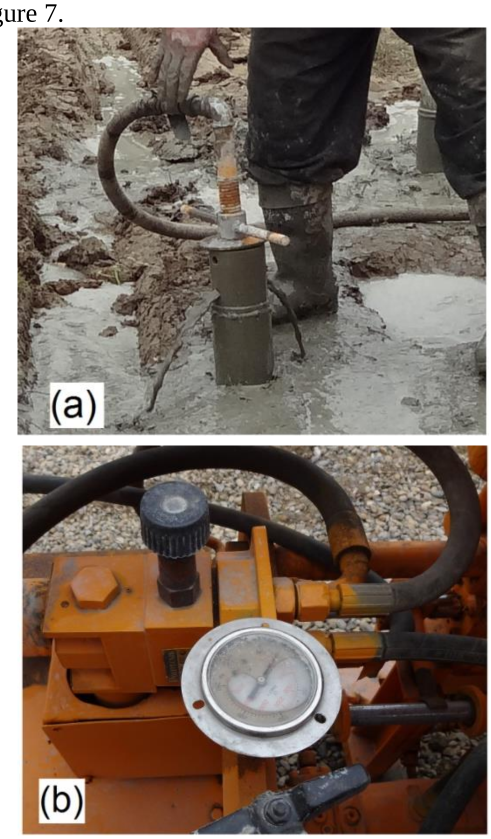

Figure 7. a) Helical piles grouting operation b) Grouting pump

3. Review of methods of interpretation of the load test results

The methods of interpretation of the load test results depend on the limit or ultimate load which can be predicted by mathematical or graphical techniques. So determining the limit or ultimate load as accurate as possible is very important. There are six methods that can be used to predict the pile capacity from load-movement records of static loading tests. A summary of these methods is presented in this section.

1-Davisson Offset Limit method: Based on a method proposed by Davisson in 1972, the pile load settlement curve is drawn to a suitable scale, so that the line shows the relationship between the load and shortening of an elastic free axially loaded column.

The offset limit load straight line is plotted parallel to the elastic line to intersect the load movement curve. Where OC is given by:

$$\text{Offset} = 4 + b/120 \qquad (1)$$

Where, b is the pile diameter in mm.

A basic benefit of this method is that the actual limit line can be plotted on the load movement diagram before beginning the test

2-Brinch Hansen's method: The load that gives four times the movement of the pile head as achieved at 80% of that load can be predicted directly from the load-movement curve, but it is more accurately determined in a plot of the square root of each movement value divided by its load value and drawn against the movement.

After calculating the slope C1, and y-intercept C2 of the drawn line, the ultimate failure load Qu is obtained as follows:

$$Qu = 1 / (2\sqrt{C1C2}) \qquad (2)$$

In many cases, the calculated 0.8 Qu doesn't intersect the observed curve, because it is more than the test load. The 80% criterion determines the load-movement curve for which the Hansen plot is a straight line throughout.

The equation for this calculated curve is shown in Eq. 4 which gives the relation for the calculated curve.

$$Q = \sqrt{S} / [C1\ S + C2] \qquad (3)$$

Where: Q = applied load, and S = movement. When using the Hansen 80%-criterion, it is important to check that the point (0.80 Qu, and 0.25 S) lies on or near the measured load-movement curve.

3-Chin-Kondner and Modified Chin Methods: Chin assumes that the relationship between load and settlement is hyperbolic. In this method, each settlement value is divided by its corresponding load value in vertical axis and the settlement in the horizontal axis. The plotted values almost lie on a straight line. The inverse slope of the straight line indicates Chin–Kondener Extrapolation Limits. This method was used to determine the load-movement curve for which the Chin-Kondner plot is a straight line throughout. The calculated curve is given by the following equation:

$$Q_u = \frac{1}{C_1} \qquad (4)$$

Where:

Q_u = Limit load

C_1= the inverse slope of the straight line

The Chin-Kondner limit load is useful when assessing the results of static loading tests, particularly in conjunction with the values determined according to Davisson's and Hansen's methods.

4-Mazurkiewicz's Method: In this method, the relationship between load and settlement is almost parabolic. A series of equal settlement lines were chosen using equal intervals and the corresponding loads were marked on the abscissa. For the marked loads on the load axis, a 45°line is plotted to intersect with the next vertical line running through the next load point. These intersections almost fall on a single straight line, the intersection of this line with the load axis defines the ultimate load.

5-De Beer's method: In this method, the load–settlement value is drawn on a double logarithmic chart. When the values fall on two approximately straight lines, the intersection of these lines determine the ultimate load.

6-Decourt's Extrapolation Method: This method is applied by dividing each load by its corresponding settlement and plotting the resulting values against the applied load. Slope C1 and y- intercept C2 constants are obtained by linear regression over the apparent straight-line.Decourt's ultimate load is the value at the intersection with the load axis, Decourt's ultimate load Qu can be accurately calculated as the ratio between the y- intercept and the slope of the line as given in Eq. 5.

$$Qu = C2 / C1 \quad (5)$$

4. Results and Discussion

As it is mentioned 6 single- helix, double - helix and triple - helix piles are executed at two sites including clay-silt and sand soil which 3 of these 6 piles were used without grouting and 3 of them were used with grouting. The helix spacing to diameter ratio (S/D) is 1.5 and 3 for double and triple helix piles, respectively. The load displacement curves are shown in Figures 8 to 12 compare the axial compressive load capacities of the piles tested under grouted and un-grouted conditions. The results show that in single- helix pile in silty clay compressive capacity has increased approximately 8% after grouting. Like single-helix piles, pile resistance has increased about 10% in double - helix. But in triple - helix piles the final load has increased about 28% after grouting. The reason is vast disturbance of the soil around the triple - helix piles which showed an increase after grouting due to the influence of slurry in the soil around resistance. Generally load-displacement curves can be divided into three main sections. . The first part is done with displacement of about 2 mm linearly and after that a non-linear components that varied from 35 to 55 mm can be observed.

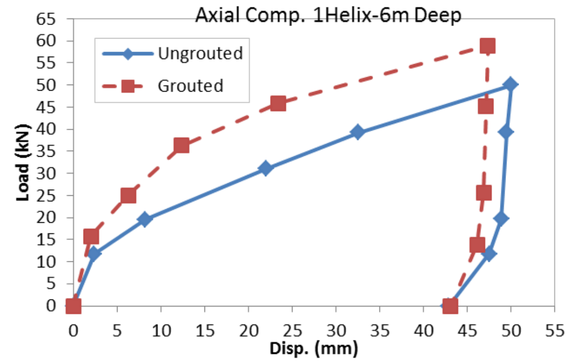

Figure 8. Axial compression load test on piles with one helix in cilty-clay

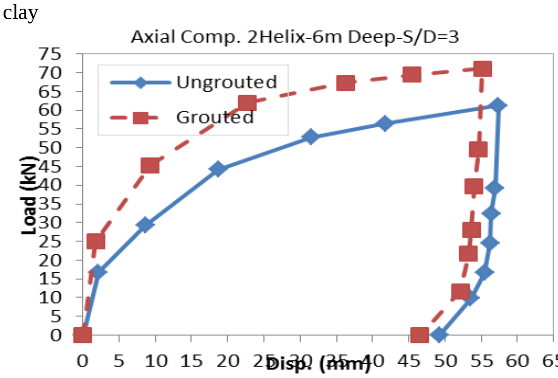

Figure 9. Axial compression load test on piles with two helix in cilty-clay

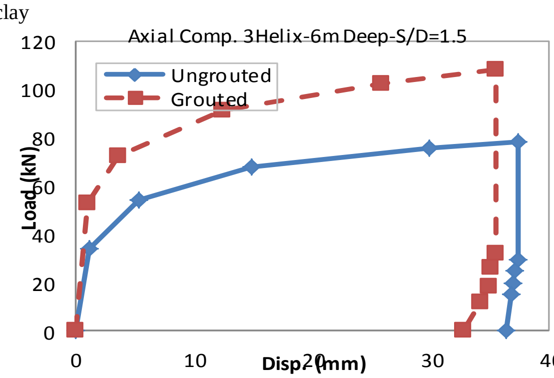

Figure 10. Axial compression load test on piles with three helix in silty - clay

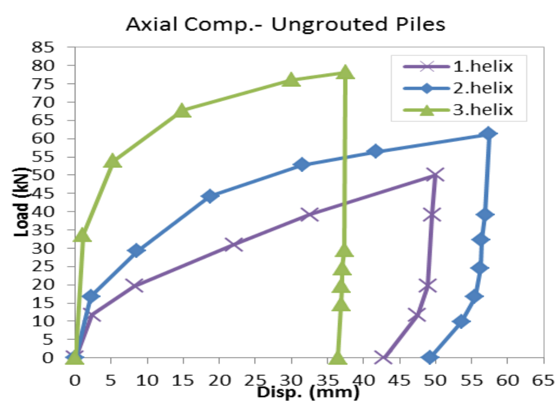

Figure 11. Axial compression load test on ungrouted in silty-clay

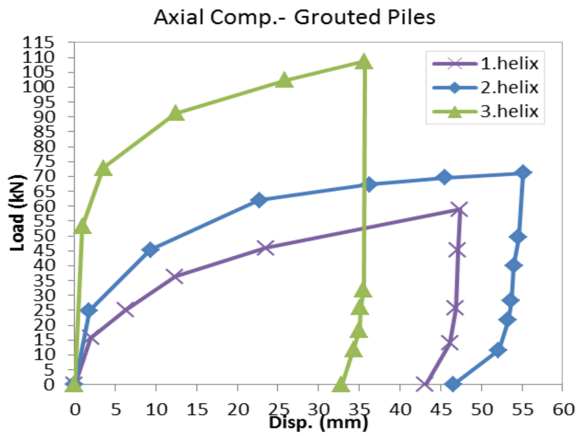

Figure 12. Axial compression load test on grouted piles in cilty-clay

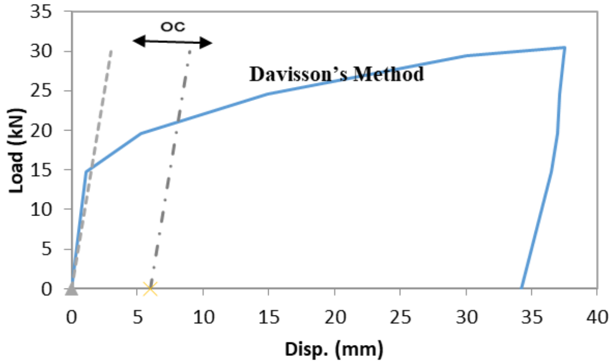

Figure 13. Ultimate failure load according to Davisson For pile no. 5

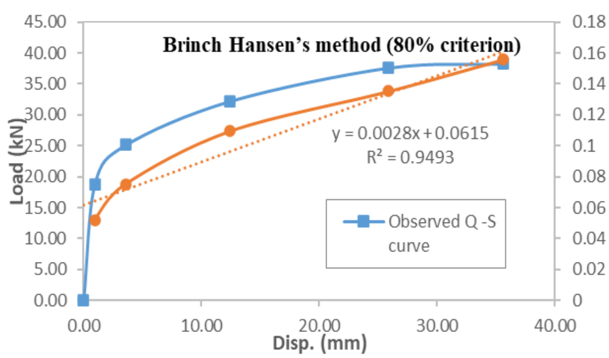

Figure 14. Ultimate failure load according to Brinch Hansen 80% criterion for pile no. 6

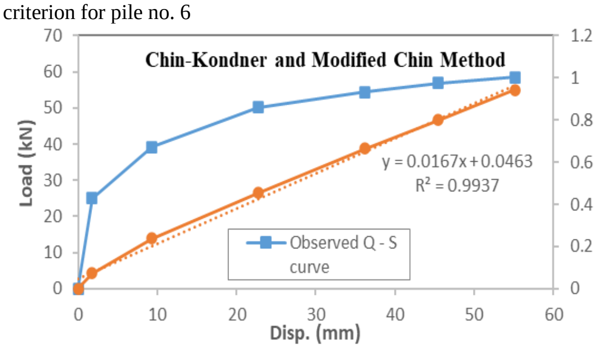

Figure 15. Ultimate failure load according to Chin- Kondner's extrapolation for pile no. 4

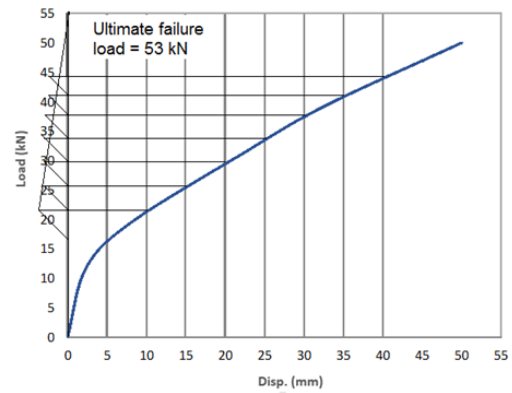

Figure 16. Ultimate failure load according to Mazurkiewicz for pile no. 1

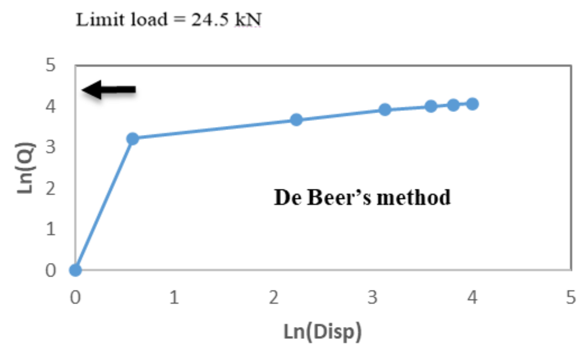

Figure 17. Yielding limit load for pile no. 3

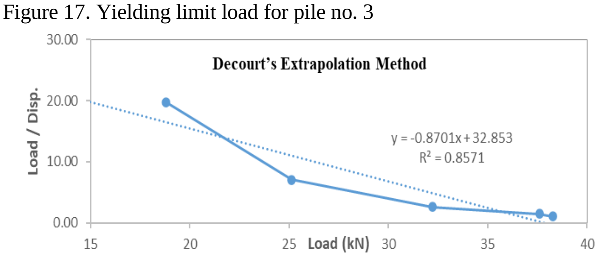

Figure 18. Decourt's Extrapolation Method for pile no. 6

It can be seen from the curves that in grouted piles in clay soil have less place shift than piles without grouting that shows grouting operation has caused an increase in pile resistance. In clayey soil none - grouting triple-helix piles bearing capacity is more than single- helix piles and double - helix piles, the reason is the cylindrical performance of triple-helix piles and single- helix piles and double - helix piles have single performance that this reason caused this that increasing the number of helix results to increase the loading capacity and stiffness of the pile. In piles due to shallow depth and low levels of tension there is no expected pile frictional resistance impact but when the grouting is done the resistance increases due to adhesion increase. Among grouted piles, grouting was more effective in triple-helix piles because the soil of the upper part is more scrabbled and grouting has filled the cracks and with a further adhesion increase gives greater load capacity. Generally it can be said that grouting operation in clay has dense performance and due to lack of penetration in clay loading capacity did not increase.

Furthermore, as it can be seen, when comparing between the load-displacement curves for grouted and un-grouted helical piles, the data showed that both types of piles had a similar performance and the trends of both types of grouted and un-grouted axial compression load tests curves are the same but grouted piles show greater axial compressive strength.

The grouted helical piles deflected less at the failure load than the ungrouted helical piles. This stiffer response is also very useful in structural support applications.

4.1. Estimation of Ultimate Load from Pile Load Test

A database of six axial static loading tests on single, double and triple helix helical piles under grouted and un-grouted conditions was compiled. The ultimate load capacity Qu for each pile test was predicted using the six different interpretation methods stated in section 2.5 that are used in the evaluation of the pile load test. Figures 13 to 18 show typical ultimate failure load predictions according to these methods. A summary of predicted ultimate failure loads is presented in Table 3 and Figures 19 to 20.

4.2. Choice of evaluation method

Choosing the best criteria for pile axial load capacity is quiet complicated since this is mostly depended on engineer's experiences and mechanism of failure. One of the conservative methods is Davisson's method.

Brinch-Hansen method is in good agreements with real ultimate resistance of pile which gives about 80% of ultimate load calculated based on static loading test.

Chin-Kondner and Decourt methods both are using extrapolation for determination limit load values, hence, the ultimate load gained from both is asymptotically.

As a straight engineering rule never to interpret static loading test result to gain ultimate load larger than the test load. Therefor allowable load should not calculate by dividing the limit loads obtained from Chin-Kondner's and Decourt's methods by a factor of safety.

The most conservative method is Mazurkiewicz method which its results are less than others methods including Davisson, Hansen, Chin, and Decourt methods. This method is easy to use and is more reliable especially for piles loaded near failure.

Table 3.
Summary of predicted ultimate failure loads

		Davisson	Hansen	Chin	Mazur	De Beer	Decourt	Test Site Load
		Qu(kN)	Qu(kN)	Qu(kN)	Qu(kN)	Qu(kN)	Qu(kN)	Qu(kN)
1 Helix	Ungrouted	22.5	54.55	53.19	53	12.18	53.7	50
	Grouted	32.5	73.7	63.7	61	16.44	61.98	58.9
2 Helix	Ungrouted	19.5	49.5	50.5	47.5	9.97	49.65	47.09
	Grouted	38	58.15	59.9	59	24.5	58.43	58.44
3 Helix	Ungrouted	21	29.5	31.05	31	14.8	29.8	30.4
	Grouted	28.5	38.1	39.22	39.5	18.17	37.75	38.29

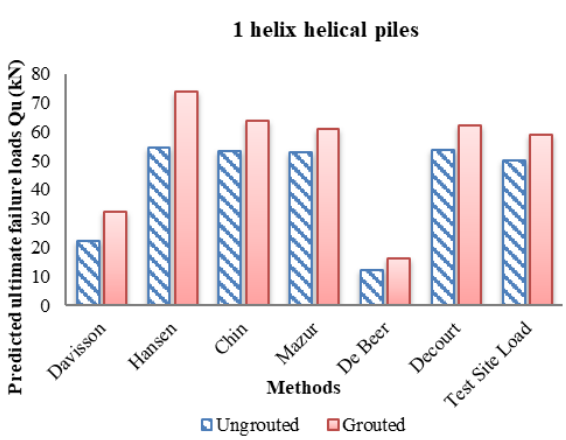

Figure 19. Summary of predicted ultimate failure loads for 1 helix helical piles

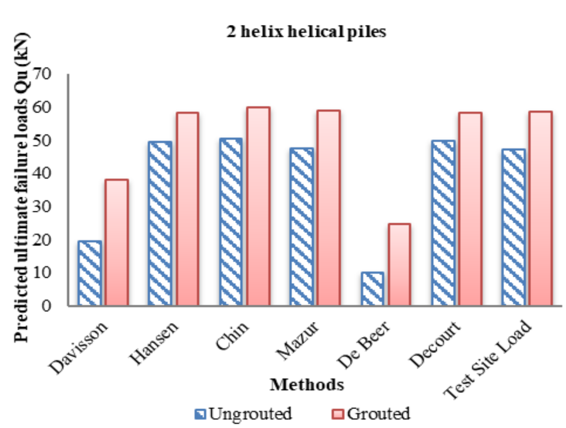

Figure 20. Summary of predicted ultimate failure loads for 2 helix helical piles

Shortcomings of De Beer's method are mentioned earlier. Hansen's 80%-criterion, Chin's and Decourt's extrapolation methods using the latter part of the load-movement curve and could extrapolated beyond the maximum load applied.

One of the advantages of Decourt's method is that a plot can be drawn while the static loading test is performing which allow the user to eyeball the projected capacity directly once a straight line plot starts to develop.

While in Chin-Kondner's method, if during the static loading test, a weakness in the pile develops, the curve would deviate from straight line. Hence it is significantly desirable plotting the readings as per Decourt's method as the test progresses. Finally these two methods estimate ultimate failure load reasonably.

5. Conclusions

In this study, helical piles behavior was evaluated. Furthermore, the effect of grouting on the load capacity of these piles was assessed and finally the limit load was obtained using methods presented. The results showed that:

For single, double and triple helix piles with various lengths, the ultimate load at the site was 50, 47.09 and 30.4, respectively.

It was seen that in all three kinds of piles, grouting increased the load capacity of piles. This increase was 17, 24 and 26 for single, double and triple helix piles, respectively.

The increase of load capacity due to grouting for double helix piles was more than other piles. Increase of resistance of triple helix piles was less than double helix piles due to soil disturbance around helixes in triple helix piles. Compression capacity in grouted helical piles increases due to the mobilization of skin friction at the grout/soil interface.

According to various limit load methods evaluation, it was concluded that the values for three methods of Chin, Decourt and Mazurkiewicz were close to the site values.

In summary, the grouted helical pile is a creative new development in anchored helical piles, which provides a great improvement in compressive load resistance further resistance against corrosion. It provides the design engineer with an excellent new foundation system for the resistance of uplift, as well as, compressive loads.

Furthermore, it is difficult to make a choice of the best axial load capacity criterion to use, because the preferred criterion depends heavily on one's experience and conception of what constitutes the ultimate resistance of a pile to failure. The most convenient methods that were applied and gave reasonable results are Chin's, Mazurkiewicz's, Decourt's, and Brinch Hansens methods. However, Davisson's, and DeBeer's methods needs the pile to be loaded for failure to be applicable.

References

[1] Perlow, J. M. (2011). Helical pile acceptance criteria, design guidelines, and load test verification. In *Geo-Frontiers 2011: Advances in Geotechnical Engineering* (pp. 94–102).

[2] Sakr, M. (2010). High capacity helical piles – A new dimension for bridge foundations. In Proceedings of the 8th International Conference on Short and Medium Span Bridges, Niagara Falls, Canada.

[3] Perko, H. A. (2009). Helical piles: A practical guide to design and installation. John Wiley & Sons.

[4] Zhang, D. J. Y., Chalaturnyk, R., Robertson, P. K., Sego, D. C., & Cyre, G. (n.d.). Screw anchor test program (Part I): Instrumentation, site characterization and installation. Edmonton, AB.

[5] Zhang, D. J. Y., Chalaturnyk, R., Robertson, P. K., Sego, D. C., & Cyre, G. (n.d.). Screw anchor test program (Part II): Field test results and design implication. Edmonton, AB.

[6] Merifield, R. S. (2011). Ultimate uplift capacity of multiplate helical type anchors in clay. Journal of Geotechnical and Geoenvironmental Engineering, 137(7), 704–716. https://doi.org/10.1061/(ASCE)GT.1943-5606.0000478

[7] Basu, P., & Prezzi, M. (1969). Design and applications of drilled displacement (screw) piles. https://doi.org/10.5703/1288284314278

[8] Rao, S. N., & Prasad, Y. V. S. N. (1991). Behavior of a helical anchor under vertical repetitive loading. Marine Geotechnology, 10(3–4), 203–228. https://doi.org/10.1080/10641199109379892

[9] Cerato, A. B., & Victor, R. (2009). Effects of long-term dynamic loading and fluctuating water table on helical anchor performance for small wind tower foundations. Journal of Performance of Constructed Facilities, 23(4), 251–261. https://doi.org/10.1061/(ASCE)CF.1943-5509.0000013

[10] El Sharnouby, M. M., & El Naggar, M. H. (2012). Field investigation of axial monotonic and cyclic performance of reinforced helical pulldown micropiles. Canadian Geotechnical Journal, 49(5), 560–573. https://doi.org/10.1139/t2012-017

[11] Liu, H., Zubeck, H. K., & Schubert, D. H. (n.d.). Finite-element analysis of helical piers in frozen ground. Journal of Cold Regions Engineering, 21(3), 92–106.

[12] Weech, C., & Howie, J. A. (2012). Helical piles in soft sensitive soils – a field study of disturbance effects on pile capacity. In VGS Symposium on Soft Ground Engineering.

[13] Sakr, M. (2011). Installation and performance characteristics of high capacity helical piles in cohesionless soils. DFI Journal: The Journal of the Deep Foundations Institute, 5(1), 39–57. https://doi.org/10.1179/dfi.2011.004

[14] Tsuha, C. H. C., Aoki, N., Rault, G., Thorel, L., & Garnier, J. (2012). Evaluation of the efficiencies of helical anchor plates in sand by centrifuge model tests. Canadian Geotechnical Journal, 49(9), 1102–1114. https://doi.org/10.1139/t2012-064

[15] Abdelghany, Y., & El Naggar, M. (2014). Full-scale field investigations and numerical analyses of innovative seismic composite fiber-reinforced polymer and reinforced grouted helical screw instrumented piles under axial and lateral monotonic and cyclic loadings. In Advances in Soil Dynamics and Foundation Engineering (pp. 414–424). https://doi.org/10.1061/9780784413425.042

[16] American Society for Testing and Materials. (2013). Standard test methods for deep foundations under static axial compressive load

(ASTM D1143/D1143M-07). Annual Book of ASTM Standards, 04.08. https://doi.org/10.1520/D1143_D1143M

[17] Vickars, R., & Clemence, S. (2000). Performance of helical piles with grouted shafts. In New Technological and Design Developments in Deep Foundations (pp. 327–341).

Author Guidelines EditEdit Author Guidelines

GENERAL GUIDELINES FOR AUTHORS

Journal of civil engineering researches invites unsolicited contributions of several forms: articles, reviews and discussion articles, translations, and fora. Contributions should fall within the broad scope of the journal, as outlined in the statement of scope and focus. Contributors should present their material in a form that is accessible to a general anthropological readership. We especially invite contributions that engage with debates from previously published articles in the journal.

Submissions are double-blind peer-reviewed in accordance with our policy. Submissions will be immediately acknowledged but due to the review process, acceptance may take up to three months. Submissions should be submitted via our website submission form (see links above for registration and login). Once you login, make sure your user profile has "author" selected, then click "new submission" and follow the instructions carefully to submit your article. If problems arise, first check the FAQ and Troubleshooting guide posted below. If you are still experiencing difficulty, articles can be submitted to the editors as email attachments.

Each article should be accompanied by a title page that includes: all authors' names, institutional affiliations, address, telephone numbers and e-mail address. Papers should be no longer than 10,000 words (inclusive of abstract 100-150 words, footnotes, bibliography and notes on contributors), unless permission for a longer submission has been granted in advance by the Editors. Each article must include a 100 words "note on contributor(s)" together will full institutional address details, including email address. We request that you submit this material (title page and notes on the contributors) as "supplementary files" rather than in the article itself, which will need to be blinded for peer-review.

We are unable to pay for permissions to publish pieces whose copyright is not held by the author. Authors should secure rights before submitting translations, illustrations or long quotes. The views expressed in all articles are those of the authors and not necessarily those of the journal or its editors. After acceptance, authors and Special Issue guest editors whose institutions have an Open Access library fund must commit to apply to assist in article production costs. Proof of application will be requested. Though publication is not usually contingent on the availability of funding, the Journal is generally under no obligation to publish a work if funding which can be destined to support open access is not made available.

Word template and guidelines

Our tailored Word template and guidelines will help you format and structure your article, with useful general advice and Word tips.

(La)TeX template and guidelines

We welcome submissions of (La)TeX files. If you have used any .bib files when creating your article, please include these with your submission so that we can generate the reference list and citations in the journal-specific style

Artwork guidelines

Illustrations, pictures and graphs, should be supplied with the highest quality and in an electronic format that helps us to publish your article in the best way possible. Please follow the guidelines below to enable us to prepare your artwork for the printed issue as well as the online version.

Format: TIFF, JPEG: Common format for pictures (containing no text or graphs).

EPS: Preferred format for graphs and line art (retains quality when enlarging/zooming in).

Placement: Figures/charts and tables created in MS Word should be included in the main text rather than at the end of the document.

Figures and other files created outside Word (i.e. Excel, PowerPoint, JPG, TIFF, EPS, and PDF) should be submitted separately. Please add a placeholder note in the running text (i.e. "[insert Figure 1.]")

Resolution: Rasterized based files (i.e. with .tiff or .jpeg extension) require a resolution of at least 300 dpi (dots per inch). Line art should be supplied with a minimum resolution of 800 dpi.

Colour: Please note that images supplied in colour will be published in colour online and black and white in print (unless otherwise arranged). Therefore, it is important that you supply images that are comprehensible in black and white as well (i.e. by using colour with a distinctive pattern or dotted lines). The captions should reflect this by not using words indicating colour.

Dimension: Check that the artworks supplied match or exceed the dimensions of the journal. Images cannot be scaled up after origination

Fonts: The lettering used in the artwork should not vary too much in size and type (usually sans serif font as a default).

Authors services:

For reformatting your manuscript to fit the requirement of the Journal of Civil Engineering Researchers and/or English language editing please send an email to the following address:

researchers.services@gmail.com

Noted: There is a fixed charge for these mentioned services that is a function of the manuscript length. The amount of this charge will be notified through a reply email.

FAQ AND TROUBLESHOOTING FOR AUTHORS

I cannot log in to the system. How do I acquire a new user name and password?

If you cannot remember your username, please write an email to (journals.researchers@gmail.com), who will locate your username and notify you. If you know your username, but cannot remember your password, please click the "Login" link on the left-hand menu at homepage. Below the fields for entering your username and password, you will notice a link that asks "Forgot your password?"; click that link and then enter your email adddress to reset your password. You will be sent an automated message with a temporary password and instructions for how to create a new password. TIP: If you do not receive the automated email in your inbox, please check your SPAM or Junk Mail folder. For any other issues, please contact our Managing Editor,Kamyar Bagherinejad (admin@journals-researchers.com).

How do I locate the online submission form and fill it out?

First you need to register or login (see above). Once you are logged in, make sure the "roles" section of your profile has "Author" selected. Once you assign yourself the role of "Author," save your profile and then click the "New Submission" link on your user home page.

Once you arrive at the submission form page, please read the instructions carefully filling out all necessary information. Unless specified otherwise by the editors, the journal section to be selected for your submission should be "Artlcles." Proceed to the remaining sections, checking all boxes of the submission preparation checklist, and checking the box in the copyright notice section (thus agreeing to journals-researchers's copyright terms). Once the first page is completed, click "Save and Continue." The next page allows you to upload your submission. Use the form to choose your file from your computer. Make sure you click "Upload." The page will refresh and you may then click "Save and Continue." You will then proceed to a page for entering the metadata for your article. Please fill out all required fields and any further information you can provide. Click "Save and Continue." The next page allows you to upload supplementary files (images, audiovisual materials, etc.). These are not required, but if you wish to provide supplementary materials, please upload them here (do no forget to click "Upload." Then click "Save and Continue." This brings you to the final page of the submission form. Please click "Finish Submission" in order to close the submission process. You wil then be notified by email that your article has been successfully submitted. TIP: If you do not receive the automated email in your inbox, please check your SPAM or Junk Mail folder. For any other issues, please contact our Managing Editor, Kamyar Bagherinejad (admin@journals-researchers.com).

Why am I not receiving any email notifications from HAU?

Unfortunately, some automated messages from Open Journal Systems arrive in users' Spam (or Junk Mail) folders. First, check those folders to see if the message was filtered into there. You may also change the settings of your email by editing your preferences to accept all mail from [jcer] and related journals-researchers.com email accounts.

I am trying to upload a revised article following an initial round of peer-review, but I cannot locate where to upload the article. Where do I submit a revised article?

Follow the login process outlined above and when you successfully login you will see on your user home page a link next to "Author" for "active" articles in our system (usually it is only one article, but if you have mulitple submissions currently in our system, the number could be higher. Click the "Active" link and you will be led to a page that lists your authored articles currently in our system. Click the link under the column labeled "Status" and this will take you to a page showing the current review status of your article. At the very bottom of the screen, you will see an upload form under the heading "Editor decision." Here you may upload your revised article. An automated email will be sent to the editors and you may also notify them directly via email. You may then logout.

I successfully submitted an article; how long will it take for the editors to respond to me with a decision.

For all articles that are recommended for peer-review, the editors of JCER strive to notify authors of a decision within 4-6 weeks. You may contact JCER's Managing Editor, Kamyar Bagherinejad (admin@journals-researchers.com). if you have any questions relating to the review process and its duration.

For all other inquiries, please contact: Kamyar Bagherinejad (Managing Editor)

Privacy Statement

The names and email addresses entered in this journal site will be used exclusively for the stated purposes of this journal and will not be made available for any other purpose or to any other party.

Articles

Section default policy

Make a new submission to the Articles section.

Copyright Notice EditEdit Copyright Notice

Journal of Civil Engineering Researchers follows the regulations of the International Committee on Publication Ethics (COPE) and the ethical principles of publishing articles in this journal are set based on the rules of this committee, and in case of problems, it will be treated according to these rules.

Privacy Statement EditEdit Privacy Statement

The names and email addresses entered in this journal site will be used exclusively for the stated purposes of this journal and will not be made available for any other purpose or to any other party.

Scholars Pavilion

Scholars Pavilion or **Scholars Chartagi** is a monument donated by the Islamic Republic of Iran to the United Nations Office at Vienna. The monument architecture is claimed by the Islamic Republic News Agency of Iran to be a combination of Islamic and Achaemenid architecture, although the latter clearly predominates in the decorative features, with Persian columns and other features from Persepolis and other remains from the Achaemenid dynasty. The Chahartaq pavilion form runs through the architecture of Persia from pre-Islamic times to the present.

Statues of four famous Persian medieval scholars, Omar Khayyam, Al-Biruni, Muhammad ibn Zakariya al-Razi and Ibn-Sina are inside the pavilion. This monument donated in June 2009 in occasion of Iran's peaceful developments in science.

J-Researchers